A QUALITATIVE FAR INFRARED CHARACTERIZATION OF CONVECTIVE CLOUD TOPS

by

Carolyn Bean

A thesis submitted in partial fulfillment of

the requirements for the degree of

Master of Science

(Atmospheric and Oceanic Sciences)

at the

UNIVERSITY OF WISCONSIN-MADISON

2026

Thesis Declaration and Approval

I, Carolyn Bean, declare that this Thesis titled 'A Qualitative Far-Infrared Characterization of Convective Cloud-Tops' and the work presented in it are my own.

Carolyn Bean	_____	_____
Author	**Signature**	**Date**

I hereby approve and recommend for acceptance this work in partial fulfillment of the requirements for the degree of Master of Science:

Tristan L'Ecuyer	_____	_____
Committee Chair	**Signature**	**Date**
Angela Rowe	_____	_____
Committee Member	**Signature**	**Date**
David Henderson	_____	_____
Committee Member	**Signature**	**Date**

Abstract

The Polar Radiant Energy in the Far-Infrared Experiment (PREFIRE) mission is the first modern spaceborne instrument capable of making spectral measurements into the far infrared region, with wavelengths spanning from 5 to 54 μm. This new observational regime provides a new dimension from which to analyze convective cloud-top properties and represents an exciting opportunity to further inform cloud physics constraints in numerical weather prediction and Earth system models. Here, we develop an algorithm to detect the presence of deep convection in PREFIRE granules using mid-infrared atmospheric window brightness temperatures. Using case studies identified by this algorithm, the variability in the spectral signals present in the full emission spectrum between continental convection, rainforest convection, rainforest deep convection, and oceanic convection is documented. These results are used to explore how the far-infrared may be able to enhance modern mid-infrared ice cloud property retrievals, propose a new identification technique for deep convection using far-infrared brightness temperatures, and to perform initial analysis of how the lifecycle stages of mid-latitude storms may impact their radiative effects. We find that distinctive far-infrared spectral shapes correspond to varying cloud height, cloud type, and cloud optical depth characteristics, as well as providing potential environmental signals and the possibility of lifecycle distinguishing characteristics. We find that there is strong promise for the use of PREFIRE data in the diagnosis of cloud-top particle properties, though much more work is required to fully tease out quantitative information.

Acknowledgments

This thesis has taken a village; I am so grateful to everyone who has supported me, offered a listening ear, tolerated my whining and complaining, and allowed me to think out loud for the past three years. In no particular order:

- My parents: for believing in me, supporting me when I decided I wanted to go to grad school after all, and for rolling with the punches when "just one year" turned into "I think I'm staying for a PhD". I love you. No, you cannot take my cat home with you.
- My advisor, Tristan L'Ecuyer: for hours of productive conversation, endless patience, constant insight, and for giving me a chance.
- My committee, Angela Rowe and Dave Henderson: for thoughtful advice and gentle guidance throughout this process. This thesis is so much better for having had your eyes on it.
- The entire PREFIRE science team, in particular Kyle Mattingly and Tim Michaels: for your unending patience as I learned how to navigate PREFIRE files, work through coding issues, and (on occasion) re-learn how to tell my east from my west.
- My Boston friends, who have stuck by me through a cross-country move and who are always willing to hop on the phone and chat, to start a book club, to spend nearly four years now working through the entire modern reboot of Doctor Who, and to support me so earnestly and relentlessly from so far away: I love you all. Thank you so much. You make this worth it.
- My Madison friends, who have welcomed me, loved me, and teased me relentlessly: I love you and I am so grateful to have you all in my life and to have built a second home here with you.
- The entire AOS department staff – Kaitlyn, Dee, Scott, Christi, Pete – thank you so much for all you do for us. Kaitlyn, thank you for rolling with it every time I changed

my mind about what I wanted to do and thank you for supporting me like you did when “what I want to do” turned into “stay here another 2-5 years”.

- And lastly, my beautiful Olive, my most beloved darling girl: You are the best cat in the whole world, even when you wake me up at 5 in the morning to eat every piece of paper on my desk. You have provided more emotional support than you can ever comprehend. I hope to keep you in treats for the rest of time.

Table of Contents

Chapter 1. Introduction

The radiative energy balance of Earth is characterized by two broad categories of radiation: incoming solar radiation and outgoing longwave radiation. By a coincidence of nature, emission from the Earth is largely in the longwave, while incident radiation from the sun is largely in the shortwave. The balance between this longwave and shortwave radiation drives weather patterns at the global level; the redistribution of heat from the tropics to the poles, which serves in part to correct local energy imbalances, is the primary force behind these weather patterns. Because of the influence this redistribution of heat has on weather and climate patterns, which can create damaging storms, long droughts, and other meteorological human impacts, it is important to thoroughly characterize this balance. Many of the processes impacting this radiative balance are not well-defined in atmospheric models. Improving the characterization of these processes represents significant potential gain in atmospheric modelling accuracy.

Modern satellite measurements have provided extensive, global measurement of Earth's emission in the visible, near, and mid-infrared spectral regions, which encompass wavelengths up to 15 μm (or wavenumbers greater than 667 $cm^{-1)}$, at spectral resolutions up to 0.35 cm^{-1} (Ackerman et al. 2019; Clerbaux et al. 2009). What modern satellite measurements have thus far failed to capture well is the far-infrared (FIR): the region of longwave emission beginning around 15 μm after the CO_2 absorption band, encompassing the far-infrared dirty window and bands of variable water vapor absorption out to the beginning of the microwave region of measurement at approximately 100 μm (100 cm^{-1}). The lack of measurement in the far-infrared represents a significant global knowledge gap. We may consider the Earth as a whole to be a far-infrared body; when we measure its brightness temperature, we measure a value around 255 K (Andrews 2000) – a value that peaks in the far-infrared at about 500 cm^{-1} (20 μm) (Goody 1964). Performing a model-based analysis of

the emission of Earth finds that, with regional variation, between 40% (in the tropics) and 65% (in the poles) of spectral emission occurs in the far-infrared (L'Ecuyer et al. 2021, Huang et al. 2014b). Incomplete characterization of this important spectral region thus limits current understanding of many cold-air atmospheric processes in the polar regions as well as at high altitudes in the mid- and low-latitudes, where deep convective and high cirrus clouds are tall enough to have notable far-infrared signatures (Libois and Blanchet 2017). Without a clear understanding of the full energy spectrum – without the 40-65% of emission that is currently uncharacterized – the models we use to characterize current and future weather patterns miss a significant piece of the picture (Gardner 2010; L'Ecuyer et al. 2015; L'Ecuyer et al. 2021).

1.1. Characterizing the far-infrared

Owing to its under-characterization, the wavelengths that constitute the far-infrared are not well-defined. References to "the far-infrared" may include the entirety of the spectral region from 15–100 μm, but the bulk of this introduction will focus on the region between 15 and 53 μm (188 cm^{-1} – 667 cm^{-1}), where the far-infrared "dirty window" band as well as strong water vapor absorption bands dominate.

The far-infrared is characterized by low-energy emission and absorptions; wavelengths in the far-infrared are longer, so the bodies that emit at these wavelengths are cooler. These longer wavelengths are dominated by strong, variable water vapor absorption (Harries et al. 2008). This strong water vapor absorption means that the lower atmosphere is effectively opaque to spaceborne far-infrared observations, as upwelling far-infrared radiation is absorbed before it reaches the upper atmosphere. The primary exceptions to this rule are cold, dry surface locations, such as the poles and high mountain-tops (Turner and Mlawer 2010; Palchetti et al. 2020; L'Ecuyer et al. 2021). In these regions, shorter wavelengths in the far-infrared spectrum

may reveal a surface signal, while the strong sensitivity of longer wavelengths to water vapor variations may support moisture retrievals (Turner and Mlawer 2010; Merrelli and Turner 2012; Shahabadi and Huang 2014; Palchetti et al. 2015). The water vapor information content provided by the far-infrared is greater than in the mid-infrared in most scenarios (midlatitude winter, tropical summer, Arctic winter) due to this increase in observable upper-tropospheric water vapor information (Merrelli et al. 2012).

Figure 1, from Harries et al. (2008), shows the optical depth of the atmosphere due to absorbers throughout the infrared: at top, water vapor and carbon dioxide, and at bottom, all atmospheric constituents except water and carbon dioxide. Three features stand out across the full spectrum: the strength of the carbon dioxide absorption band between 500 and 1000 cm^{-1}, the strength of the water vapor absorption in the far-infrared between 0 and 500 cm^{-1}, and the relative magnitudes of absorption between those two constituents and the remaining relevant absorbers. A fourth, slightly less prominent, feature is the decreased optical depth for both carbon dioxide and water vapor between 800 and 1200 cm^{-1}: evidence of the infrared atmospheric window.

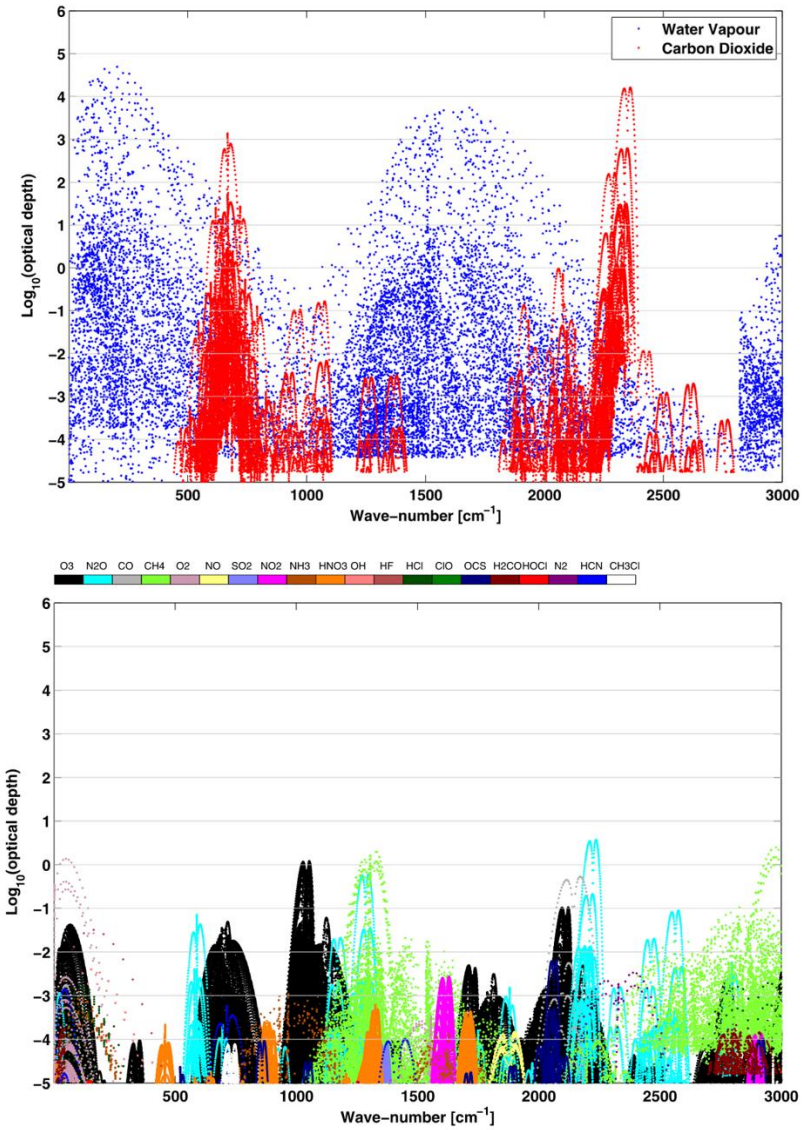

Figure 1 *(Harries et al. 2008, from Maestri 2000): Top, optical depth of lines due to water vapor and carbon dioxide throughout the IR; Bottom, optical depth of lines due to absorbers other than water vapor and carbon dioxide throughout the IR*

In this "clean" atmospheric window (also sometimes referred to as the longwave atmospheric window), absorption is low across all atmospheric constituents, making the atmosphere essentially a "window" to infrared observations. This well-known effect also occurs, albeit to a lesser degree, in the far-infrared between sharp peaks in absorption. In smaller spectral intervals, located between 17 and 25 μm, Earth's atmosphere is somewhat transparent (Rathke et al. 2002); this is called the far-infrared "dirty window". Rathke defines four particular "microwindows" as being centered at 17.45, 17.87, 18.81, and 19.14 μm (shown in

Figure 2), but for our purposes the dirty window may be defined as the spectral region between 17 and 20 μm. In sufficiently cold and dry conditions, such as the poles and at high mountain-tops, this dirty window region is capable of resolving a surface spectral signal (Turner and Mlawer 2010).

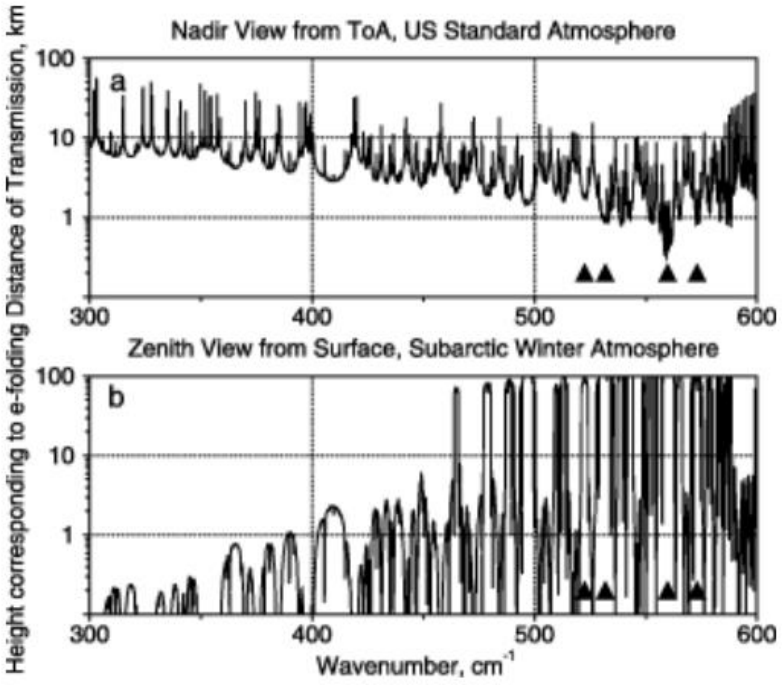

Figure 2 *(Rathke et al): Spectral variation of the height corresponding to the e-folding distance of transmission in the FIR, calculation at a 0.05 cm^{-1} spectral resolution: (a) for a nadir view from top-of-atmosphere into a clear US standard atmosphere (b) for a zenith view from surface into a clear subarctic winter atmosphere.*

The far-infrared may also offer a new angle for retrieval of vertical atmospheric composition (L'Ecuyer et al. 2021; Coursol et al. 2020; Turner and Mlawer 2010; Palchetti et al. 2020), which may discerned by analyzing atmospheric transmittance in the FIR. **Figure 3** (Harries et al. 2008) displays atmospheric transmittance between 0 and 1000 cm^{-1} for the US tropical standard atmosphere; (3a) and the U.S. subarctic winter standard atmosphere (3b) (U.S. Committee on Extension to the Standard Atmosphere, 1976), from the tropopause to the top of the atmosphere (3a(i), b(i)) and from the surface to the top of the atmosphere (3a(ii), b(ii)). It is notable that in the far-infrared (up to 600 cm^{-1}), the tropical atmosphere is entirely opaque when integrated from the surface to TOA. When isolating the stratospheric signal,

however, the atmosphere is distinctly less opaque in both the tropical atmosphere and the subarctic atmosphere, with clear variable water vapor absorption/transmission bands in the pure rotation band of the FIR. In the subarctic atmosphere, there is a local peak in transmissivity in the dirty window band, between 400 and 600 cm^{-1}.

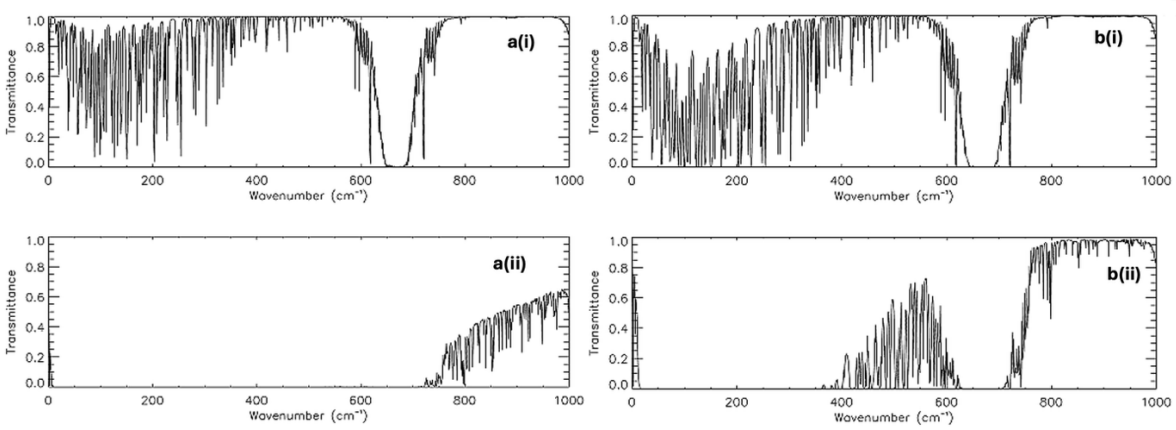

Figure 3 *(Harries et al. 2008): Transmittance in far infrared (FIR): (a) tropical standard, 12 km to TOA; (b) tropical standard, surface to TOA; (c) subarctic winter standard, 8 km to TOA; and (d) subarctic winter standard, surface to TOA (H. Brindley, unpublished manuscript, 1998)*

In general, while the atmosphere below the tropopause is relatively impermeable in the far-infrared and the surface typically cannot be distinguished, there is strong potential for valuable far-infrared retrievals in the stratosphere. In particular, the strong wavelength dependence of upper atmospheric transmissivity in the far-infrared makes the far-infrared a potentially powerful tool for the remote sensing of upper-tropospheric and stratospheric compositions (Turner and Mlawer 2010; Merrelli and Turner 2012; Shahabadi and Huang 2014; Palchetti et al. 2015). The far-infrared transmissivity of the atmosphere at different levels, as shown in **Figure 4** (Libois and Blanchet 2017), provides sensitivity to the upper troposphere (Arctic) and the stratosphere (tropics). This data may be leveraged to make observations of convective and other tropopause-penetrating high clouds in the tropics and midlatitudes, as well as near-surface observations in polar regions.

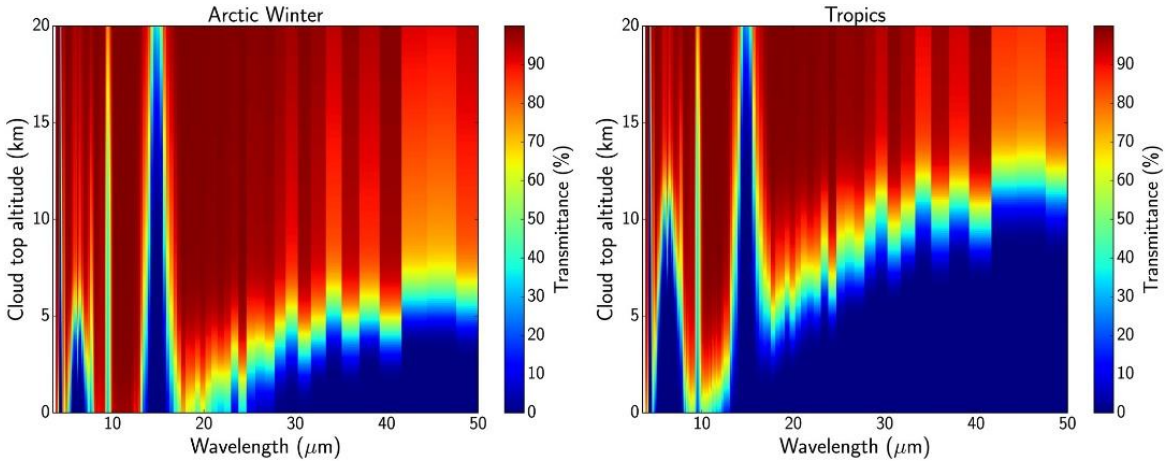

Figure 4, *from Libois and Blanchet 2017: Simulated spectral atmospheric transmittance between the top of a cloud and the TOA as a function of cloud top altitude, for Arctic winter and tropical conditions. The simulations were performed at 15 cm^{-1} spectral resolution*

In the Arctic, transmissivity is strong above 5 km (>60%) through 50 μm; in the tropics, transmissivity is relatively strong above 10 km through 50 μm and between 5 and 10 km until around 40 μm. In the spectral region between 20 and 40 μm, the height at which this strong transmissivity is present steadily increases with wavelength. This steady, sloped increase (visible in **Figure 5**) means that far-infrared observations may serve as a coarse height indicator, allowing for polar atmospheric profiling using methodology similar to many other infrared sounders in use today. This characteristic of far-infrared transmissivity also offers the opportunity for identification of ice clouds and other high clouds that approach or penetrate the tropopause in both the poles and in the tropics. Deep convection in the tropics can range from 12-18 km, reaching the height of the tropical tropopause or slightly above in the case of overshooting convective tops (Bouniol et al. 2016; Tegtmeier et al. 2020; Highwood and Hoskins 1998). Corresponding high transmissivity in the far-infrared in the tropics at this level allows for explicit examination of the spectral properties of these high clouds in the far-infrared, which introduces the opportunity for enhanced particle size identification techniques.

These transmissivity characteristics, coupled with the far-infrared “dirty windows”, hold promise for the use of the far-infrared in filling in observational gaps in current remote

sensing algorithms that measure cloud phase and cloud particle size (Yang et al. 2005; Yang et al. 2003; Baran 2007; Libois and Blanchet 2017; Saito et al. 2020). Later in this analysis, we will begin to investigate this promise by looking at real data taken in this spectral region and assessing its relationship to the conventional, "clean" atmospheric window.

1.2. Radiative impacts of cloud-top properties

Taking advantage of these aspects of the far-infrared presents an exciting opportunity to retrieve new or better information about cloud composition and cloud-top properties. In order to better understand this potential, it is necessary to first characterize cloud property variability and the current understanding of the radiative effects of these variations. From this characterization, we will discuss how the far-infrared may best contribute additional information and diagnostic capabilities.

1.2.1. *Radiative properties*

Clouds affect the radiative energy budget by impacting both short- and longwave radiation. Incoming shortwave radiation is reflected by clouds with sufficiently high albedo, while outgoing radiation may be absorbed, scattered, or reflected back towards the surface of the Earth. Some radiation at some wavelengths may make it through the clouds, but clouds are opaque to longwave radiation. A broad division between thin, high cirrus clouds and low, thicker clouds may be made: thin, high cirrus clouds have a warming effect, while low, thicker clouds generally have a cooling effect (L'Ecuyer et al. 2019).

There is a strong spatial influence on the extent of cloud radiative extinction. In the tropics, the larger cloud shields associated with convective storms have a higher average albedo – and thus extinguish shortwave radiation with greater efficiency – and lower outgoing longwave radiation. This is explicitly shown in investigations of African convection (some of the deepest in the world) which shows that increasing horizontal extent in African systems

increases albedo and slightly decreases outgoing longwave radiation (Futyan et al. 2007). This size relationship also implies a relationship between the radiative properties of cirrus clouds and the lifecycle stage of the system they are attached to, as the spatial extent of a storm system is strongly related to its lifecycle stage.

Cirrus clouds have a notable impact on radiative cooling. In the tropical regions, they make up significant portions of active convective systems and create large areas of cloudiness, opaque to outgoing longwave radiation, that can significantly outlast the convection that created them (Berry and Mace 2014; Hartmann et al. 2018; Gasparini et al. 2021). The macrophysics and the microphysics in the uppermost part of these system-connected anvil clouds have a direct influence on the radiative properties of these clouds, which in turn have strong influence on the cloud radiative effect associated with these systems (Hartmann et al. 2018). These clouds alternately radiatively cool or heat the upper atmosphere in the thermal IR band (particularly, as relates to our area of study, in the far-infrared), depending on height, longevity, optical depth, geometry, and internal microphysical features (Harries et al. 2008, Slingo and Slingo 1988, Stephens et al. 1990, Stackhouse and Stephens 1991, Berry and Mace 2014; Gasparini et al. 2021). As current radiative characterizations of cirrus clouds are primarily focused on impacts in the visible and mid-infrared spectral regions (e.g. Baran 2012, Yang et al. 2015) and cirrus clouds often occur at temperatures that emit largely in the far-infrared, models that depend on accurate spectral characterization of cirrus clouds fall short without far-infrared information (Cox et al. 2010, 2015; Fox 2015; Bantges et al. 2020).

Cirrus radiative impacts vary in tandem with their properties, in particular the interrelated variations in the height of the clouds, the habit of the ice particles comprising the clouds, the size of those same particles, and the optical depth of the clouds (Yang et al. 2005; Wendisch et al. 2007; Baran et al. 2014b; Maestri et al. 2019b; Bantges et al. 2020).

The primary influence of the height of the cloud derives from the composition of the atmosphere at a given cloud height (Wendisch et al. 2007). The presence of background atmospheric gases, the temperature of the cloud, and the density of the air around the cloud can all influence the radiative impact of a cloud. Where fewer atmospheric gases are present, the composition of a cloud is more strongly influential of its radiative profile; variations in charactertics such as optical depth, habit, and size will have a stronger influence when the net scattering and absorption – and thus extinction efficiency – is not at that level strongly affected by ambient surrounding gases.

1.2.2. *Particle properties*

The habit and size of ice particles strongly impacts near and mid-infrared as well as visible cloud radiative emission spectra. Cloud microphysical and optical depth retrievals must take these impacts into account, and may suffer as a result. To explore some of the ways in which far-infrared measurements may have the capacity to alleviate some of these shortfalls, we will first elaborate briefly on how mid- and near-infrared radiative effects are impacted by cloud microphysical properties. In general, larger particle sizes are associated with colder brightness temperatures throughout the electromagnetic spectrum (Yue and Liou 2009; Baran 2005). This association may also strengthen the relationship between optical depths and colder brightness temperatures: greater optical depths are associated with colder brightness temperatures (Wei et al. 2004), but increasing the mean effective diameter strengthens this association.

This analysis is complicated by the inclusion of habit effects. Cirrus clouds, unlike water clouds, are largely composed of non-spherical ice crystals (Korolev et al. 2001; Baran 2005; Sassen et al. 2003; Heymsfield et al. 2017), which complicates any analysis that may need an accurate assessment of particle size: what habit dimension is appropriate to use when they may vary greatly?

An analysis by Wendisch et al. (2007) of near-infrared and visible particle characteristics finds that in the case of high cirrus clouds, habit has a distinct impact on the upwelling irradiance at the top of the cloud, but in the case of lower cirrus clouds, this impact is far less pronounced. This relationship is found to be mostly dependent on the altitude of the cloud and the characteristics of the atmospheric background emission; where the cloud is higher, the temperature colder, and the presence of water vapor diminished, variation in ice crystal habit has a more prominent impact on radiative extinction.

Wendisch et al. (2007) also describe a slight dependence on cloud optical thickness, likely owing to the difference in the prominence of single-scattering between optically thin and optically thick clouds, but that this relationship is not strong. In the case of higher cirrus clouds, the impact of habit is most pronounced in the longwave window channels (10-12 μm), where the upwelling irradiance at cloud-top varies between ~3 W/ m^2μm for a droxtal habit and ~28 W/m^2μm for aggregate ice crystals. This effect is diminished somewhat as we approach the far-infrared region, where habit seems to have less of an impact, likely due to the particle size relative to the wavelength. This decreased habit significance means that retrieval algorithms making use of far-infrared data can make more reliable assumptions about habits. In shorter wavelengths, nearer the dirty window, a spherical assumption is unreliable, particularly for ice clouds (Baran 2005), but far-infrared measurements may also present an opportunity to retrieve size-distribution information that can help to alleviate this effect – something current mid-infrared measurements are unable to do (Baran 2005).

Particle size, for optically thick clouds, is also potentially more differentiable in the far-infrared (Yang et al. 2003); these optically thick clouds have proven to be particularly confounding in nighttime retrievals, where decreased differences between brightness temperatures in the mid-infrared hamper particle size detections. Optically thin clouds may also be more distinguishable in the far-infrared.

1.3. Current mid-infrared remote sensing techniques

In order to take advantage of the new possibilities provided by far-infrared observations, we will attempt to build on current mid-infrared remote sensing techniques to detect and diagnose cloud-top properties. Currently, there are two prevalent satellite remote sensing techniques for the detection of cloud properties, both of which take advantage of the differing absorption properties present in different wavelength measurements. A solar band methodology (Hansen and Pollack, 1970) infers cloud optical thickness and effective particle size from solar wavelengths; it uses the relationship between radiances and brightness temperatures recorded by a weakly absorbing near-infrared or visible band and a moderately absorbing shortwave band to create lookup tables that provide effective particle diameter isolines. This method works because in the visible band, scattering is dominant and reflectance is primarily dependent on optical depth. In the moderately absorbing band, extinction also depends on absorption, creating an additional dependence on effective diameter that can be exploited to diagnose particle size signatures (Yang et al. 2015). It suffers, however, in two primary regimes: where optical depth is small and the isolines converge, and where the solar zenith angle is so high that the solar band is unavailable: all night-time settings and many high-latitude geostationary satellite contexts. It is also relevant to consider that this method is highly dependent on particle habits and vertical variations in crystal habit and size may complicate retrievals under this methodology (Yang et al. 2001).

Some of these weaknesses may be alleviated with the use of a methodology dependent solely on infrared bands, which remain useful at night and have a less pronounced dependence on habit in some habit regimes as wavelengths become longer relative to particle size (Wendsich et al. 2007). This methodology is known as the split-window method (Inoue, 1985). It takes advantage of the difference in ice absorption characteristics in the mid-infrared window (between 10 and 12 μm) to make inferences about particle size. In some channels in the

window band, extinction is dominated by absorption, not scattering. The brightness temperature difference (BTD) between two different wavelengths in the window band can thus provide additional information about scattering extinction observed in these bands. The relationship between a window-band brightness temperature and two window-band brightness temperature differences creates isolines that can provide information about particle size and optical depth. This method is sensitive to more optically thin clouds than the solar method, but struggles when clouds are particularly optically thick, optically thin, or when effective diameters are particularly large (>50 μm). At large optical depths, the IR radiances used in this method are saturated (Yang et al. 2015), while at large effective diameters, the difference in BTD values is small enough that effective retrieval becomes difficult.

A useful visualization of the principle behind the split-window technique is shown in **Figure 5**, which will be helpful when considering the ways the far-infrared can enhance the information provided by (and neglected by) current split-window techniques.

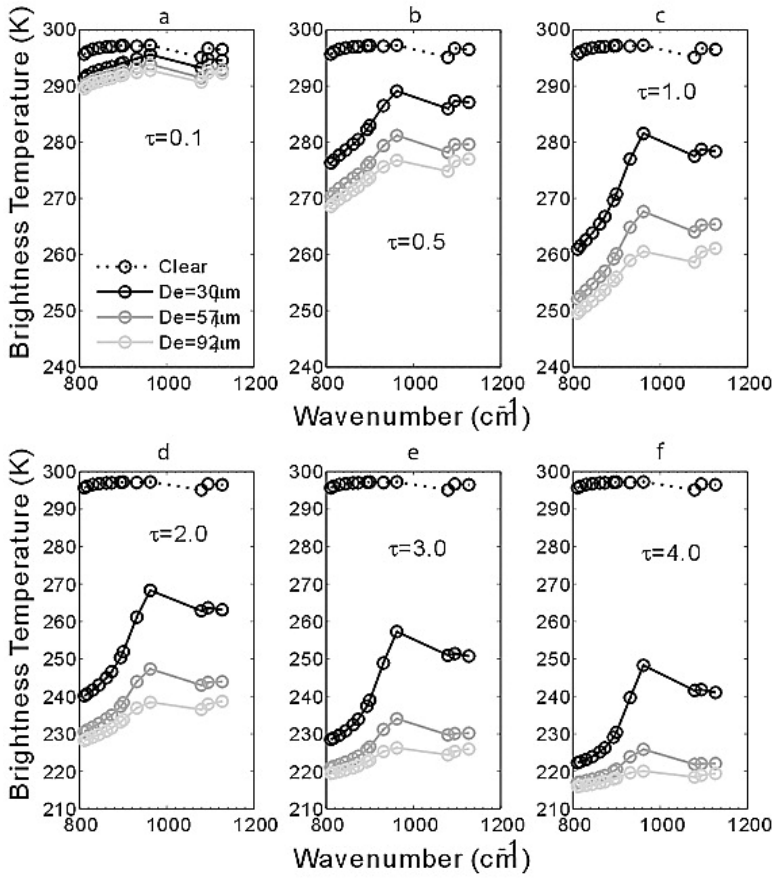

Figure 5, *from Yue and Liou 2009: Sensitivity of the sub-band brightness temperature spectra to variation in optical depth and mean effective diameter for optical depths of (a) 0.1, (b) 0.5, (c) 1.0, (d) 2.0, (e) 3.0, (f) 4.0 in a standard tropical atmosphere. Surface and cloud temperature were set to be 300 K and 200 K, respectively; circles indicate the position of each sub-band. Black, gray, and light gray solid lines indicate a cirrus layer with mean effective diameters of 30, 57, and 92 μm, respectively. Clear sky brightness temperature spectrum (τ = 0) is also shown by the dashed line for comparison purposes.*

Figure 5, from Yue and Liou (2009), shows us variation in window channel brightness temperatures for a variety of different particle sizes (largest particles at the bottom, smallest at the top, with a clear-sky baseline) across a range of optical depths. There are a few key features in this figure that highlight the theory behind the split-window technique. For all particle sizes and at all optical depths, there is a strong variation in brightness temperature throughout the window channels; this variation in brightness temperature forms the backbone of the split-window technique discussed prior.

As the optical depth increases, the measured brightness temperature decreases for all particle sizes and the separation between these recorded brightness temperatures becomes more pronounced between very large particles and small particles. As optical depth becomes larger,

the brightness temperature differences between larger particles flatten across wavelengths and particles are more difficult to distinguish. Similarly, when optical depth is small, the brightness temperature differences between all particles become small. When optical depth becomes small or when wavelengths grow larger, this separation becomes distinct. These brightness temperature differences, in the optical depth ranges where they remain distinct, can be useful in microphysical retrievals. In larger particles, the difference is less pronounced at smaller wavenumbers (longer wavelengths), but it remains visible. For larger particles, the difference between brightness temperature measured at different wavenumbers is also less prominent in longer wavelengths (wavenumbers less than 1000 cm^{-1}), while the gap between sub-1000 and 1000+ wavenumbers remains quite discernible at all effective diameters. It may be assumed that at larger optical depths, or with less distinct effective diameters, these differences become so small as to be within range of error for each measurement, limiting the usefulness of such retrievals for microphysical properties.

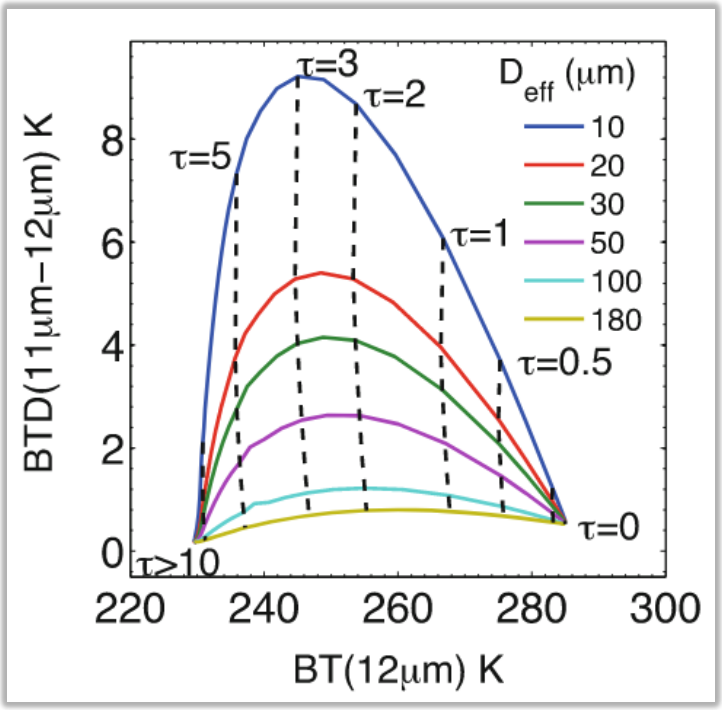

Figure 6, *from Yang et al. 2015: Relationship between simulated 12 μm VIIRS band brightness temperature (x-axis) and the brightness temperature difference between 11 μm and 12 μm VIIRS bands.*

The split-window technique, shown graphically in **Figure 6** from Yang et al. 2015, follows from the microphysical variations displayed in Yue and Liou 2009. This method, proposed by Inoue in 1985, takes advantage of wavelength-based variation in brightness temperature, driven (as shown above) by microphysical property variations, to retrieve information about particle size and optical depth. The brightness temperature at 12 μm displays a strong dependence on optical depth, but the brightness temperature difference between 11 and 12 μm is dependent on both optical depth and particle size. The relationship between these two values – the 11-12 μm BTD and the 12 μm window channel – can be used to create a lookup table to provide information about particle size and optical depth (e.g. Yang et al 2005). The arched lines represent isolines of effective particle size, increasing as brightness temperature differences grow smaller, and the dashed lines show optical depth isolines, which increase monotonically as brightness temperatures decrease. This method loses efficacy when particle sizes are particularly large, as we saw the decrease in discernibly different BTDs, and also when optical depth is large or small, as radiances become saturated to create the pinched ends of the arches we see here. The shape of those arches also depends on particle habit.

As we will investigate later in this thesis, the far-infrared may provide a good baseline for filling in night-time and property extrema gaps left by the constraints of current mid-infrared split-window techniques. In particular, the far-infrared may be capable of isolating optical depth and particle size signatures from each other and of refining retrieval algorithms where solar radiances are not available.

1.4. Relevance of convection/deep convection

While PREFIRE is a polar-focused mission, it is still important to expand far-infrared characterization beyond the poles and into the tropics and mid-latitudes. In this study, we focus on deep convection as that is the primary source of ice clouds at lower latitudes. Deep

convective clouds are tall enough to have significant far-infrared signatures and a strong radiative impact, both locally and globally. The cirrus anvil clouds associated with deep convection, particularly in the tropics, weigh strongly in the top-of-atmosphere radiative budget (Feng et al. 2011; L'Ecuyer et al. 2019) and characterizing these clouds in the far-infrared will provide a dimension of analysis that is currently inaccessible.

Cirrus anvil clouds are also associated with high-impact weather and represent a source of multiple frequently-studied cloud feedbacks. At the local level, tropopause-penetrating convection has also been observed to cause localized warming in the upper troposphere and cooling in the lower stratosphere; at the global level, tropopause-penetrating convection contributes strongly to variations or regulation of water vapor, chemical constituents, and tropospheric and stratospheric thermal structure (Xian and Fu 2015).

We, therefore, seek to apply PREFIRE data to deep convection to contribute to addressing these important problems. This research will explore PREFIRE cloud detection and retrievals in the mid-latitudes and tropics, focusing on clouds associated with deep convection, to enhance the global utility of PREFIRE.

Given the wide range of potential lower-latitude PREFIRE applications, we will narrow our scope of interest to initial explorations into four main questions, which the bulk of this thesis will be spent answering:

1. Can we identify convective ice clouds with PREFIRE measurements?
2. How does the full emission spectrum vary across different storm types and regions?
3. How can the far-infrared enhance modern mid-infrared ice cloud property retrievals?
4. Can we begin to incorporate the lifecycle stage of the storm into our analysis?

In Chapter 2, we will introduce the PREFIRE mission and associated dataset, which will form the bulk of the data to be analyzed throughout this work. In Chapter 3, we will introduce the

convection-finding methodology that will allow us to identify case studies with which to answer the questions listed above. In Chapter 4, we will seek to characterize how the full emission spectrum, particularly the as-yet-undocumented far-infrared region, varies across different storm types and regions, using regional case studies to identify several different convective and spectral archetypes and begin to assess how these identified far-infrared characteristics contribute to the overall radiative impact of the storm. In Chapter 5, we will begin to explore how the far-infrared may be able to enhance modern mid-infrared ice cloud property retrievals, which struggle in a few key places that longer-wavelength measurements are uniquely capable of compensating for. Based on our findings in Chapters 4 and 5, Chapter 6 will propose a new methodology for the identification of convection using PREFIRE's far-infrared channels. Finally, in Chapter 7, we will take the first steps towards identifying the lifecycle stage of specifically storms identified by PREFIRE; given the variation in morphology and cloud type over the course of a storm and the documented impact this has on cloud radiative effects, it stands to reason that storms at different lifecycle stages may have differing far-infrared signatures. Investigating this question requires the development of a technique that can identify the storm lifecycle stage tied directly to PREFIRE measurements.

Chapter 2. Data

We use two datasets throughout this study. The primary dataset is PREFIRE and its associated products, which will be described in Section 2.1. PREFIRE, as a polar-orbiting satellite, is necessarily temporally and spatially limited in terms of its observations; to compensate for these limitations, we bring in window-channel radiances from the geostatioanry ring (similar to Heidinger et al. 2025), which consists of data acquired from GOES-West and East (including its April 2025 transition between GOES-16 and GOES-19), METEOSAT-9 and 11, and Himawari-9. These measurements will serve as a truth dataset for effective satellite geolocation (discussed further in Section 2.2 of this chapter) and add

necessary temporal and spatial context to case study analysis, such as the lifecycle stage and spatial extent of storms, to ensure that spectral characterizations are adequately contextualized with the environment around them. In order to best determine the utility of particular cases of far-infrared data for particle size and cloud optical depth retrieval (Chapter 5), Level 2 cloud particle size, cloud optical depth, and cloud phase products from the GOES series of satellites (Heidinger et al. 2020) are also introduced as truth datasets.

2.1 PREFIRE

PREFIRE is the first polar-orbiting satellite to conduct spaceborne observations of the far-infrared (L'Ecuyer et al. 2021). Launched in May and June 2024 from Mahia, Aotearoa (New Zealand) to observe the polar regions of Earth, it currently accounts for nearly two years of continuous far-infrared data collection.

PREFIRE consists of two 6U CubeSats (SAT1 and SAT2) in asynchronous polar low-earth orbits, equipped with a Thermal InfraRed Spectrometer (TIRS) with 64 channels capable of measuring radiances from 5 to the 54 μm (2000- 185.2 cm^{-1}) at a spectral resolution of approximately 0.84 μm every 0.7 s. TIRS footprints have a spatial resolution of 11-30 km, with ground spacing of approximately 8 km between eight cross-track fields of view, which we will refer to as individual "scenes", and a horizontal swath width of approximately 250 km. Close spatial sampling in the instrument means that a given point on the ground may be sampled as many as 7 times consecutively.

PREFIRE location data has two spatial dimensions: an along-track dimension and a cross-track dimension. Cross-track refers to position horizontally across the width of the swath (across the track) and along-track refers to position along the track of the swath in the direction of orbit. Each location is indexed by its along-track and cross-track positioning in

the granule; there are 8 discrete cross-track indices and 6000-8000 discrete along-track indices in each granule.

Each satellite observes a given location roughly every 12 hours, with intersections (co-located ground scenes) between the satellites occurring in specified locations with as little as 0 or as many as 12 hours in between observations. The local time of an overpass for SAT1, launched in June 2024, is approximately 03:00 and 15:00 (early morning and mid-afternoon); the local time of an overpass for SAT2, launched in May 2024, is approximately 08:00 and 20:00 (mid-morning and late evening).

While the TIRS instruments were initially designed to be identical, slight differences in instrument build, calibration, and maintenance resulted in variations between the wavelengths measured across each satellites. For ease of reference, the TIRS channels are divided into four broad categories: mid-IR 1 (MIR-1), consisting of channels 1-8 (SAT1: 3.92-5.51 μm; SAT2: 4.47-6.31 μm), mid-IR 2 (MIR-2), consisting of channels 9-17 (SAT1: 8.4 - 13.04 μm; SAT2: 9.29 - 13.87 μm), far-IR 1 (FIR-1), consisting of channels 18-34 (SAT1: 15.96-28.23 μm; SAT2: 16.89-29.45 μm), and far-IR 2 (FIR-2), consisting of channels 34-63 (SAT1: 31.16 - 52.66 μm; SAT2: 32.17 - 54.11 μm). **Figure 7**, below, shows these broad bands over a SAT1 clear-sky spectrum, with significant spectral regions highlighted for ease of reference throughout this work. A full table containing the channels and their corresponding wavelengths for each satellite is printed in Appendix A. To maintain channel consistency across case studies, all cases for this work use data from SAT1. Throughout this work, we will refer to these individual filter bands by their acronyms (MIR-1, MIR-2, FIR-1, FIR-2) but will write out “far-infrared” and “mid-infrared” when discussing the broader categories.

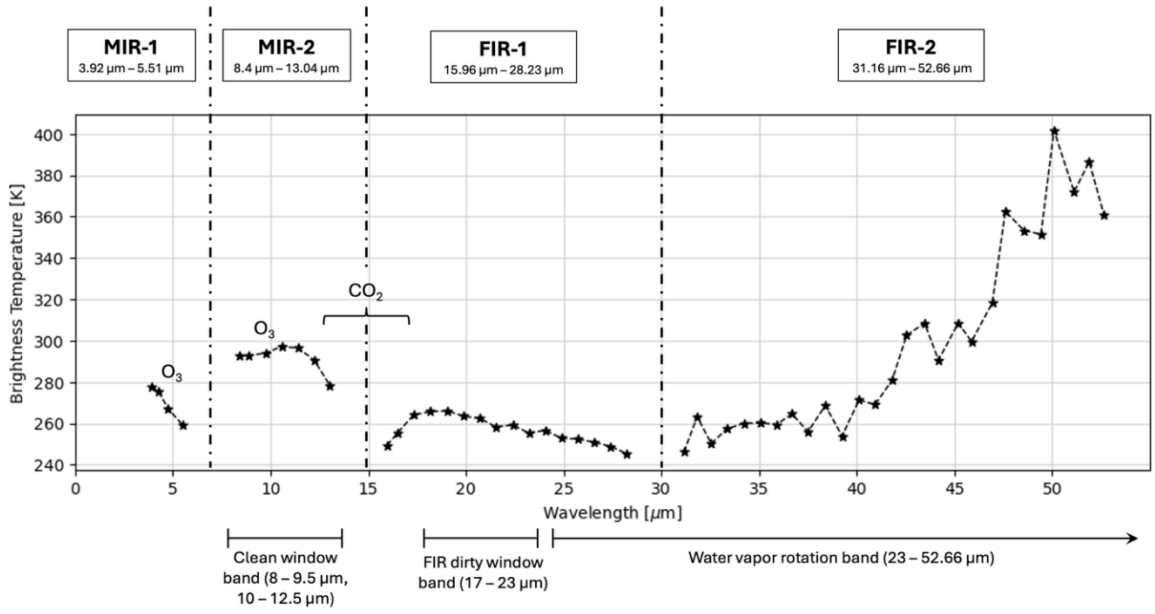

Figure 7: *Clear-sky sample spectrum, highlighting SAT1 measurement bands (top), relevant constituent absorption bands, and window bands (bottom). The FIR-2 band remains relatively untrustworthy (as seen in the unphysical brightness temperature measurements), though the PREFIRE data team is actively working to retrieve science-quality data from FIR-2 measurements.*

The PREFIRE data used in this study comes from Version 1 PREFIRE Level 1B radiances, which are publicly available as of May 2025. These Level 1 granules, consisting of one full orbit of either SAT1 or SAT2, provide longitude, latitude, radiance, and brightness temperature data. Data quality flags are available for both radiances and brightness temperature, with flags of 0, 1, and 2 indicating good quality data, unknown quality data, and bad data, respectively. For the purposes of this study, only data flagged as 0, or "good quality", is trusted in absolute terms; data flagged as 1, or "unknown quality", may be used with appropriate caution. As of March 2026, all wavelengths longer than 28.23 µm (the end of the FIR-1 band) are unavailable for research purposes due to instrument noise and calibration issues; therefore, for this project we restrict our analysis to MIR-1, MIR-2, and FIR-1. Other data may be unavailable for orbital or mechanical reasons; while much of the FIR-1 is available across all scenes for SAT1, in both satellites issues with eclipse entry and exit have arisen that necessitate data quality flags.

As PREFIRE progresses through its mission and on to proposed future missions, data processing will improve to increase the volume of good quality data and decrease the volume of moderate and bad quality data included in public data releases. In version 2.0, which should be released in the upcoming months, much of this quality-flag 1 data should be recovered through future processing.

2.1.1. Supplemental PREFIRE products

Two supplemental PREFIRE datasets will be used in support of this work: Anc-Sat and Aux-Met (Mattingly; Hokanson Wagner 2025). Anc-Sat collocates PREFIRE tracks with geostationary data from GOES-East and West, METEOSAT-9 and 11, and Himawari-9, producing a truth dataset showing approximately what PREFIRE should have recorded when it passed over the selected comparison region. Aux-Met collocates PREFIRE tracks with VIIRS satellite data and GEOS-IT analyses to add additional meteorological and environmental context to PREFIRE data, particularly in the vertical dimension, which PREFIRE observations by nature lack. Anc-Sat will be used primarily for geolocation purposes; Aux-Met will be used to provide tropopause height diagnostics and vertical profile information where relevant to case studies.

2.1.2. Geolocation

It was determined in the initial stages of the in-orbit check-out (commenced once the satellite was in-orbit) that the GPS in SAT1 was faulty to the point of untenability and it would be necessary to develop other methods of geolocation. The current PREFIRE geolocation methodology uses a two-line element dataset (TLE) to predict the location of the satellite over the course of the next 24 hours of orbits. The accuracy of TLE data is not sufficient for the degree of precision PREFIRE requires, as in-orbit variations in orbital conditions may compound to produce along-track error that will cause the satellite to deviate from a computed orbit. It is thus necessary to externally validate TLE predictions with the use of a

truth dataset. In this instance, the truth dataset comes from the geostationary satellite ring; PREFIRE granules are collocated with geostationary observations from NOAA GOES-East and West, METEOSAT-9 and 11, and Himawari-9 at regions that are likely to produce high contrast in brightness temperatures, such as along coastlines or at a desert/land contrast point.

To identify the most appropriate actual geolocation for the PREFIRE granule, shifted PREFIRE and Anc-Sat files are created by translating data in the along-track direction to correct for inaccurate along-track predictions. The shifted Anc-Sat files are then differenced with the PREFIRE granules representing the same along-track shift to determine which along-track shift most accurately matches the actual ground location of PREFIRE data. The shifted PREFIRE granule with the least difference from its corresponding shifted Anc-Sat file is presumed to be the “correct” shift and the original PREFIRE data files are modified to reflect this correct location instead of the inaccurate TLE prediction. A demonstration of this methodology is shown in **Figure 8.**

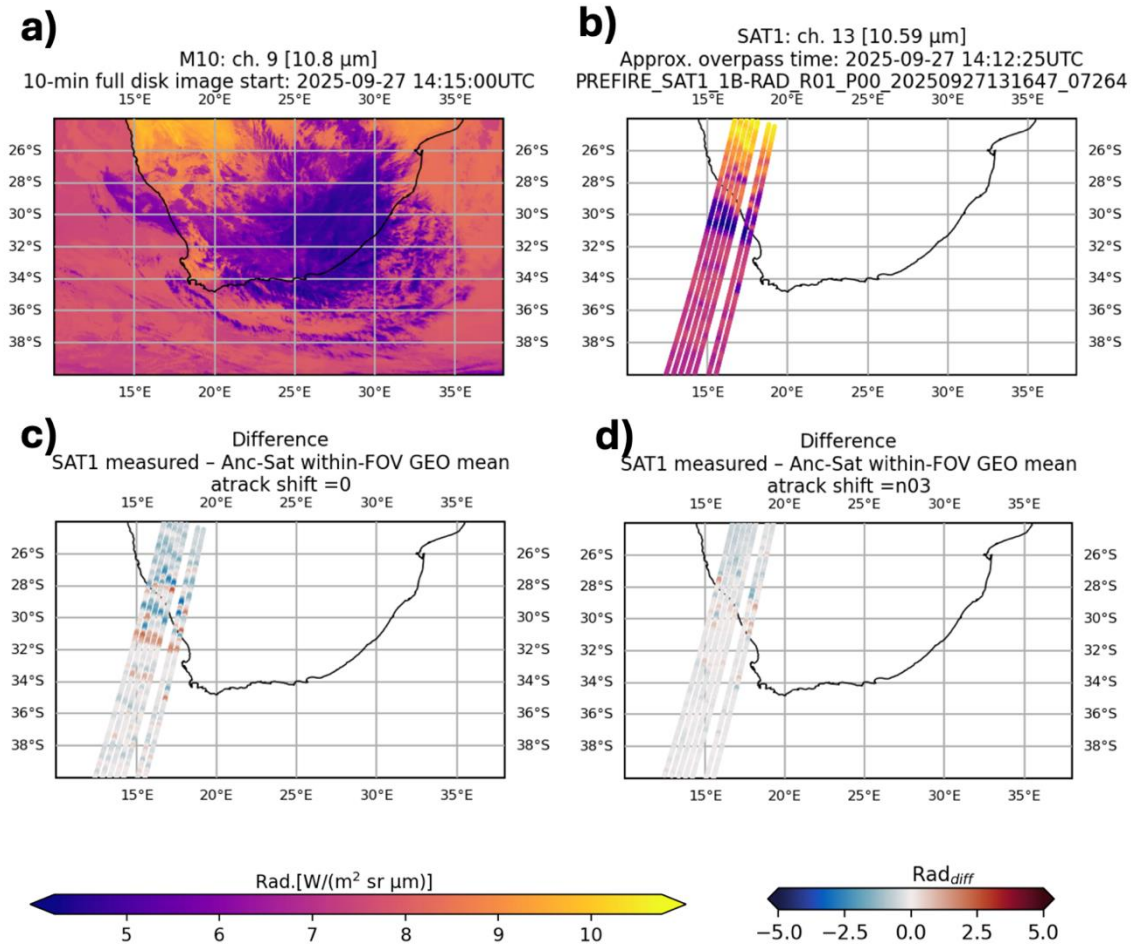

***Figure 8**: Example of SAT1 geolocation methodology for a case over South Africa. In (a), Meteosat-10 radiances are shown; in (b), SAT1 radiances for the same location, per TLE predictions, are shown. In (c), the difference between SAT1 measured radiances and Anc-Sat radiances (Meteosat-10 data interpolated onto SAT1 tracks) is shown. In (d), the difference between SAT1 measured radiances and Anc-Sat radiances, shifted -3 along-track indices, is shown. It is evident from this comparison that the shift performed in (d) results in measurements much closer to the truth dataset and the SAT1 files produced for this overpass will use this shift to correct the geolocation error.*

This procedure was validated by testing its performance on data from SAT2. Comparing the accuracy of this procedure on SAT2 data, where it was possible to validate its conclusions with actual GPS data, was instrumental in verifying its operational efficacy. The GPS on SAT2 did eventually also degrade and, as of August of 2024, is no longer operational; both satellites therefore currently use this geolocation method instead of a GPS. Because it takes significant computing power to generate Anc-Sat granules for each PREFIRE granule, the geolocation process is not run as a continuous part of the PREFIRE data processing. Appropriate shifts are instead determined on semi-monthly basis, which necessitates

occasional manual shifting of the PREFIRE data based on comparison with geostationary data.

2.1.2 TIRS processing

For all granules used within this work, preliminary processing was performed to ensure good-quality data and to smooth out some instrument noise. The current convection-seeking algorithm, described in Chapter 3, screens for solely quality flag-0 data, as it requires the use of absolute values of radiances and quality flag-1 data is not universally reliable for quantitative usage. When performing case study analysis, however, in the case of storms that were identified through other means such as visual inspection of geostationary data or personal experience with the storm in question, some quality flag-1 data was available. The usability of quality flag-1 data is variable, with some data completely unusable in the FIR-2 due to gratuitous instrument noise while other data is quality-flagged 1 for miscellaneous orbit- or instrument-related reasons. Quality flag-1 data that may be used for our purposes is generally data found in the eclipse exit, where thermal anomalies associated with the eclipse of the sun by the Earth may influence the absolute values recorded but preserve the relative values measured by different channels. In general, data was screened for quality flag 0 ("good" data); the advice of the PREFIRE data team was that quality flag-1 data was only acceptable for case study analyses, where the primary interest was qualitative spectral characteristics and relative differences between channels.

Screened data was also averaged along-track in each channel, taking advantage of the significant overlap in PREFIRE fields of view: each area that a PREFIRE track is able to image is captured roughly 7 times. Averaging along-track allows us to take advantage of this spatial resampling in order to ensure that observed variations within the PREFIRE measurements are physical signals instead of instrument noise. Each footprint was averaged with the footprint before and after it; this average was then remapped onto a new set of along-

track indices to preserve location data. The latitude and longitude associated with each newly averaged footprint are the latitude and longitude information associated with the center along-track value, preserving roughly the center of the averaged information. A demonstration of this methodology is presented in Appendix B for additional clarity.

Chapter 3. Initial convection-finding algorithm and case identification

While all analysis performed in this work is based on convective case-study work, one of the primary goals for future work is to perform these analyses at a much broader scale, with many more cases across a broad range of regions, conditions, and storm sizes. This necessitates the development of a convection-finding algorithm tailored to the PREFIRE data structure and constraints. To begin, we first test PREFIRE's ability to detect convection at all: can PREFIRE measurements reach a point where convection is detectable? And does it do so in regions where this would be an expected result?

We take two months of continuous PREFIRE data from SAT1: one in July, the northern hemisphere summer, and one in January, in northern hemisphere winter, and calculated the minimum brightness temperatures recorded in each discrete SAT1 orbit. These minimum brightness temperature values are plotted according to the location where they occurred and shown in **Figure 9**.

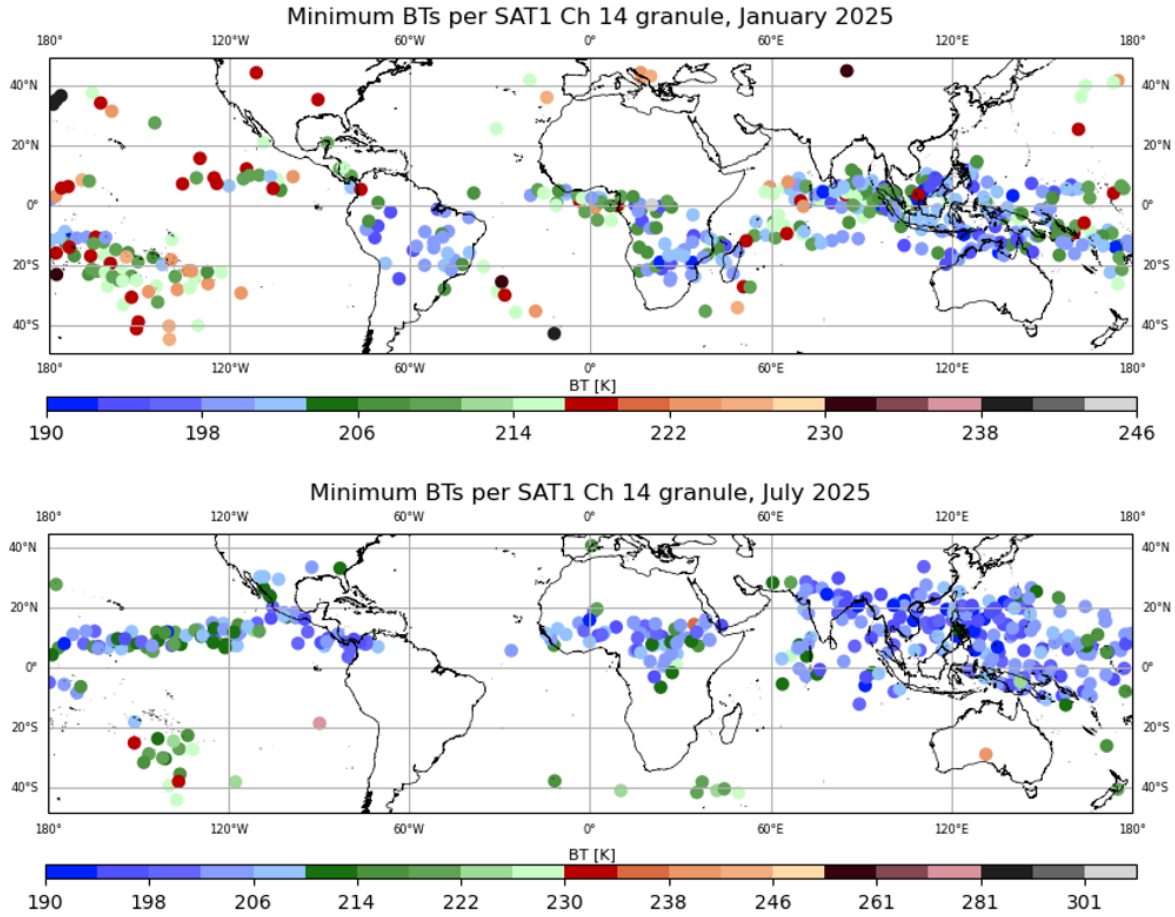

Figure 9: *The location of the minimum window-channel brightness temperature recorded in each SAT1 granule (orbit) throughout the months of January (top) and July (bottom) 2025. Dots are colored according to the measured minimum brightness temperature.*

It is clearly shown that minimum brightness temperatures are distributed in accordance to the locations in which most literature agrees tropical deep convection occurs (Houze et al. 2014; Pilewskie et al. 2024; Roca et al. 2017): central and southern Africa, the maritime continent in Brazil and over the Pacific islands, and along the ITCZ, where the seasonal shift is demonstrated between January and July. This provides confidence that PREFIRE can successfully detect the brightness temperature extremes associated with convection: PREFIRE consistently detects minimum brightness temperatures of 190-200 K, with the lowest values verging into the 180s in very high convective activity regions such as the African Congo.

Having established that PREFIRE is capable of identifying convection, the next step is to provide it with a means of filtering these extremes out into specific cases. This step will take the form of PREFIRE-tailored thresholds, a methodology based off of current thresholding strategies used to find convection in geostationary data (Bedka et al. 2021; Takahashi et al. 2021; Fiolleau and Roca 2013; Sassen et al. 2008). This premise takes advantage of the typical structure of large or moderately sized convective storms: tall, cold cloud towers called convective cores, or "hot towers" when they are tall enough that they breach the stratosphere (Pilewskie et al. 2024), surrounded by robust, high anvil ice clouds. These storms are typically extensive enough that they have significant radiative impact due to the extinction of outgoing longwave radiation; the far-infrared characteristics of these storms will be the primary focus of the case study analyses and characterizations in Chapter 4. The extinction of outgoing longwave radiation means that these high clouds appear very cold in the window channel, which allows us to perform a simple screen of window channel brightness temperatures, applying a thresholding methodology, to identify convection.

The accepted threshold for geostationary convection identification varies widely across the literature, with thresholds as low as 208 K for very deep, hot towers (Pilewskie et al. 2024) and thresholds as high as 235 K for simple identification of convection and convection-associated cloud shields (Fiolleau and Roca 2013). On the lower end, these threshold values come from the temperature of the tropopause; for very deep convection, cloud-tops may be assumed to be at or slightly above the level of the tropopause and thus the measured brightness temperature can be expected to be in agreement with the ambient temperature of the tropopause. In comparison, higher thresholds seek to identify powerful systems with extensive anvil structures; these thresholds are more effective when the goal is to identify broad mesoscale systems, where the cloud-top brightness temperatures are slightly warmer, but less effective when attempting to identify specifically the deep, tall convection that

reaches the tropopause. The initial goal for the application of this methodology to PREFIRE data is to find both extensive anvil structures and deep convection, so that initial case-study characterization of their spectral signatures can attempt to draw some differentiation between these different types of convection in the far-infrared. As a result, the convection-finding algorithm needs to be capable of threshold adjustment between not only different regions of the globe, but between different types of desired storms.

To find convection using TIRS data at an initial outset, some adjustments need to be made: the large TIRS ground footprint, necessitated by the physical limitations of measurements made at longer wavelengths, means that it is far more difficult to resolve cold temperatures at the same degree that geostationary satellites are able to. A TIRS brightness temperature measurement is consistently 10 K warmer than the geostationary satellite measurement of the same location. An example of this discrepancy is shown in **Figure 10**, which shows a PREFIRE overpass of a convective storm in the northeastern region of the United States. This inconsistency must be accounted for when designing a convection-seeking algorithm.

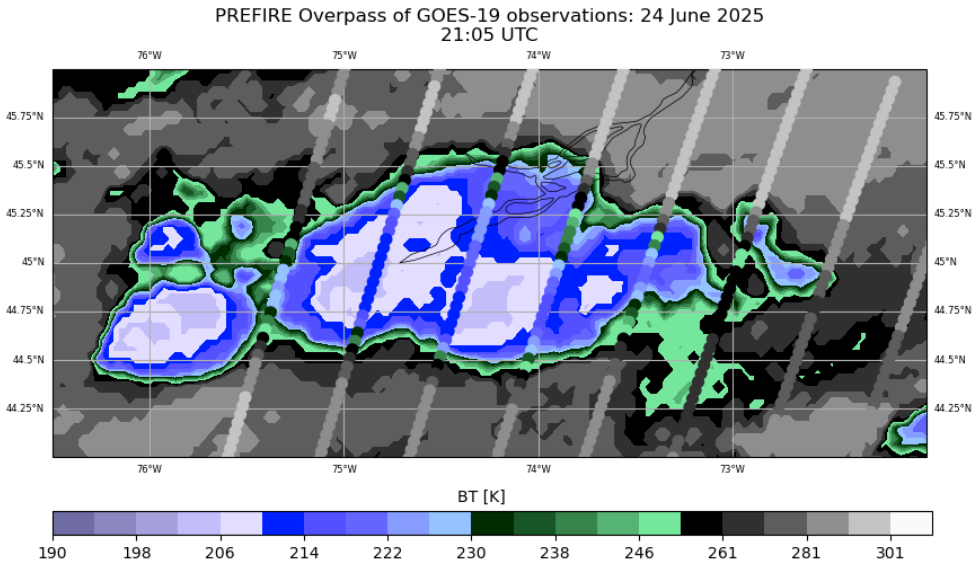

Figure 10: *PREFIRE tracks overlaid on GOES-19 brightness temperature measurements; the +10 K discrepancy can be seen as PREFIRE passes over the storm, with GOES brightness temperatures dipping as low as 200 K where PREFIRE only records brightness temperatures of no lower than 210 K.*

The thresholds used in this convection-seeking algorithm will be adaptable for particular region or case-study type desires. In a case where we may seek to identify tropopause-penetrating convection, we set a threshold targeted at finding the coldest cloud-tops. This threshold was modelled after the methodology used in Pilewskie et al. 2024, which sought to identify specifically hot towers – "any deep convective cloud with a base in the planetary boundary layer (PBL) and reaching near the upper-tropospheric outflow layer" – by analyzing the occurrence of hot towers relative to all other convective objects, defined as objects containing CloudSat-identified convective precipitation (Pilewskie and L'Ecuyer 2022). A comparison histogram using PREFIRE data composed of minimum brightness temperatures per orbit (as a parallel to hot towers) and of all recorded PREFIRE brightness temperatures (as a parallel to the convective objects) in the months is shown in **Figure 11**(b).

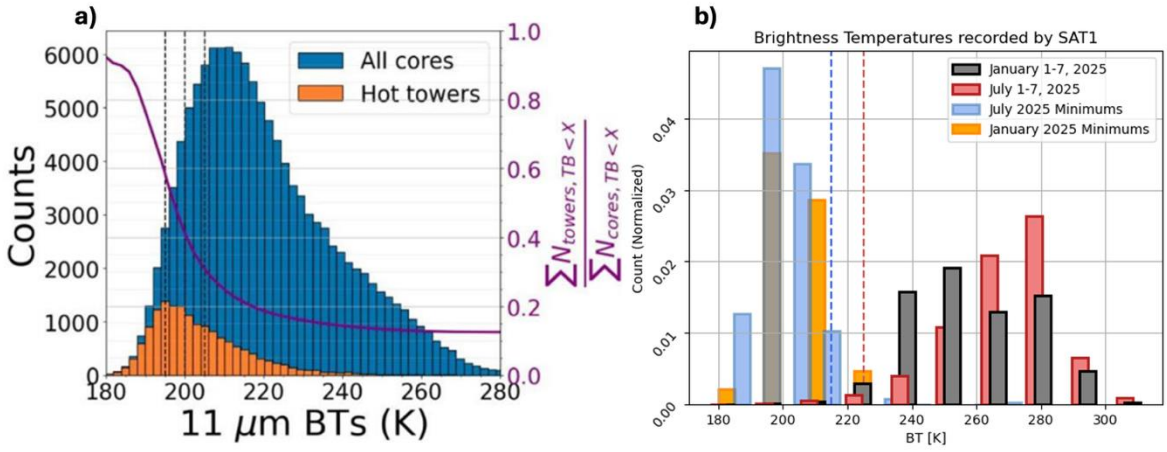

Figure 11*: Left: Distribution of minimum brightness temperatures (orange/blue bars, as in Fig. 8) and all brightness temperatures recorded from January 1-7, 2025 and July 1-7, 2025 (red/black bars). The dashed red (blue) line shows the brightness temperature thresholds chosen for January (July) applications of the initial convection-finding algorithm. Right: from Pilewskie et al. 2024, distribution of measured brightness temperatures of all cores (blue) and hot towers (orange) in the tropics.*

For this specific case, thresholds are set in an attempt to encompass the majority of brightness temperature minimums (not all, as some orbits did not pass over any regions of convection and showed minimum brightness temperatures as high as 260 K) without including the warmer brightness temperatures. These thresholds are shown by the red dashed line (for January) and the blue dashed line (for July); a threshold of 225 and 215 K, respectively.

For operational use, these thresholds are coupled with a pixel requirement: for every case where PREFIRE passes over a region meeting the threshold requirement, it is further screened to ensure that sufficient volume of PREFIRE footprints observed temperatures meeting this requirement. This was to ensure that outlier measurements or erroneously segmented storms did not skew the results, as the eventual use case for this method is to be used to automate the selection process and perform statistical analyses. This threshold was means-tested across a number of potential cases, which were checked manually to ensure validity. One of these cases, a case of particularly deep convection over the Northern Congo in April of 2025, is shown in **Figure 12**. This case in particular used a brightness temperature threshold of 215 K with a pixel requirement of 50 pixels.

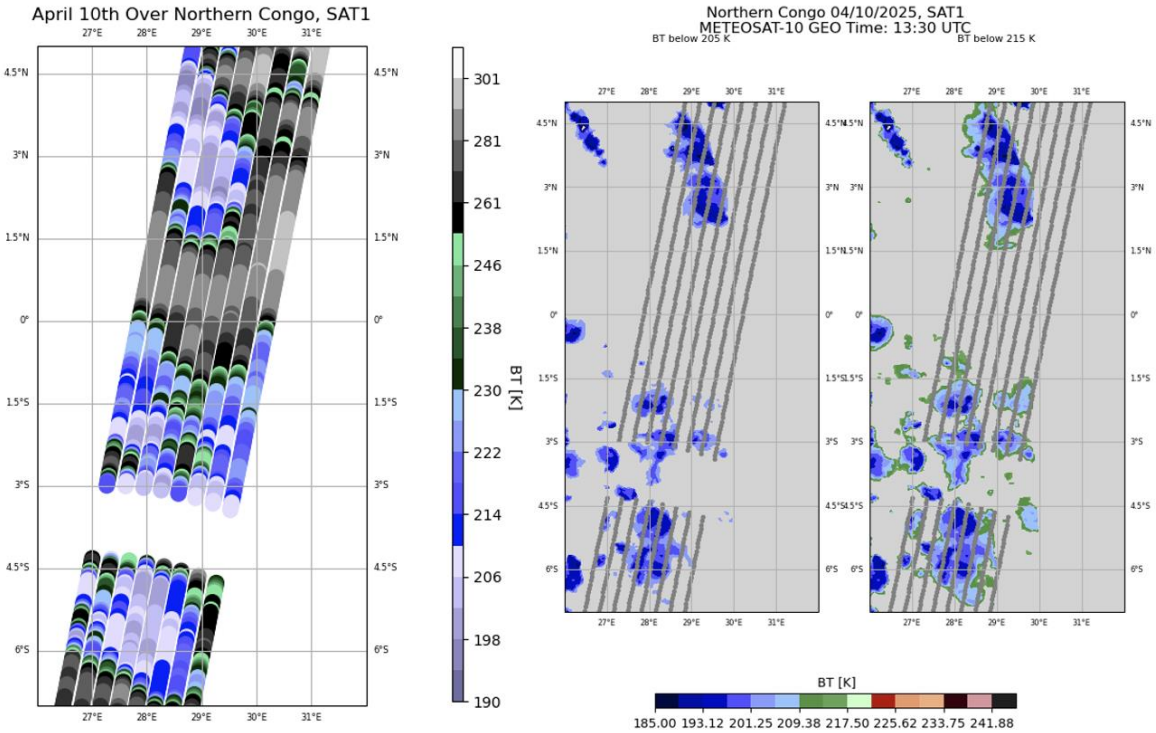

***Figure 12**: A PREFIRE overpass of deep convection in the Congo, shown with (left) brightness temperature information in the tracks and (right) tracks overlaid over GEO observations, filtered to show brightness temperatures below 205 and 215 K.*

In this case, the cold convective cores that are of interest when applying this threshold are obvious; **Figure 12**(a) shows the PREFIRE overpass, where brightness temperatures clearly

reach as low as 196 K, and **Figure 12**(b) shows filtered Meteosat-10 observations of the same scene. It is evident from this comparison that high, cold clouds dominate this scene, while warmer clouds (denoted by the green section of the colorbar) are not particularly extensive, especially in the geostationary observations, which are more precise than PREFIRE observations. The geostationary imagery indicates that PREFIRE was successful at identifying this case of rainforest deep convection; identifying other types of cases necessitates threshold adjustment based on region, case of interest, and time of year. While a more thorough analysis may be necessary to create a set of a easily implementable thresholds, we will propose an improvement on this initial methodology in Chapter 6 that will leverage the far-infrared spectral signals to be investigated in the next two chapters.

Chapter 4. Emission spectra characterization

Using case studies identified using this initial convection-finding algorithm, our attention now turns to an initial characterization of the far-infrared spectral behavior of convective storms across four different archetypes: mid-latitude continental, tropical rainforest, deep rainforest, and tropical oceanic.

4.1. Spectral dimension of convective radiative effects

This continental case is of a mature convective storm that occurred across much of the midwestern United States on April 17th and 18th, 2025. PREFIRE observed this storm twice, once in the afternoon of the 17th at 22:34 UTC, 16:34 local time, and once in the early morning of the 18th at 09:14 UTC, 03:14 local time (overpasses shown in **Figure 13**). The evolution of this storm, complete with PREFIRE overpasses, can be seen in Appendix A. This analysis will focus on the overpass in the afternoon of the 18th, which observed the full north-south and nearly the full east-west extent of the storm, including a large area of strong convection (brightness temperature < 210 K) with a large associated anvil (brightness

temperature between 210 K and 250 K). This overpass presents an interesting array of spectral features to study. We choose this instance of continental convection to observe the basic properties of convective cloud spectra and to gain an initial baseline; this is a strong, mature storm that includes all of the basic components of a convective storm, so it is useful to compare to other forms of convection elsewhere on the globe. This is also a Great Plains storm, so topographical influences on the development and nature of this convection are relatively minimal compared to other locations.

In this overpass, PREFIRE was entering the phase of its orbit where the Earth eclipses the Sun, which produces quality flag-1 data flawed by thermal anomalies; for a qualitative spectral analysis, this data is sufficient, but we will take care to avoid any quantitative interpretations or usage. In future versions of the PREFIRE product, this data will be fully recovered and a more quantitative analysis may be conducted.

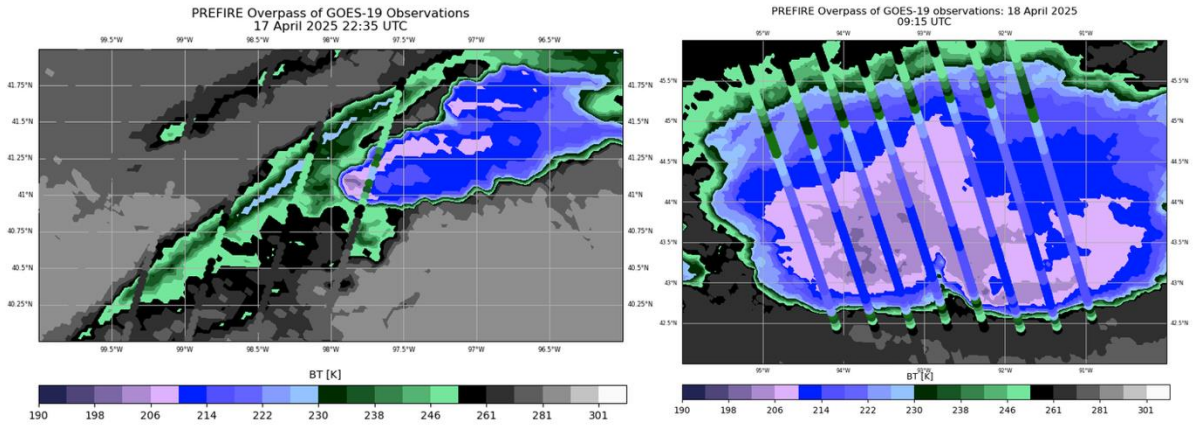

Figure 13: *Right, overpass on 4/17/2025, to be analyzed later, with timestamps showing it is a descending overpass. Left, overpass on 4/18/2025, to be analyzed here, with timestamps showing it is an ascending overpass. Scene 1 will be located on the westernmost side of the overpass, while Scene 2 is located on the easternmost side.*

Three primary spectra, the locations of which are identified in in **Figure 14**, will be analyzed for an initial baseline diagnostic. A clear-sky spectrum, highlighted by the row of pentagons, will serve as a useful initial baseline to compare convective spectra against; understanding how the mid-latitude atmosphere looks in the absence of a convective object will help to

understand the ways in which a convective object modifies the far-infrared spectrum. The location of this clear-sky spectrum was identified using the GOES Level 2 cloud mask product to verify that it was a clear-sky observation. A convective core spectrum, highlighted by the row of stars, will be compared to the clear-sky spectrum to gain an initial understanding of convective far-infrared characteristics. Finally, a spectrum from the convective anvil portion of the storm, highlighted by the row of plus signs, will be compared to both the clear-sky and convective spectra to see what this convective alteration looks like in the absence of the deep convective cores and updrafts characterizing the core of the storm.

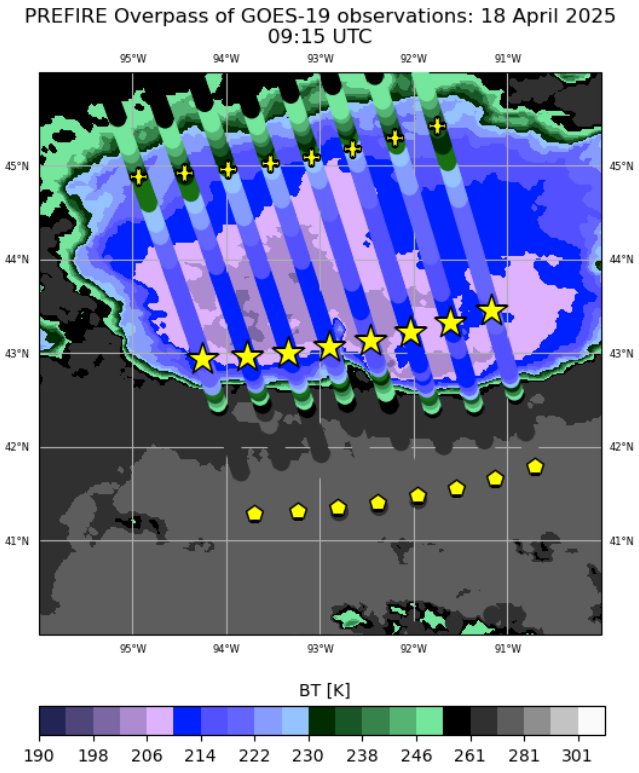

Figure 14: *PREFIRE overpass of first convective case. The background color scheme is GOES-19 window-channel brightness temperatures, while the overlaid tracks are PREFIRE SAT1 window channel brightness temperatures. Both sets of data share the same colormap, highlighting the discrepancy between PREFIRE and GOES brightness temperature observations. This is an ascending overpass, so Scene 1 is the easternmost track, while Scene 8 is the westernmost track. Pentagons: clear-sky observations; Stars: convective core observations; Plus sign: anvil observations.*

4.1.1. Clear-sky spectra

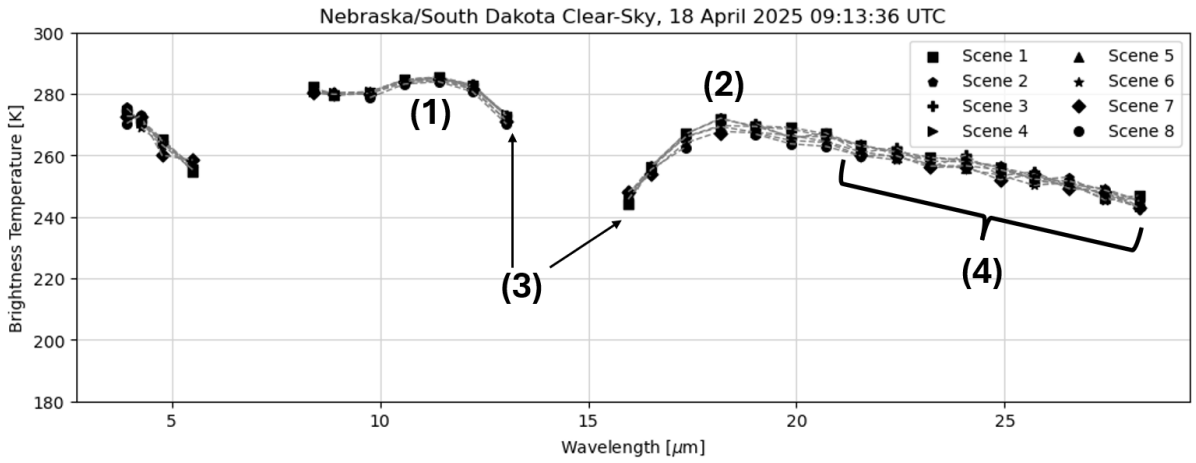

Figure 15: *Clear-sky spectrum from just south of the convective storm, with spectral features of interest marked (see text).*

The primary spectral features to note, highlighted in **Figure 15Error! Reference source not found.**, are:

(1) the mid-infrared window, shown between 9 and 13 μm

(2) the far-infrared dirty window, shown as the peak around 17 μm to around 21 μm

(3) the edges of the CO_2 absorption band, shown as the dip in the mid-infrared window and the strong increase in the far-infrared (in FIR-1) until the beginning of the dirty window band

(4) the tail of FIR-1, which moves out of the dirty window into the beginning of a water vapor absorption regime, shown by the brightness temperatures decreasing

The mid-infrared window brightness temperatures should be approximately ground-temperature. As wavelength increases into the CO_2 band at the long-wavelength edge of the MIR-2 filter, the brightness temperature begins to decrease as the CO_2 in the atmosphere blocks ground-level emission. At the short-wavelength edge of the FIR-1 filter, the long edge of the CO_2 band is visible, marked by much colder brightness temperatures than the mid-

infrared window. The far-infrared dirty window is warmer than the CO_2 absorption band but still shows notable disagreement with the clean dirty window, with a drop in BT of almost 10 K. This disagreement will provide useful contrast for future spectral signatures, as a dip this clear shows most prominently in clear-sky spectra.

4.1.2. Convective core signature

Having established this clear-sky baseline, we move on to a spectrum taken from the convection displayed further north in the overpass, denoted by the stars in **Figure 14**. To add some more environmental context to this spectrum, Next Generation Weather Radar (NEXRAD) radar reflectivity cross-sections (**Figure 17**) from the KDMX Des Moines station and an Aux-Met vertical temperature profile (**Figure 16**) are incorporated. The NEXRAD reflectivities add vertical information that can be correlated with cloud-top brightness temperatures, allowing us to identify the approximate locations of updrafts and where large particles may be present in the cloud. Prominent updrafts are inferred as high reflectivity values (corresponding to the largest particles), visible in this data as extending up to 10 km with notable reflectivity values extending up to 15 km. Per the far-infrared transmissivity shown in Libois and Blanchet (2017) (**Figure 4**), it is reasonable to expect that an far-infrared updraft spectral signatures would be detectable at cloud-tops in this height range.

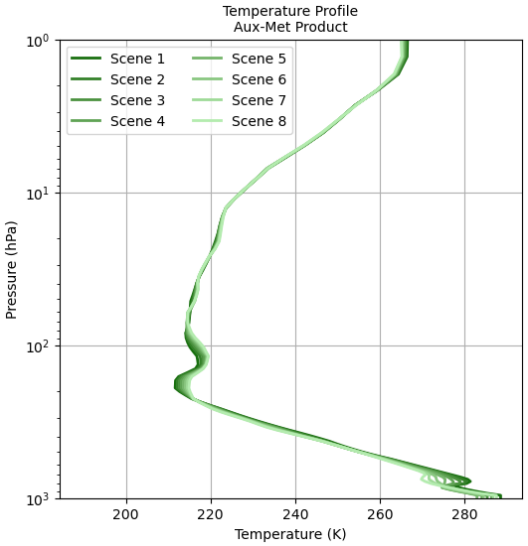

Figure 16: *Aux-Met temperature profile, showing that the temperature of the cold-point tropopause is approximately 211 K.*

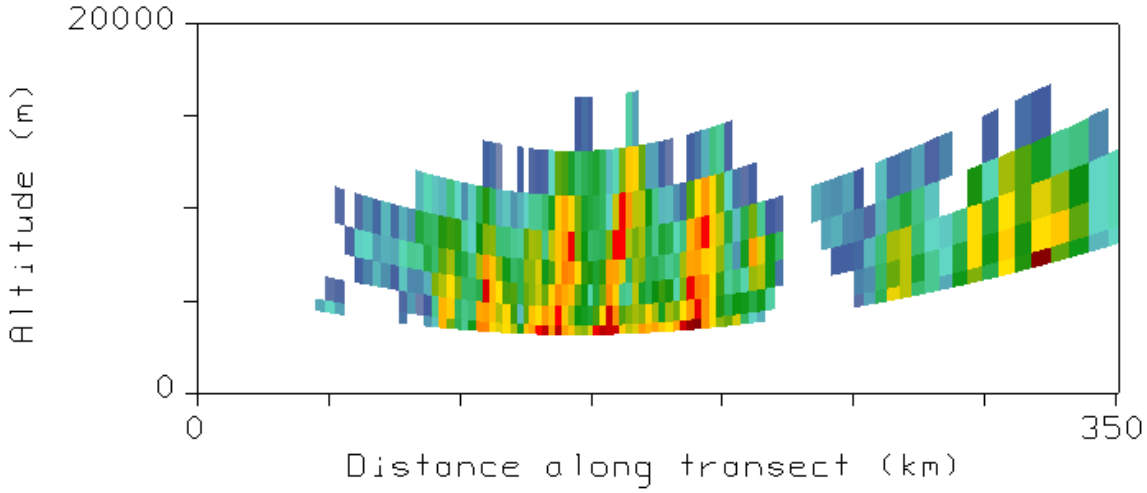

Figure 17: *Radar reflectivity cross-section taken from Des Moines station coinciding with location of stars shown in Fig 16(a).*

The Aux-Met temperature profile is incorporated in order to identify the height of the tropopause and to clarify whether PREFIRE is observing tropopause-level clouds or clouds below the tropopause. Defining the tropopause as the point at which the temperature stops decreasing with height and is instead relatively constant finds that this mid-latitude tropopause occurs at a temperature of approximately 211 K. A convective spectrum for this case, shown in **Figure 18**, has window-channel brightness temperatures of 220 K; keeping in mind the fact that PREFIRE observations are generally 5-10 K warmer than more precise

geostationary observations, it can be concluded that this spectrum represents observations of cloud-tops at or just below the level of the tropopause. With this knowledge, analyses of the far-infrared spectra may be conducted under the assumption that any signals result from either cloud-top properties (such as particle size, shape, and cloud height) or from potential stratospheric signals.

The spectrum shown in **Figure 18** represents the coldest cloud-tops PREFIRE observed in this particular storm overpass. The coldest window-channel spectra, from Scenes 2 and 3, likely represent the tops of convective cores or the clouds directly adjacent to these cores, where the updrafts are strongest and the cloud-top reaches the tropopause. Any potential particle-size signatures discernible in these spectra (which we will discuss in depth in Chapter 5) would be from the larger particles nearly at cloud-top as shown in the reflectivity data in **Figure 17**.

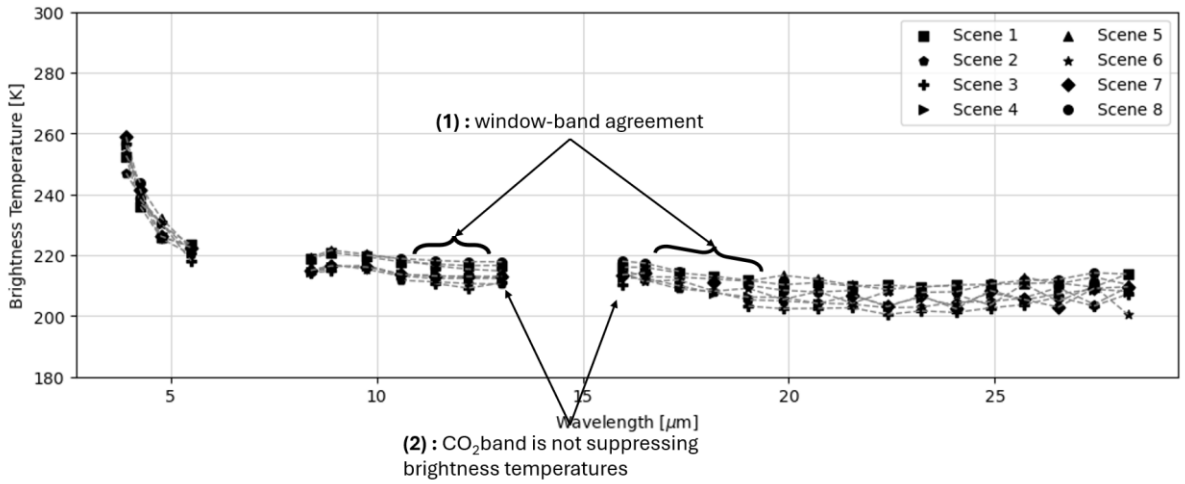

Figure 18: *Eight-track spectrum from PREFIRE observations of a convective region of the storm, as shown in Fig 14.*

A few notable features distinguish these spectra from the clear-sky spectra shown in **Figure 15**:

(1) The brightness temperatures in the mid-infrared window band and the far-infrared dirty window display notable agreement, within 5 K, particularly near the CO_2 band

(2) The CO_2 band does not display the suppressed brightness temperatures visible in the clear-sky spectra

These characteristics are indicative of high- cloud-top spectral signatures. For both CO_2 and water vapor (the confounding element that dirties the far-infrared window band), these cloud-tops are high enough that transmissivity is not impacted by the absorption properties in these bands and the dirty window band becomes, in effect, a clean window band. The brightness temperature measurement becomes roughly analogous to an air temperature measurement at cloud-top, just as in the clean window band brightness temperature; this is further reinforced by the fact that these measurements hover around 220 K – just where the Aux-Met temperature indicates the tropopause temperature is (accounting for PREFIRE footprint overestimation).

The other prominent feature in this spectrum is the convex nature of the brightness temperature measurement in most scenes as we progress out of the dirty window band and into the longer-wavelength channels where water absorption is more prominent. Convection, as noted previously, may inject water vapor into the upper troposphere and lower stratosphere. At these roughly tropopause-height clouds, it is possible that localized tropospheric water injection signatures are present in the FIR-1 band. At the longer wavelengths in this spectrum (between 20 and 25 μm), brightness temperatures decrease as increasing water vapor absorption causes the signal to originate higher in the atmosphere before beginning to increase when wavelengths are slightly longer than 25 μm. Referencing the vertical temperature profile again, this may be a result of the above-tropopause temperature behavior, where temperature decreases briefly with height before warming again in the stratosphere. This signature does not follow the same pattern as in the clear-sky spectrum, where the decrease in brightness temperatures follows a smooth slope in agreement with expectations of previously characterized far-infrared emission spectra of Earth, as

discussed in the introduction. This contrast may indicate the influence of localized tropospheric water injection, where increased water vapor directly above the convective clouds causes eliminates lower far-infrared signal and causes the spectrum to instead reflect the stratospheric lapse rate.

4.1.3. Convective anvil signature

The last signature we will use to establish our mid-latitude baseline comes from the anvil of this storm, denoted by the row of plus signs in **Figure 14**. In this spectrum, shown in **Figure 19**, the minimum MIR-2 brightness temperature does not reach below 218 K, as opposed to colder spectra taken over deeper convection, implying that these clouds do not reach the tropopause.

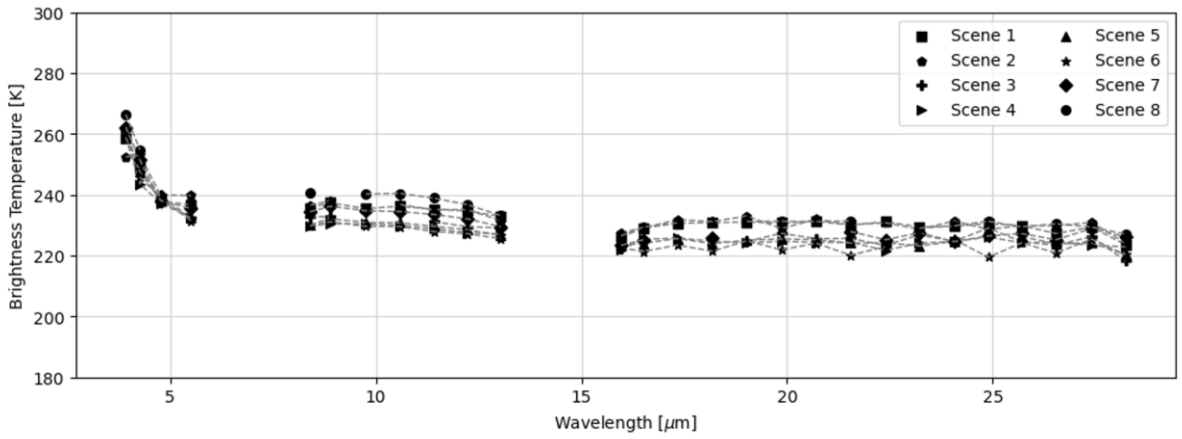

Figure 19: *As in Fig 18, but for the convective anvil.*

Here, the brightness temperatures through FIR-1 are nearly constant; in most scenes, variations are within 2 K and nearly negligible. In the MIR-2, there is only a notable decrease in temperature at the very edge of the filter, where CO_2 absorption begins to dominate. This anvil spectrum lacks the convex pattern seen in the convective spectra, where water vapor injected into the tropopause or stratosphere due to deep convection causes decreasing brightness temperatures throughout the middle of the FIR-1 filter. Instead, the water vapor absorption remains constant across the top of the anvil cloud, resulting in this flat, consistent

brightness temperature signature across the entire FIR-1 filter. This qualitative observation – that the coldest MIR-2 brightness temperatures are associated with a convex signature in the FIR-1, while the slightly warmer temperatures are associated with a flatter signature – holds across the remainder of spectral observations taken across this storm.

4.2. How does the convective spectrum change in a rainforest environment?

Having established a baseline for a case of mid-latitude continental convection, we will now investigate a case of tropical convection. This rainforest convection occurred over Brazil in the early morning hours of March 12th, 2025. The storm in question is a smaller, moderately intense, mature convective storm, which developed over the course of roughly 2 hours, intensified, and merged with surrounding convection. The full lifecycle of this storm, until its merger into surrounding complexes, is shown in Appendix A. The ascending PREFIRE overpass of this storm occurred when it had reached peak intensity. Scenes 1 and 2 observed the deep convective core and associated anvil. This analysis will examine first the clear-sky and convective core spectra, to compare with the previously characterized mid-latitude continental spectra, before examining the sharp transition between clear-sky and storm anvil at the boundary of the storm to investigate some of the structures identified in the first spectra. The locations of each spectrum are shown in **Figure 20**.

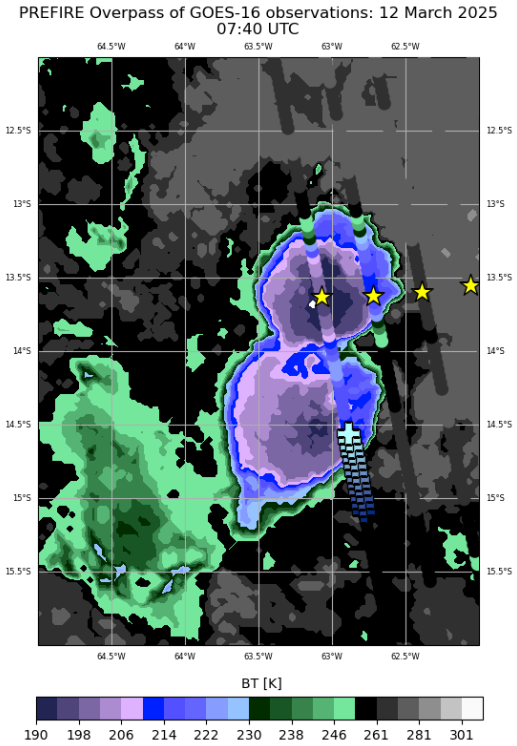

Figure 20: *PREFIRE overpass of rainforest convection. This is an ascending overpass; Scene 1 is the westernmost scene. Stars: convective core + anvil observations. Ascending line of plus signs, dark to light: observation of brightness temperature gradient over sharp temperature gradient at edge of storm.*

4.2.1. Clear-sky and convective spectra

Figure 21 shows the clear-sky (light blue) and convective spectra (dark blue) for this storm, with key points from the clear-sky spectra highlighted.

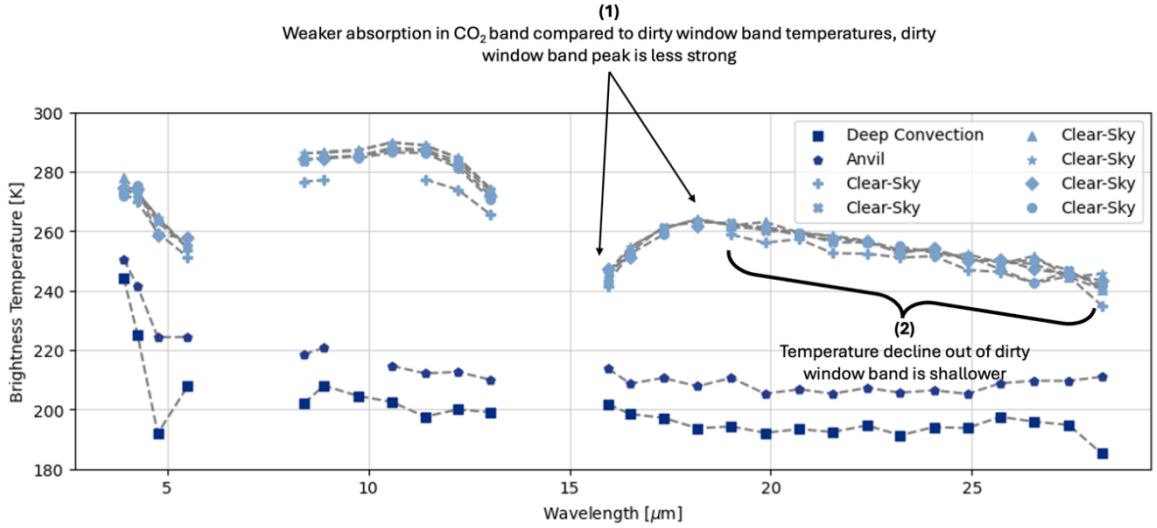

***Figure 21**: Spectra from the indicated PREFIRE tracks in (left), showing clear-sky (light blue) and convective (dark blue) spectra. The convective spectra are further split into a deep convective observation (squares) and an anvil observation (stars). Points of interest for the clear-sky spectra are marked (1) and (2); see text for details.*

In the clear-sky spectra, there are two primary differences between the mid-latitude and tropical cases:

1. Clear-sky dirty window band

In the clear-sky spectra, this tropical dirty window band distinguishes itself less from the surrounding water vapor absorption and CO_2 absorption bands: the difference between brightness temperatures in the FIR-1 CO_2 band and the dirty window band is weaker and the transition from the CO_2 band to the dirty window band into the FIR-1 water vapor absorption band is overall less distinct than in the mid-latitudes, with a difference of ~20 K as opposed to ~35 K. The transition between the mid-infrared window band and the MIR-2 CO_2 band, on the other hand, does not display this contrast. The difference between the two in the mid-latitude and tropical cases remains about the same, around 15 K. Conversely, the dirty window band in the tropical clear-sky spectra is *more* distinct from its corresponding clean window band; where in the mid-latitude spectrum, the difference between the dirty and clean window bands is as small as 15 K, in this tropical clear-sky spectrum, the difference is as large as 30 K.

This difference in the dirty window band may be due to comparatively increased humidity in the tropical region, where extinction due to water vapor is stronger. The prominence of the dirty window band may be suppressed by water vapor absorption due to this increased humidity. To assess this hypothesis, **Figure 22** compares the column water vapor Aux-Met product for both the tropical case and mid-latitude case. The environment around the tropical case is at least twice as moist as the environment around the mid-latitude case, making it feasible that this increased humidity would be the cause of this spectral signal.

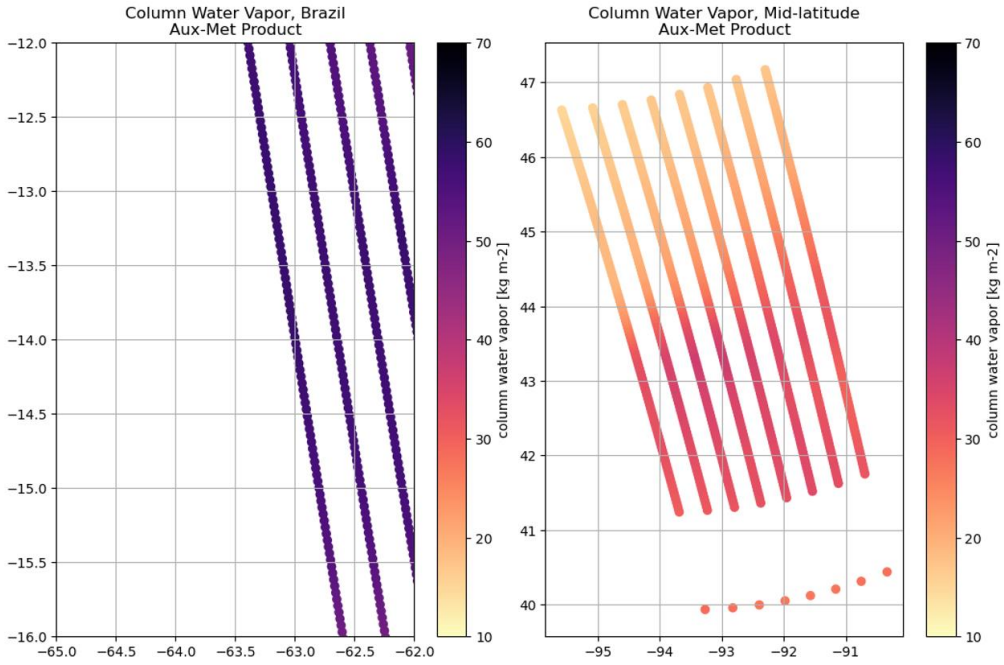

Figure 22: *The column water vapor product from PREFIRE's Aux-Met product for Brazil (left) and the mid-latitude case (right), derived from the GEOS-IT analysis. Both figures use the same colormap and scale, highlighting the difference between the mid-latitude case and the tropical case.*

2. Clear-sky water vapor absorption band

In the clear-sky spectrum water vapor absorption band, the temperature decline from the dirty window into the water vapor absorption band is much shallower, with a less pronounced difference over the span of the FIR-1 filter. In contrast to the mid-latitude clear-sky spectra, where the decrease from the dirty window to the end of the FIR-1 filter is as great as 35 K, the decrease in this spectrum is as low as 15 K and maxes out around 20 K – similar to the

difference between the dirty window and the FIR-1 CO_2 band. The slope of this decrease appears as constant as the mid-latitude slope, just shallower.

There are also notable differences between the core and anvil spectra in this tropical case as compared to the mid-latitude case, highlighted in **Figure 23**:

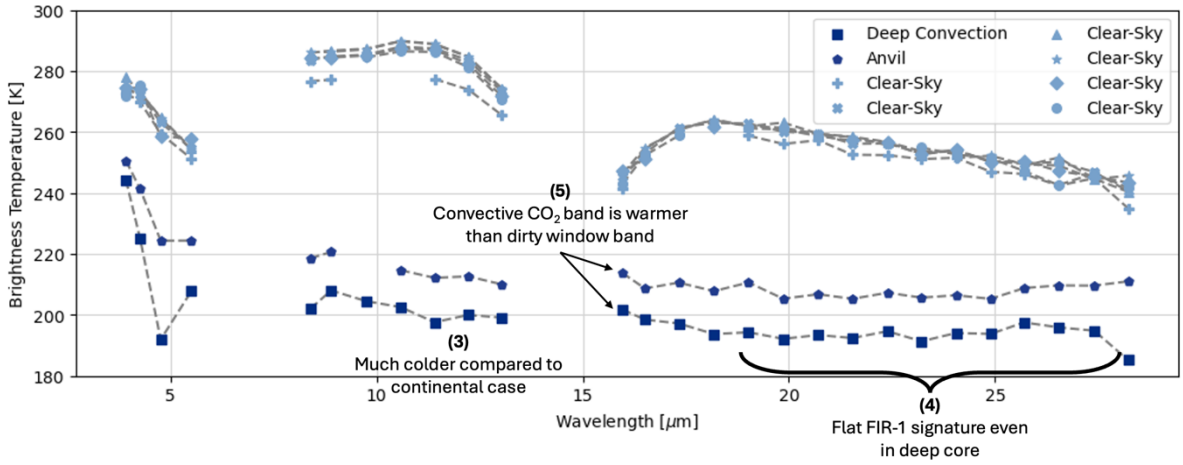

Figure 23: *Spectra from the indicated PREFIRE tracks in (left), showing clear-sky (light blue) and convective (dark blue) spectra. The convective spectra are further split into a deep convective observation (squares) and an anvil observation (stars). Points of interest for the convective spectra are marked (3), (4), and (5); see text for details.*

3. Convective clean window channel

In both the convective core and the anvil, the clean window channel measurements are colder than in the mid-latitudes – by about 20 K in both instances. The corresponding temperature profile, shown in **Figure 24**, indicates that the cold-point tropopause in this region may be found at 191 K; if we approximate this as the tropical tropopause, the spectra that show this warm CO_2/cold window relationship may be inferred to represent high clouds that reach or even penetrate the tropopause. Accounting for the previously characterized difference between PREFIRE recorded temperatures and GOES recorded temperatures, the PREFIRE window channel observation of ~200 K can be reasonably presumed to be a tropopause observation – useful context to have when considering the origins of spectral signatures in the FIR-1 band.

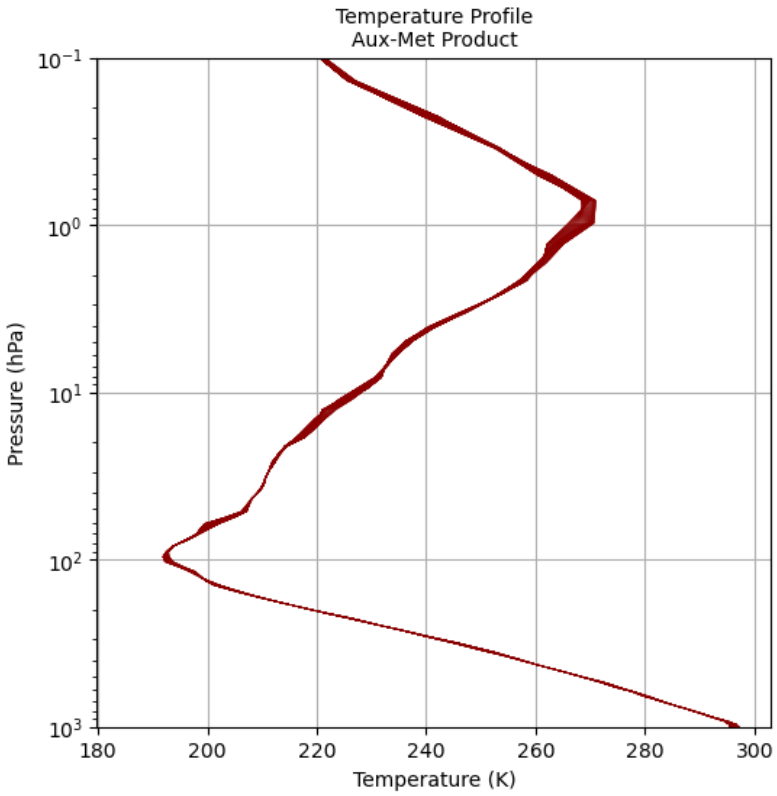

***Figure 24**: Aux-Met temperature profile for convective overpass in Brazil*

The dirty window band for these convective spectra remains largely in agreement (within ~5 K) with the clean window band, in alignment with the spectral behavior shown in the mid-latitude case.

4. Convective water vapor absorption band

In the convective anvil, the FIR-1 water absorption band is largely flat, with minimal variation in the 20-25 μm region of the FIR-1 filter and a slight increase in brightness temperatures as wavelengths grow longer than 25 μm. In the convective core, the FIR-1 water absorption has a very similar structure throughout much of the FIR-1 filter, but instead of a shallow increase at wavelengths longer than 25 μm, there is a momentary increase followed by a sharp decrease in brightness temperature between 27 μm and 28 μm. A number of environmental factors may result in this abrupt decrease; one of the most significant is the strong variability of the far-infrared water absorption. While absorption generally increases with increasing wavelength, as identified in the introduction and demonstrated by Turner and

Mlawer (2010), it varies strongly wavelength-to-wavelength and some channels may be more significantly absorptive than others. As previously discussed in Section 4.1.2., the injection of water vapor into the atmosphere as a result of convection may cause brightness temperatures to increase as longer-wavelength channels peak higher in the stratosphere and the signal of the stratospheric lapse rate emerges. A decrease like this may be an opposite result of the same effect: localized water injection causing the longer-wavelength channels to pick up a colder brightness temperature.

5. Convective dirty window band and CO_2 band

The convective transition from the CO_2 band into the dirty window band is characterized by a decrease in brightness temperature, as opposed to the increase (or stability) shown in the mid-latitude convective case. The difference between the mid-latitude and tropical cases may be a signature of injected water vapor into the upper troposphere or lower stratosphere in the tropical case, but the contrast with a clear-sky atmosphere, where the CO_2 absorption is a stronger signal than dirty window water vapor absorption, is similar in appearance to the contrast between clear-sky and convective spectra in the continental case.

4.2.2. Spectral progression across storm boundary

We take a progression of spectra representing a window-channel brightness temperature gradient across the edge of the storm, from clear-sky into the strongest part of the southern half of the storm, to investigate more closely any regional variation in the storm's spectral signature. This gradient spectra, shown in **Figure 25**, shows the same distinct pattern shown in Figure 8, but emphasizes the variation in CO_2 band absorption and the long-wavelength variations in brightness temperature. At very cold temperatures (window channel brightness temperatures of <220 K), a distinct sawtooth pattern emerges in the long wavelengths of the FIR-1 band. This sawtooth pattern is not present in shorter wavelengths closer to the dirty window band, which raises the possibility that this may be a spectral signature of particle

size, cloud characteristic, or some other microphysical property; we will investigate this possibility later.

In the CO_2 absorption band, there is an inflection point where the differences between absorption in the CO_2 band and the dirty window band switch from a negative displacement in warmer and clear-sky regions (window band is warmer than CO_2 band) to no displacement in mid-temperature, anvil settings (brightness temperatures are the same); this changes to a positive displacement in very cold regions near the pedestal (CO_2 band is warmer than the window band).

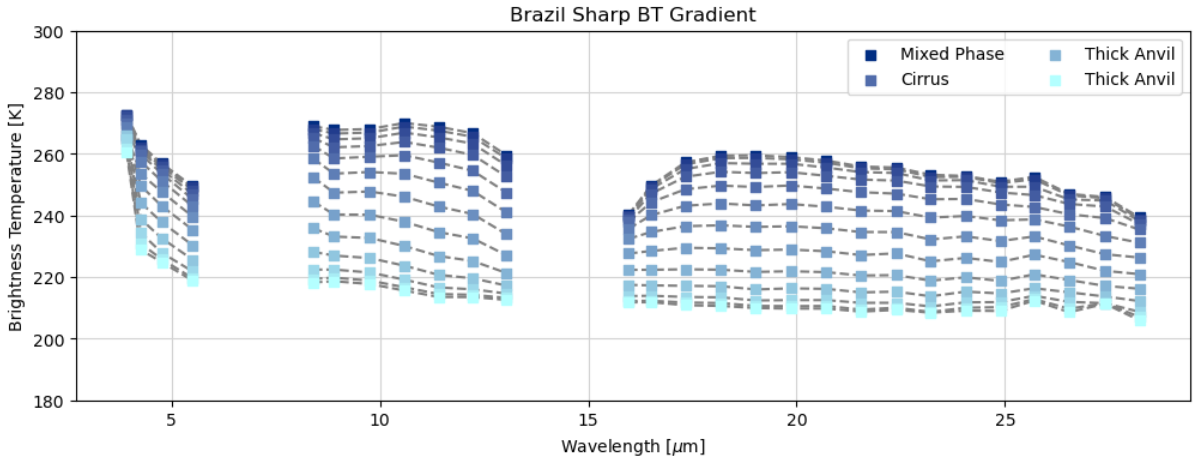

Figure 25: *As in Fig 21 and 23, for a progression of observations across a steep brightness temperature gradient in the storm.*

In this rainforest storm (compared to the previous instance of continental convection), the wavelengths at the long end of the FIR-1 filter do not present the increasing brightness temperature signal that was observed in the mid-latitude, more intense case. It may be possible to infer from these signatures information about both the height of the cloud and the thickness of the cloud. Figure 19 shows the optical depth and cloud particle size recorded at cloud-top by the GOES-16 night algorithm. The use of the night algorithm is a confounding

factor, as the night algorithm is IR only and therefore has a number of flaws due to its sole dependence on IR-based retrievals, but it provides useful context.

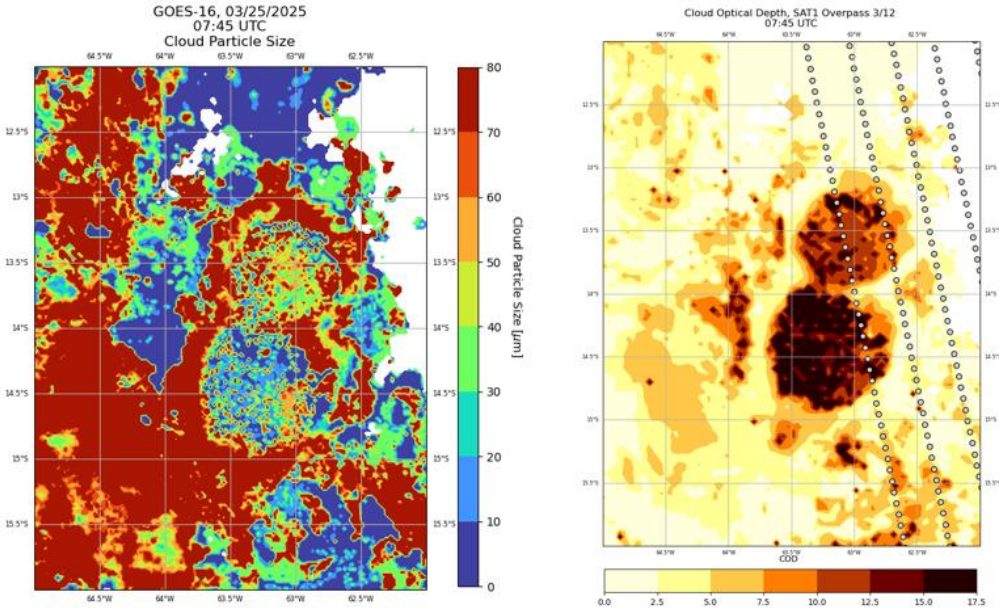

***Figure 26**: Left: GOES-16 cloud particle size product for the convective case. Right: GOES-16 cloud optical depth product for the same convective case. PREFIRE tracks overlaid as grey circles.*

Comparing the PREFIRE dirty window channel with the PREFIRE clean window channel has provided useful information about cloud-top height – as noted previously, the brightness temperature agreement between the clean and dirty window channels indicates that the cloud is tall enough that the water vapor absorption properties of the far-infrared region do not impact the brightness temperature recorded – but comparing the dirty window channel with the CO_2 absorption band may provide information about optical depth as well as some height information. By comparing Figures 25 and 26, we can see that in optically thicker clouds, the CO_2 absorption band is measured at a warmer BT than the FIR-1 dirty window; as we move further into the FIR-1 and wavelengths get longer, the BTs flatten out (with occasional "sawtooth"-like fluctuations) before increasing again towards the edge of the FIR-1 band. In

these very cold and thick regions, the true window temperature is also measured as warmer than the dirty window band.

A tentative explanation for this CO_2 band signature, which was not observed in the mid-latitude case, is that a stratospheric signature may be present. As previously identified, these observations are in close proximity to the tropopause. While in the mid-latitudes the tropopause extends for some distance (as evidenced by the Aux-Met profile for the mid-latitude case), in the tropics this is a much more abrupt transition (as shown in **Figure 24**). While the approximate minimum temperature for a cloud is at the cold-point tropopause, overshooting tops in particularly deep convection may break through the tropopause and present with warmer brightness temperature past the tropopause (Xian and Fu 2015). In the case where deep convection makes it to the tropopause, the mid-infrared window band brightness temperature will be a near-perfect representation of the cloud-top temperature, the dirty window band will, per our prior characterization, reflect this near-perfect representation, and the CO_2 band will reflect warming in the stratosphere as the weighting function for this band will peak higher in the atmosphere. In the window channel, once a cloud breaks through the tropopause, we may begin to see warming as the stratosphere warms. As we progress through the far-infrared dirty window to the edge of the FIR-1 filter, potential water vapor signatures in the stratosphere – ambient water vapor in the stratosphere or water vapor injected into the stratosphere from overshooting tops – will become more and more prevalent in the spectrum, resulting in a warming brightness temperature and the convex arc shown in those very cold spectra. The corresponding weighting function peak higher and higher in the

stratosphere and the warming signal becomes stronger, resulting in a warmer brightness temperature and the convex arc shown in the coldest spectra.

4.3. What spectral signature do we observe from extremely deep convection?

Having characterized a relatively typical case of continental convection and of rainforest convection, we will now seek out an edge case: how do these spectra change when we observe some of the deepest convection in the world?

On April 10, 2025 at 13:30 UTC (15:30 local), SAT1 observed a very deep convective storm over the northwestern region of the Democratic Republic of the Congo, shown highlighted against METEOSAT-10 observations in **Figure 27**.

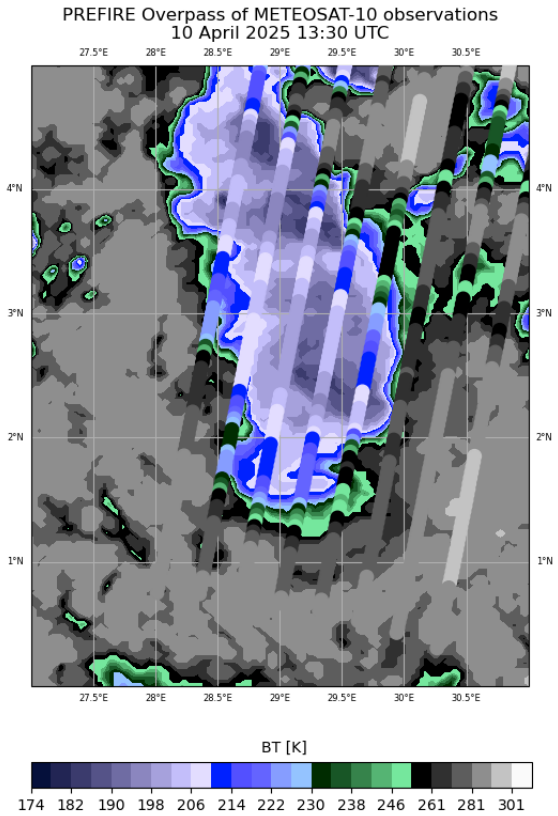

Figure 27: *METEOSAT-10 window channel brightness temperature observations of a deep convective storm over the DRC, with PREFIRE tracks overlaid. Both PREFIRE and METEOSAT-10 use the same colormap.*

This is a case of afternoon deep African convection, with window channel brightness temperatures recorded by PREFIRE dipping as low as 195 K (down to 180 K as recorded by METEOSAT-10). The modelled cold-point tropopause for this case, which will be useful in assessing whether or not clouds reach the stratosphere, is 189 K (shown in **Figure 28**

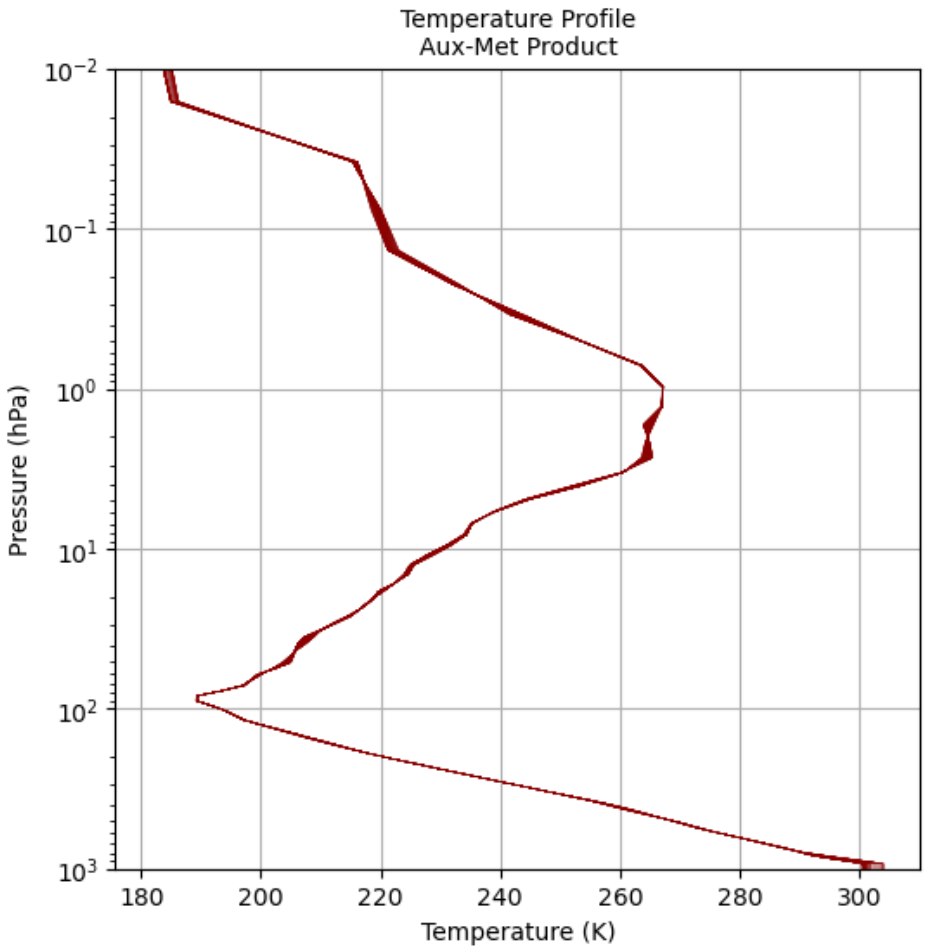

***Figure 28**: Aux-Met temperature profile for the Congo case.*

We highlight in **Figure 30**Figure **31**, and**Figure 32** three separate scenes from the PREFIRE overpass of this system: Scene 4, Scene 6, and Scene 8. This particular overpass was a descending overpass, so the leftmost track corresponds to Scene 8 while the rightmost track corresponds to Scene 1. These spectra plot every PREFIRE observation of each scene's overpass of the storm (demarcated in this case as all geostationary window channel

brightness temperatures below 250 K, breakdown shown in **Figure 29**). Our analysis will focus on the spectral shapes observed across different brightness temperature thresholds.

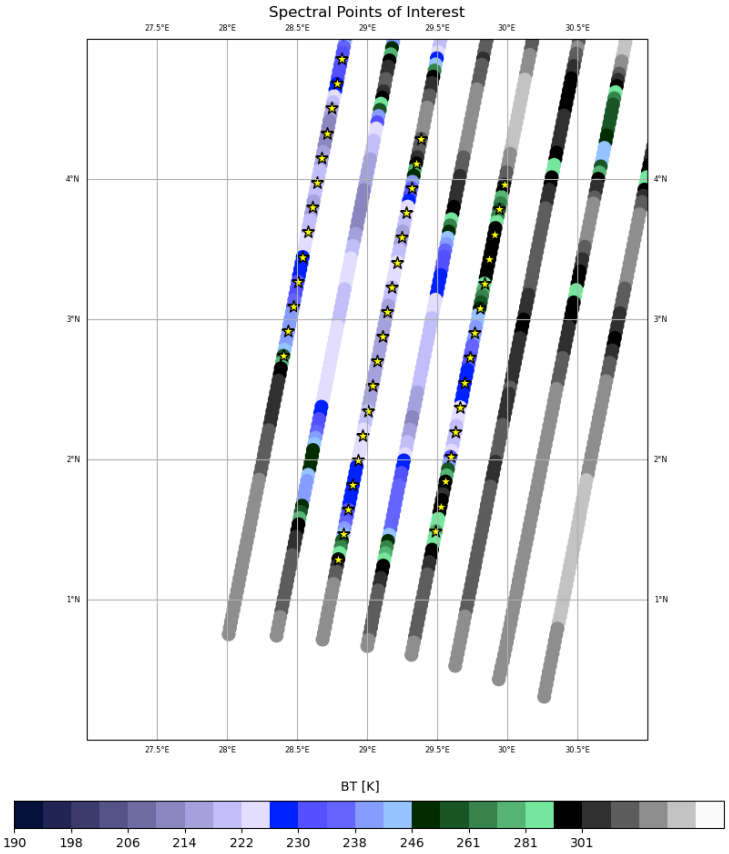

Figure 29: *PREFIRE overpass of case with stars showing the locations of spectra shown in Figs 29-31.*

:

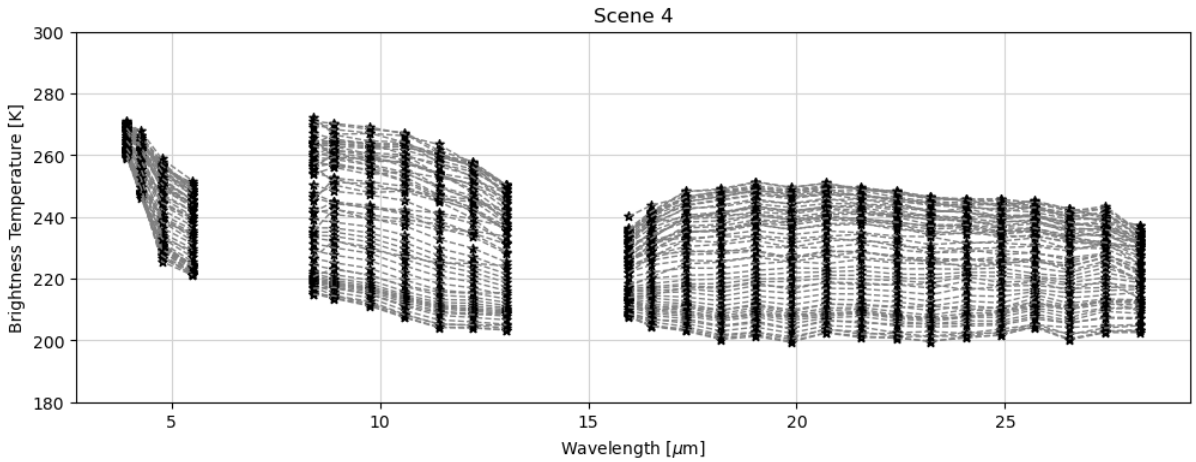

Figure 30 *Spectra from Scene 4 of PREFIRE observations of the deep convective storm shown in Fig 21. Observations are taken from the portions of the scenes that pass over the regions of the storm where geostationary window channel observations were colder than 250 K.*

The first scene we will highlight, in **Figure 30**, is Scene 4. Scene 4 passed over the outer edge of the southern portion of the storm, with a glancing pass over the coldest temperatures in that region – a region of convection, but not the coldest brightness temperatures PREFIRE observes in this storm. As such, this bears significant resemblance to the continental and rainforest deep convection we have already analyzed: a notable increase in measured brightness temperature from the CO_2 band progressing into the far-infrared dirty window, a clear thin cloud/clear sky signature in the warmer regions, and a relatively flat signature in the colder regions, with relatively strong agreement between the far-infrared dirty window, the end of the FIR-1 filter, and the MIR-2 window. This agreement highlights what we have discussed already: stratospheric-height cloud tops, such as those observed in this deep convection, have strong agreement across the longer ends of the IR spectrum because there is minimal tropospheric water vapor interference in the far-infrared signal.

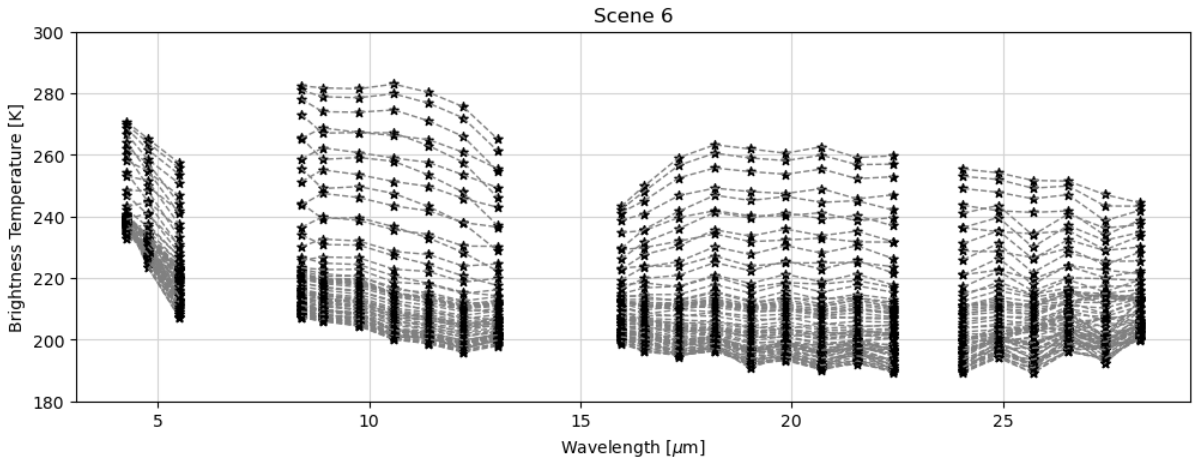

Figure 31: *As in* ***Figure 30****, but for Scene 6.*

Scene 6, shown in **Figure 31,** differs from Scene 4 primarily in the colder regions; while Scene 4 remains relatively flat throughout the FIR-1, Scene 6 displays the jagged sawtooth-like pattern previously noted in other examples of convection. This jagged pattern is strongest across the full FIR-1 band in the warmest and coldest measurements in Scene 6, while in mid-range window channel BT measurements the flat pattern displayed in Scene 4 is still

present in the shorter wavelengths in FIR-1. At the longer wavelengths in FIR-1, a slight sawtooth pattern arises in these mid-range window channel measurements as well. While it is possible that this is merely an instrument noise signal, it occurs consistently throughout other PREFIRE overpasses of convection and has not occurred solely in Scene 6. The possibility exists that this may not be an instrument noise signal and may instead contain some physical meaning.

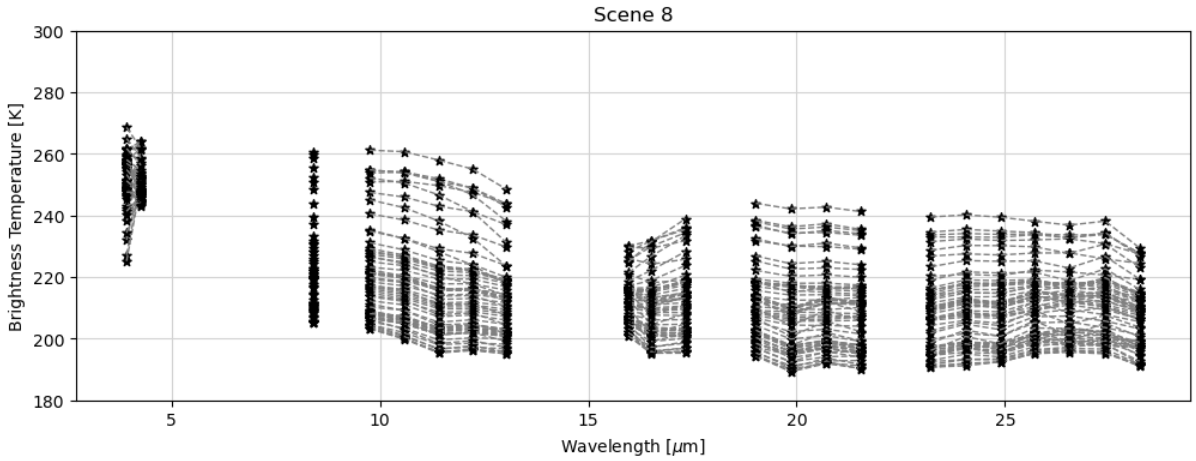

Figure 32: *As in Figures 29 and 30, but for Scene 8.*

Scene 8, shown in **Figure 32**, is the most interesting scene in this framework. Using the understanding we have previously developed of convective spectral signatures, much of the spectra presented in scenes 4 and 6 is familiar and easily interpretable. In Scene 8, however, we measure the very coldest clouds: those that reach the tropopause and possibly beyond. This is where we see PREFIRE-measured temperatures dropping to 196 K; as the tropopause in this region is at 189 K, it is

Accommodating for known discrepancies between PREFIRE brightness temperatures and geostationary brightness temperatures, as described in Chapter 3, the measurements taken at the very coldest regions of this storm (PREFIRE measurements of 193 K) can be assumed to be observations of clouds at the tropopause. Correspondingly, in Scene 8 we see spectral signatures that have not appeared in the previous two cases. At 25 μm, we start to see an

increase in the coldest measurements; as we progress further towards the edge of FIR-1, temperatures steadily increase until we reach the very edge of FIR-1, at 28 μm, where they begin to decrease again. This pattern is not observed in any other storm that we have previously analyzed, but it does occurs in two separate scenes in this storm – Scene 8 (shown in **Figure 32**) and Scene 7 (not shown). Scenes 8 and 7 pass over the same region of the storm and both observed very cold convection as shown by METEOSAT-10; Scene 8 was chosen for analysis solely because more channels are "good" quality data than in Scene 7. We can conclude from this inter-scene corroboration that this is likely a physical signal, theoretically consistent with far-infrared channels above overshooting tops sampling progressively higher in the stratosphere where temperatures increase with height; potentially, this is a stratospheric signal.

4.4. Can we distinguish a difference between oceanic and land-based far-infrared spectral signatures?

We have developed baseline spectra for land-based mid-latitude and tropical convection as well as an extreme of tropical convection; we turn our attention now to oceanic convection. Primarily, we will attempt to discern if there is a notable qualitative difference between a particular case of oceanic convection when compared with our land-based analyses.

Before performing this analysis, it may be useful to identify the key differences between oceanic convection and continental convection, in order to best characterize what we might expect to differ in the emission spectra for each storm type – and to begin to investigate whether this might be identified in these kinds of measurements.

Broadly speaking, continental convection (which we have categorized the preceding three cases as) will produce more short-lived storms with larger convective cores (Liu and Zipser 2013, Takahashi et al. 2021) that reach a larger maximum height and generally have stronger

updraft speeds. These stronger updraft speeds are generally (but not always) correlated with larger particle sizes at the convective cloud-top, though not necessarily at the top of the convective core. Radar reflectivity, shown in **Figure 33**, generally peaks for continental convection at higher altitudes than oceanic convection (Ge et al. 2024). Over the lifecycle of these convective storms, oceanic radar reflectivity varies less than continental radar reflectivity.

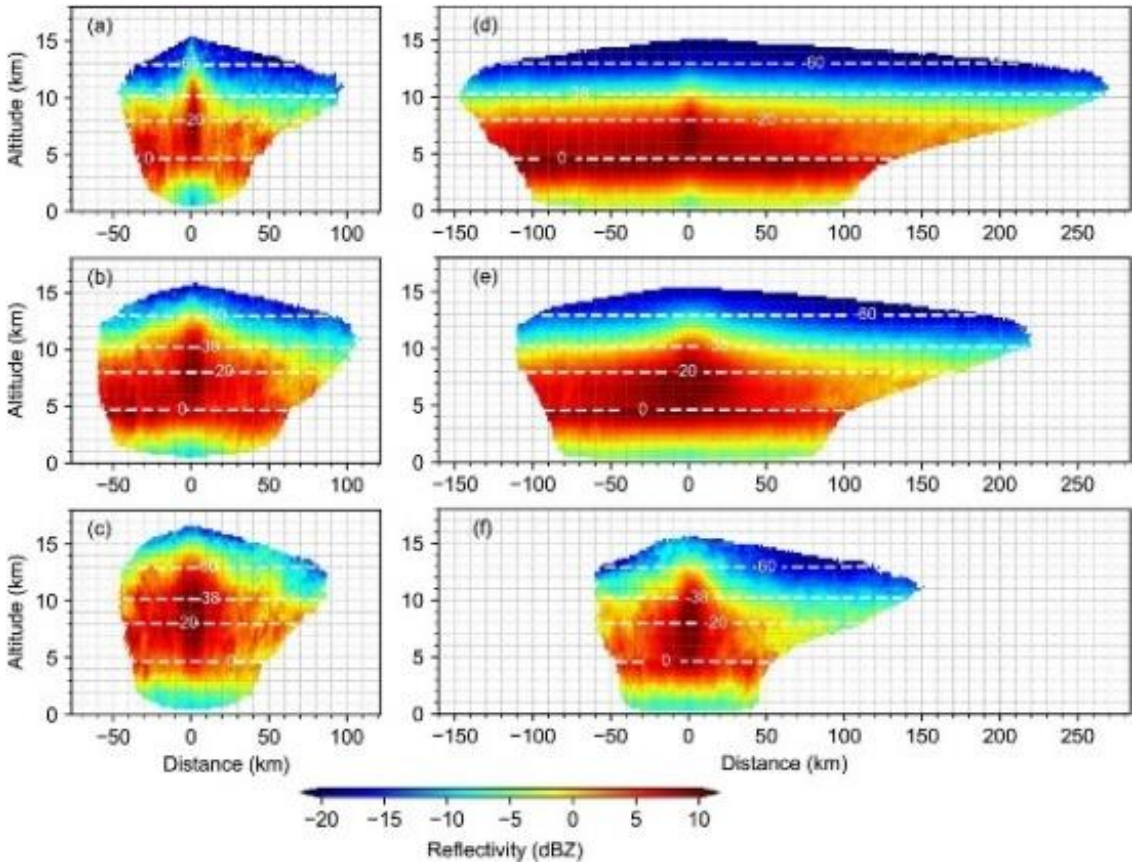

Figure 33: *Ge et al. 2024: Median CloudSat reflectivity of the DCS at developing stages (top panel), mature stages (middle panel), and dissipating stages (bottom panel) over land (left column) and ocean (right column). The white dashed line indicates isotherm with the unit of deg C.*

Ge et al. 2024 also find that if we define storms as being composed of a larger major anvil, a smaller minor anvil, and a convective *pillar* (which encompasses a convective core, or more than one convective core, and the most intense regions of intervening stratiform precipitation), oceanic convection has on average larger convective pillars; in the case of oceanic and continental convection with similarly sized convective pillars, the associated

anvils were significantly more extensive for oceanic than continental convection. In general, oceanic storms were more extensive and longer-lasting, but were less intense.

Particle sizes over the storm lifecycle also vary in altitude and lifecycle dependency based on whether it is oceanic continental; these variations are shown in **Figure 34**. In the context of spectral observations, we might expect that, in oceanic convection, identifiable particle size signatures would indicate generally smaller particles; that the relationship between the far-infrared dirty window and the mid-infrared clean window may be less pronounced, as these convective regions do not reach as far into the upper troposphere; and that as the PREFIRE dataset grows, it may contain more cases of oceanic convection, as these storms are more spatially extensive.

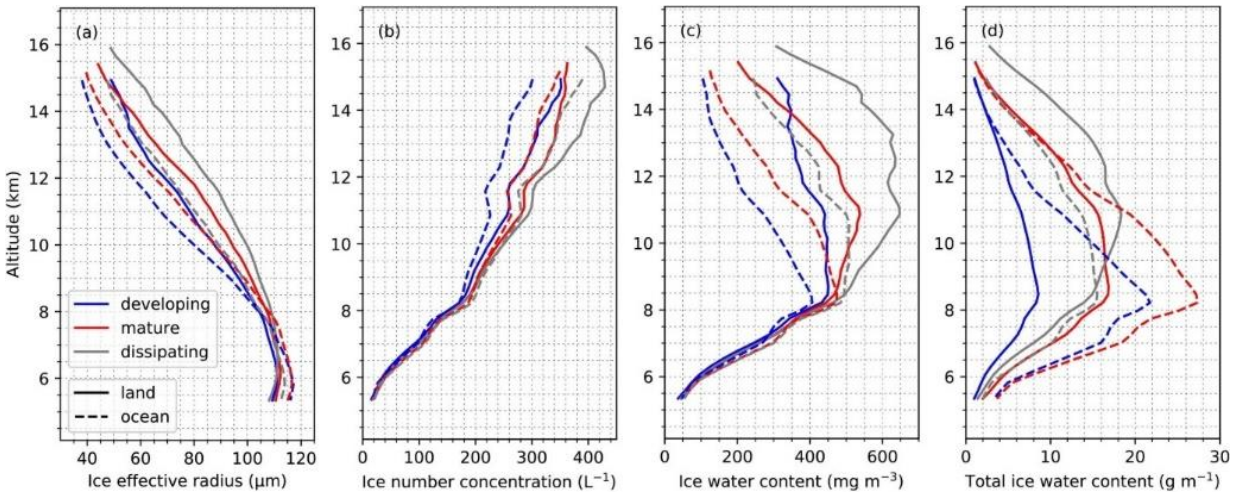

Figure 34: *from Ge et al 2024: Vertical profiles of median (a) ice effective radius, (b) ice number concentration, (c) ice water content and (d) total ice water content of convective pillar. The blue, red, and gray lines indicate developing, mature, and dissipating stages, solid and dashed lines indicate DCSs over land and ocean.*

The bulk of our expectations come from the differences between oceanic and convective lifecycle characteristics. In Chapter 7, we will begin to develop the tools to investigate lifecycle implications further. For now, we will take as an initial oceanic case study a moderately intense storm that took place in the local late evening on January 23, 2025 over the Indian Ocean, just off the western coast of India. The PREFIRE overpass is shown in **Figure 35**.

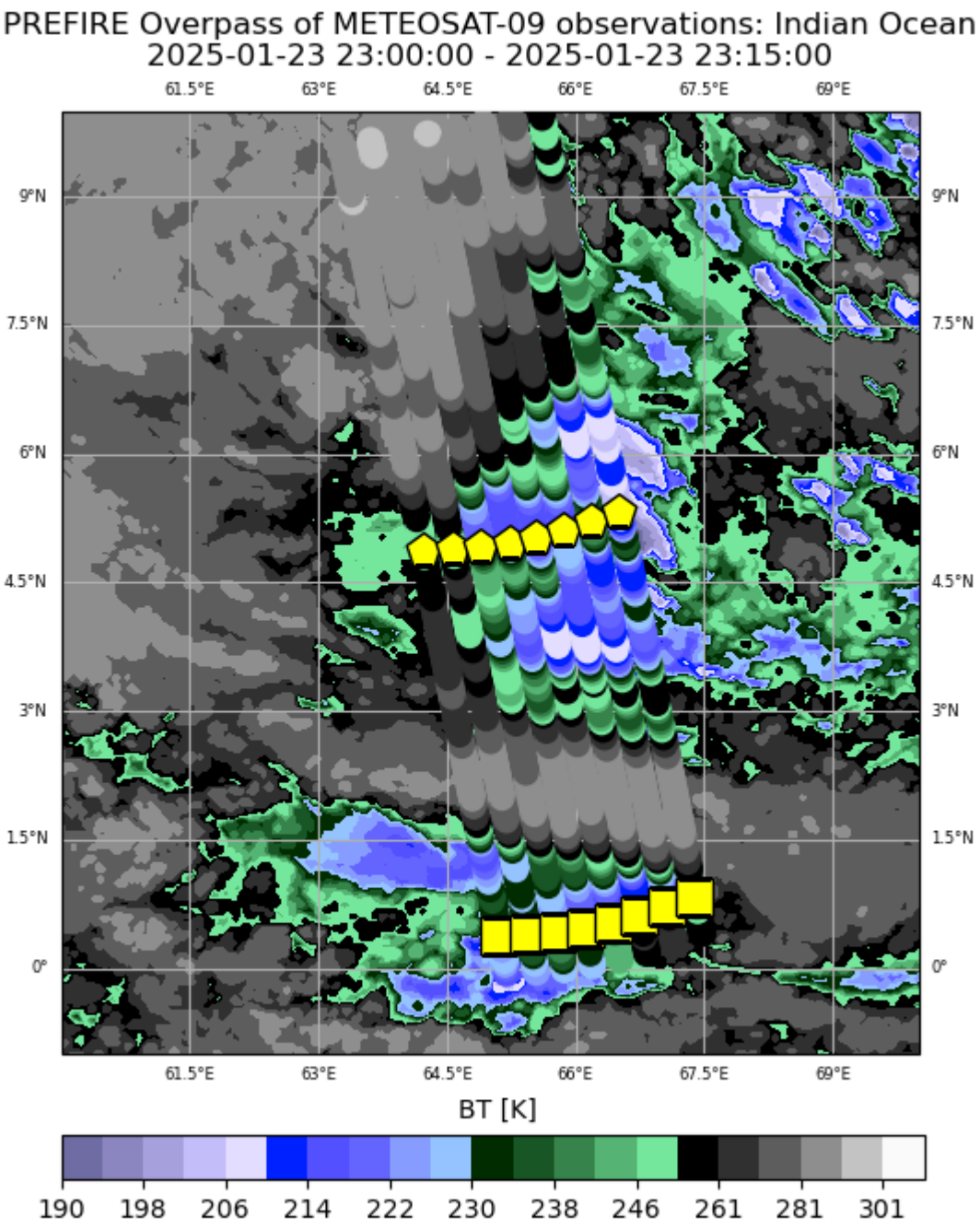

Figure 35: *Indian Ocean overpass, with location of spectral observations noted in yellow.*

This case of convection is surrounded by multiple additional storm complexes, making a particular lifecycle stage difficult to identify. Based on the minimum brightness temperature attained and the geostationary observations surrounding the PREFIRE overpass, we will approximate this observation as being of a relatively mature case of oceanic convection.

The scenes displayed here are from a PREFIRE ascending overpass; Scene 1 is the westernmost scene, while Scene 8 is the easternmost scene. A much larger portion of this storm consists of clouds between 230 and 250 K than in previously observed rainforest and continental convection, despite the fact that this is a storm approximately at maturity. This follows from prior observations showing that oceanic storms are generally more widespread, with more stratiform anvil and (presumably) precipitation (Ge et al. 2024), though it may also be influenced by local lapse rates. Due to water vapor, the lapse rate is lower, so clouds at different heights have more similar brightness temperatures.These more widepsread, warmer anvil clouds should also result in a difference in the radiative effect of this storm system, though it is unlikely that the discrete observations PREFIRE is capable of taking will resolve this with a single storm system.

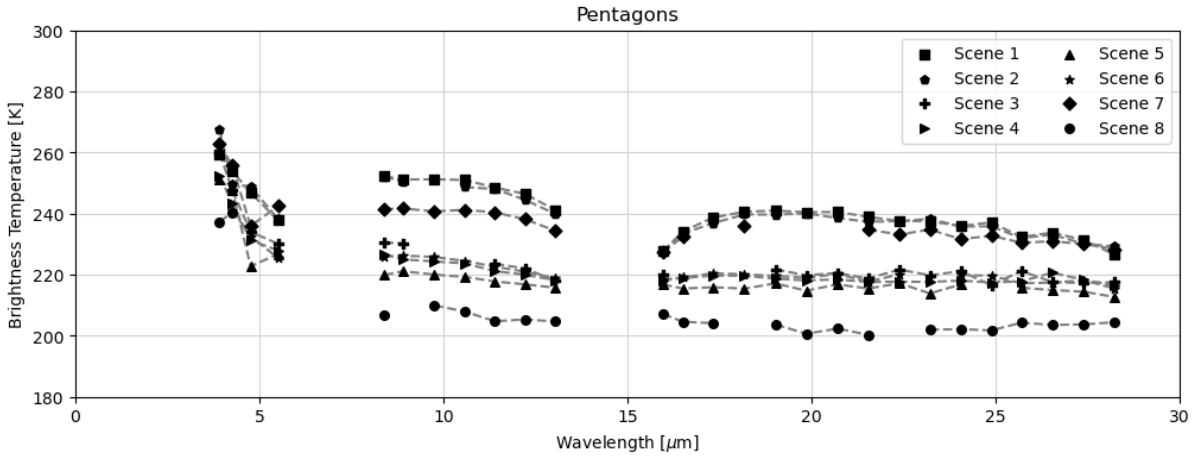

Figure 36: *Spectra taken from the region denoted by pentagons in* ***Figure 35***

Figure 36, which shows the spectra taken from the northern region denoted by pentagons in **Figure 35**, shows three distinct spectral signatures: the flat, very slightly U-shaped FIR-1 pattern of the very cold convective pillar region; the warmer, truly flat FIR-1 pattern of the cloud shield region; and the high arches of the FIR-1 clear-sky/less cloudy, warmer regions. This arc in the lower scene is in contrast to the more southern spectra shown in **Figure 37**, where, most notably, Scene 7 and Scene 2 are largely flat, lacking that clear arch out of the carbon dioxide band. This distinction arises despite their clean window channel brightness

temperatures being approximately similar to those in Scene 7 in the northern scene, where a very clear arch of the carbon dioxide band is shown.

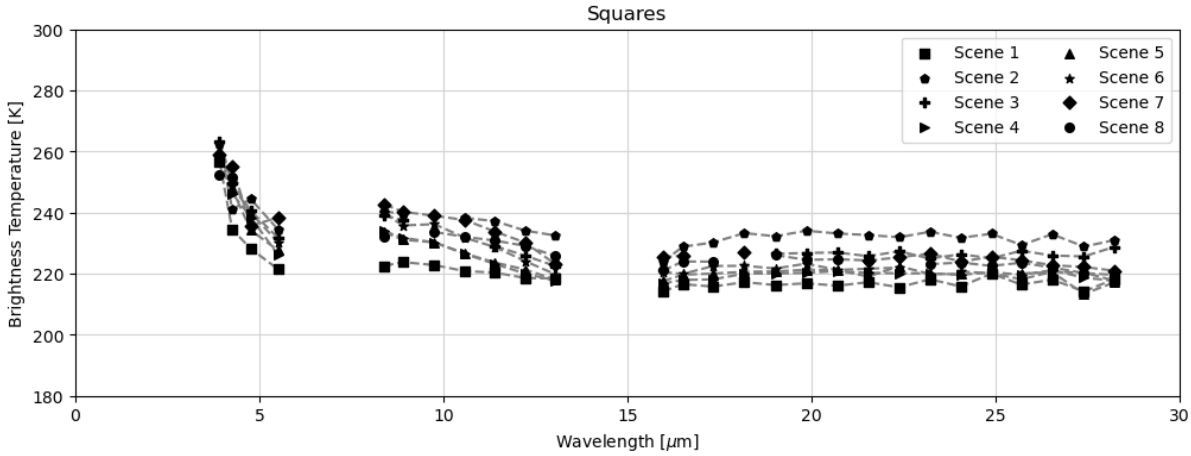

Figure 37: *Indian Ocean overpass, taken from southernmost convective region (region shown by squares in* ***Figure 35)***

It is notable that in the more "clear-sky" scenes there is a distinct exit of the carbon dioxide band, as observed in previous case studies, and that it behaves spectrally similarly to the Brazil case: a notable increase in brightness temperature as we approach the dirty window, but a still-noticeable disconnect between the clean window brightness temperatures. The arc into the dirty window is still not as steep as our previously analyzed non-rainforest continental case. The larger "shield" and warmer regions of the clouds also display some similarity to previous cases of continental convection, where these colder (but not coldest) regions are largely flat throughout the FIR-1. The relationship between the temperature of the far-infrared window and the clean longwave window is stronger in this area, with the far-infrared window warmer in Scene 8 of the southernmost scene.

Some of the slight disconnect between rainforest, continental, and oceanic spectra may potentially be attributed to differences in the water vapor content of the region itself. **Figure 38** shows the tropospheric water vapor and temperature profiles of this case from both the southernmost cloudy region and the northern cloudy region, while **Figure 39** shows a

comparison of the water vapor profiles for this case, the case of Brazilian rainforest convection, and the case of Congolese rainforest convection. We also show in **Figure 40** the total column water vapor across all observed scenes as it varies latitudinally.

In **Figure 38**, it is shown that the southern scene (squares) display some difference in water vapor content from the generally more saturated northern scenes; while this variation occurs largely at higher pressure than the brightness temperature in our PREFIRE observations, we can also observe in **Figure 40** that the total column water vapor at each observation point (Scenes 2 and 7 at the southern scene, versus Scene 7 at the northern scene) does display some variation.

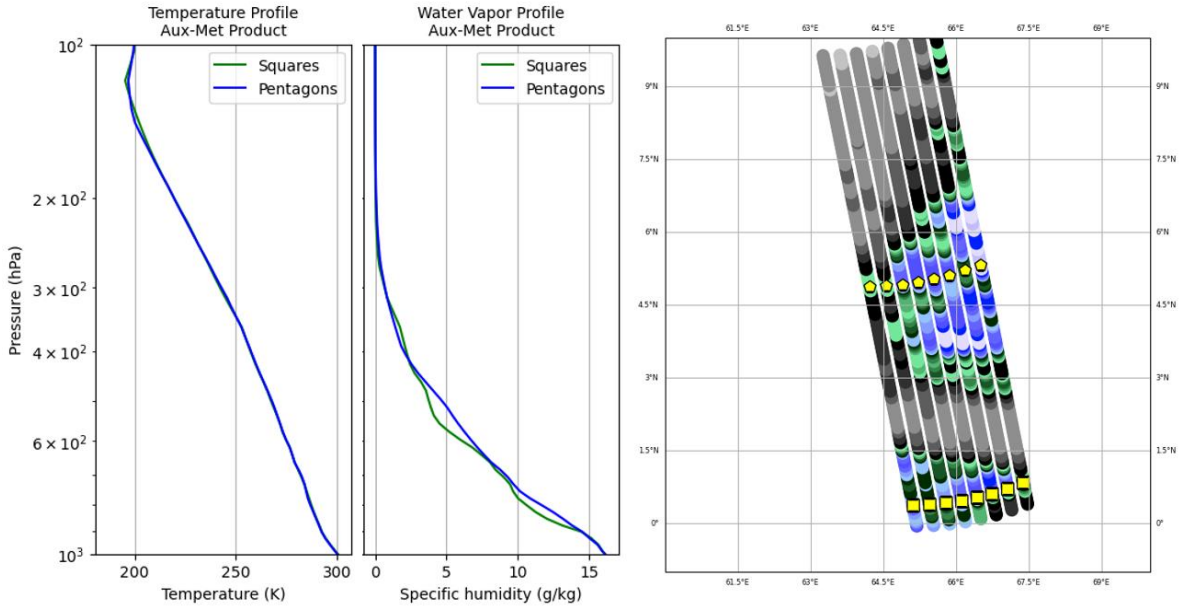

Figure 38: *Left, tropospheric temperature profile. Middle, tropospheric water vapor profile. Right, PREFIRE isolated tracks from this case, with stars indicating where each profile was taken from.*

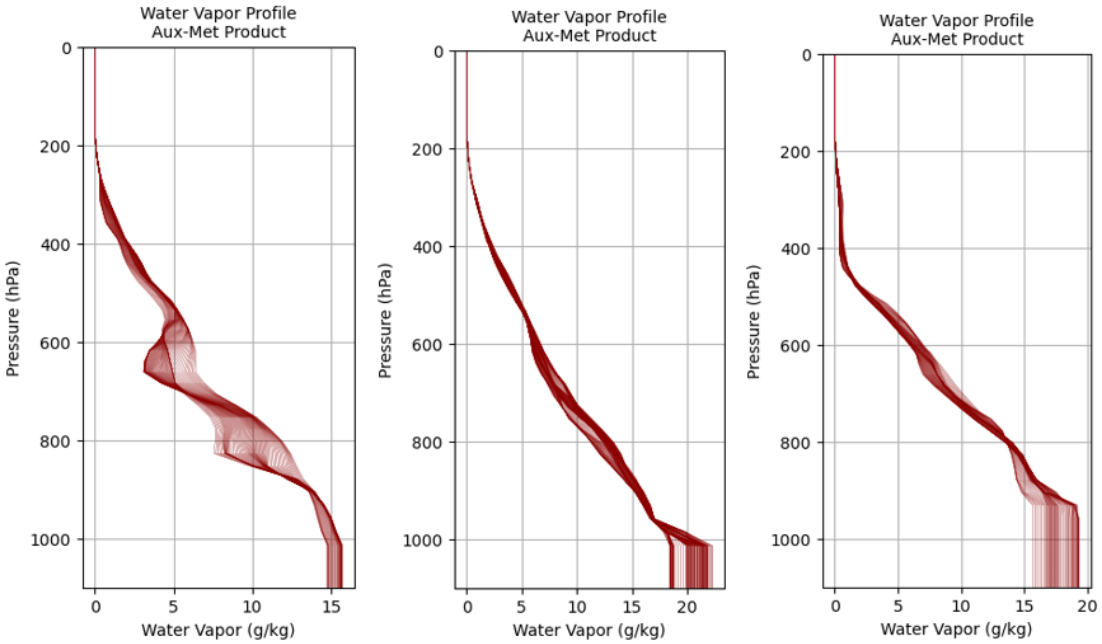

Figure 39 *Full water vapor profiles for (left) Indian Ocean, (middle) Brazil, and (right) Congo cases.*

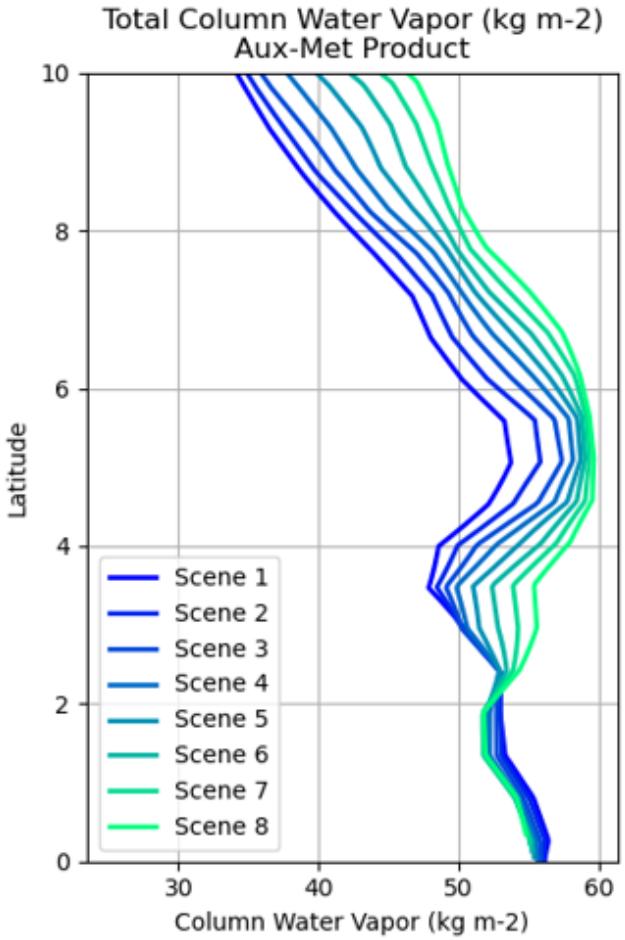

Figure 40: *Latitudinal variation in model-derived total column water vapor across all scenes*

In general, while some variation is present between continental and oceanic spectra, it is presently difficult to discern effectively and the impetus behind it is sitll unknown. More analysis of oceanic spectra is needed to determine if there is systematic dissent between oceanic and continental spectra; in future analyses, we hope to incorporate better vertical radar in order to form a more effective picture of atmospheric composition that may be impacting these spectra. Future work will attempt to more quantitatively identify this potential regional variation and to more effectively tie any spectral variation to its source.

4.5. Overall schematic

Based on the case studies analyzed here, we develop a preliminary and qualitative schematic outlining some common FIR-1 brightness temperature spectral features in convective clouds. **Figure 41** details the general patterns of spectral features that we have observed in the preceding sections.

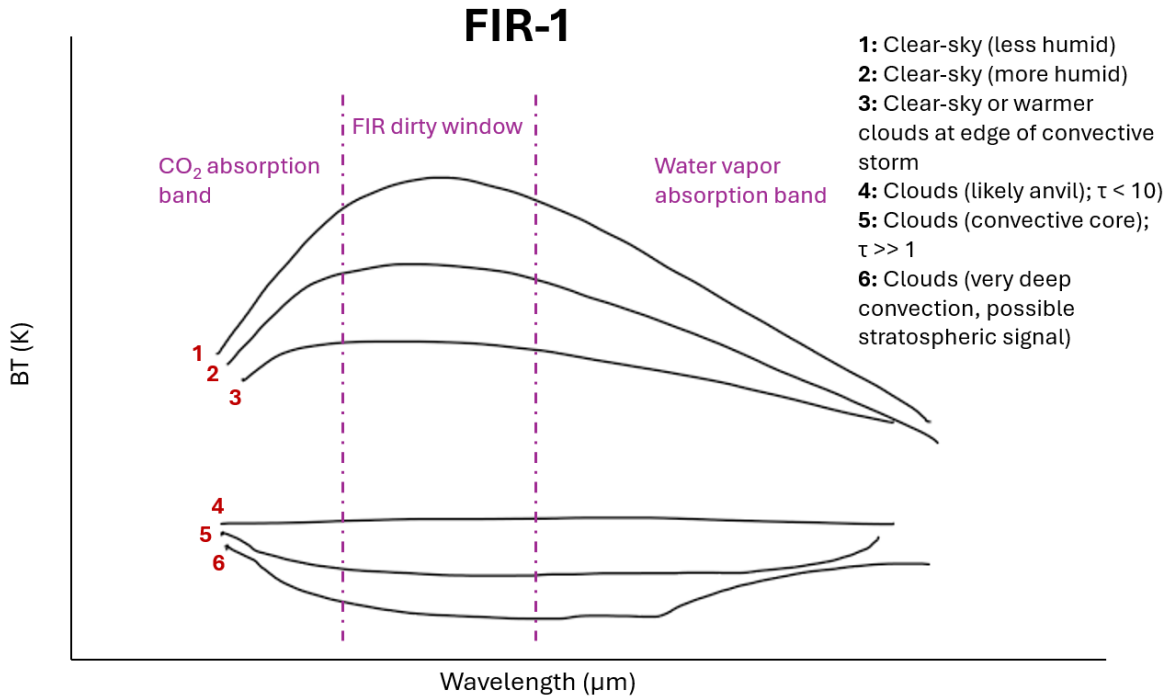

Figure 41 *Summary of spectral regimes observed in cases 1-4*

With the exception of the very coldest brightness temperature measurements, where our case studies have not gone into significant detail and much more work is needed in order to

diagnose spectral signatures, this figure represents a graphical summary of much of what has been discussed in the preceding section. We will build off of the characteristics shown in this figure to attempt to diagnose particle size, develop a split-window technique, and begin to differentiate between different types of convection – both regionally and, perhaps, across lifecycle stages.

Chapter 5. Possible far-infrared enhancements of modern retrieval techniques

5.1. Possible far-infrared particle-size signatures

We will begin by proposing a framework to infer the presence of particle size signatures in the far-infrared. We have discussed previously the general radiative effects of particle size and habit in the far-infrared, but here we will narrow our scope down to individual particle effects.

Particle-wave interactions in the longer wavelengths of the far-infrared are largely dominated by the Mie scattering regime, as opposed to the Rayleigh scattering that dominates at shorter wavelengths (Petty 2006). As we move further into the Mie regime, the influence of crystal habit and particle size on scattering properties is more significant than it is smaller wavelengths (Yang et al 2013). Scattering albedo and extinction efficiency are in particular sensitive to particle size; this sensitivity may be displayed even at coarser spectral resolutions in the far-infrared. Where the particle size is on the order of the incident wavelength, the habit has notable influence, as shown in **Figure 42** for droxtal, column, and plate crystals.

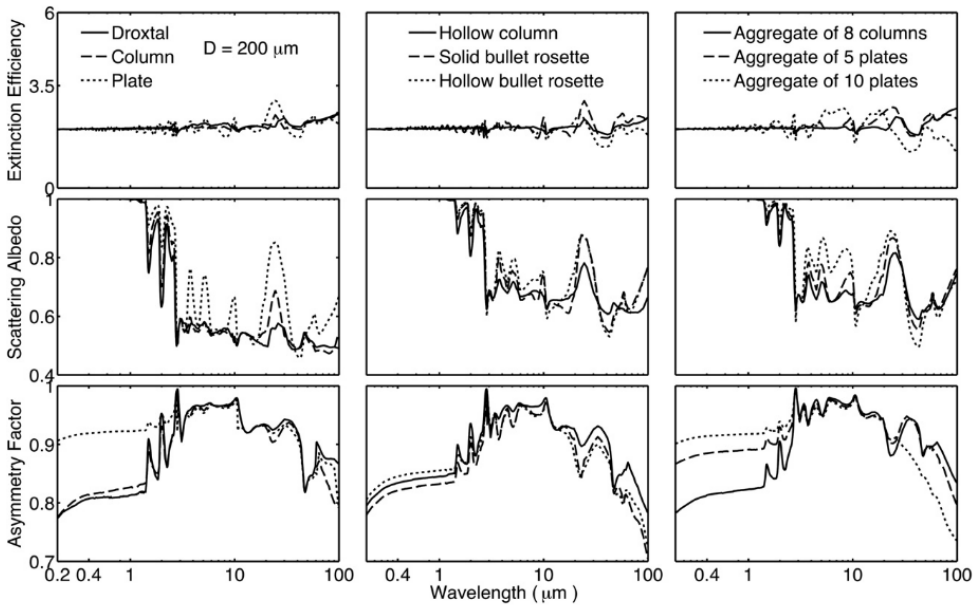

Figure 42: *Yang et al (2013) showing the variation of extinction efficiency, scattering albedo, and asymmetry factor over wavelength values 0-100 for a particle with maximum dimension 200 μm*

The impact of wavenumber (length) on extinction efficiency, absorption efficiency, and asymmetry factor is shown in **Figure 43** and**Figure 44**: **Figure 43** shows the variation, based on wavenumber, of scattering effects for four different particle sizes, while **Figure 44** shows the variation, based on particle size, of scattering effects for four different wavelengths. **Figure 43** in particular highlights the degree to which this variability may be confined to the far-infrared. While wavenumbers greater than 700 cm^{-1} are not shown, we see particularly than mean extinction efficiency begins to converge upon a singular value for all shown particle sizes as wavenumber increases and wavelength decreases.

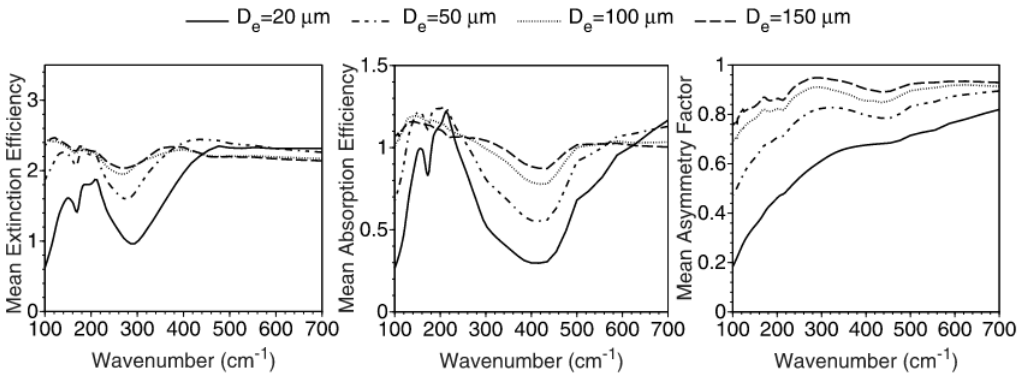

Figure 43*: The variation of mean extinction efficiency, mean absorption efficiency, and mean asymmetry factor as a function of wave number for four particle sizes (Yang et al 2013)*

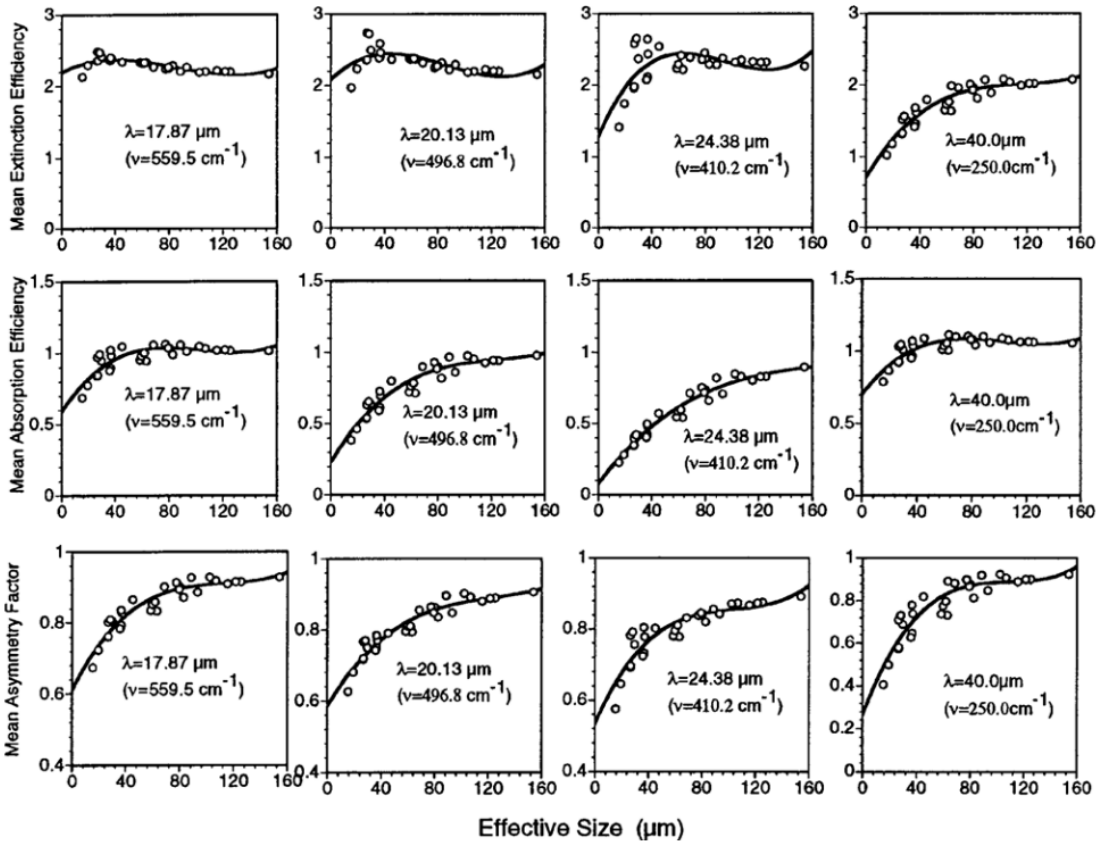

Figure 44: *The mean extinction efficiency, absorption efficiency, and asymmetry factor calculated for the 30 size distributions (circle). The solid lines are curve fits in terms of a third-order polynomial function of effective particle size (Yang et al 2013).*

These figures show us that as we progress through the far-infrared, we may see channel-specific variations in brightness temperature. These variations may be used to retrieve information about particle size or shape. At a given particle size and shape, individual incident wavelengths may have distinct absorption efficiency variations that appear in the otherwise generally consistent far-infrared spectra. We can expect this type of abnormality to be more obvious the further into the far-infrared we get, where extinction properties show more variation with wavelength.

To investigate this possibility, we identify a case of isolated continental convection. The case chosen for this analysis, a SAT1 overpass of a continental convective case on the US/Canada border across Ontario, Quebec, New York, and Vermont, was chosen for its ease of isolation and quality of data; this case occurred without any surrounding convection and is comprosed

entirely of quality flag-0 data. This case, shown at the time of the PREFIRE overpass in **Figure 45**(a), took place in the afternoon hours of June 24, 2025 between 1900 UTC on the 24th and 0200 UTC on the 25th, meaning that daylight imagery (**Figure 45**(b)) is available, improving the particle size and optical depth information available in geostationary validation products. There was no other significant convection nearby and the case had easily identifiable storm edges throughout its lifecycle, simplifying PREFIRE data selection and allowing for confidence that all data analyzed was affiliated with the case in question. This case was an descending PREFIRE overpass, so Scene 1 is the easternmost scene and Scene 8 is the westernmost scene.

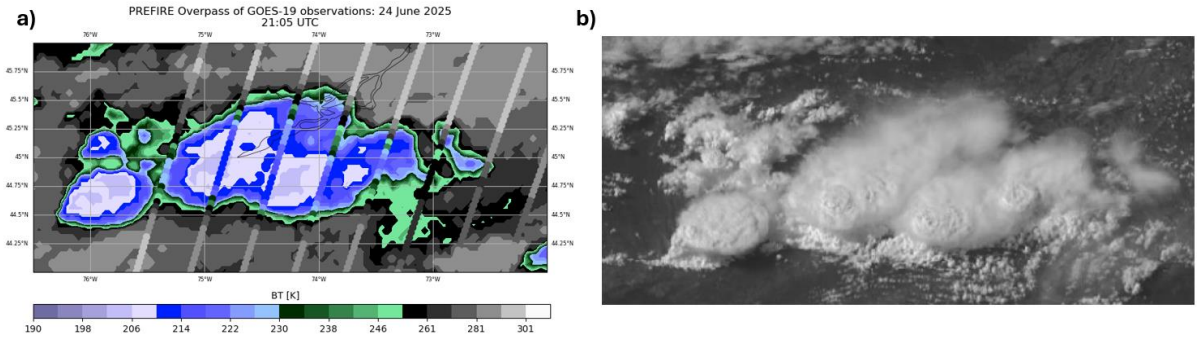

Figure 45: *Left, GOES-19 brightness temperatures observations of a convective storm occurring over New York/Ontario/Quebec/Vermont with PREFIRE tracks overlaid. Right, visible imagery of the same storm (courtesy NASA-Worldview).*

Two sets of spectra from this overpass are shown below with accompanying particle size context from GOES-19: one set that may show smaller particle size signatures (**Figure 46**a and b), and one that may show larger particle size signatures (**Figure 47**a and b).

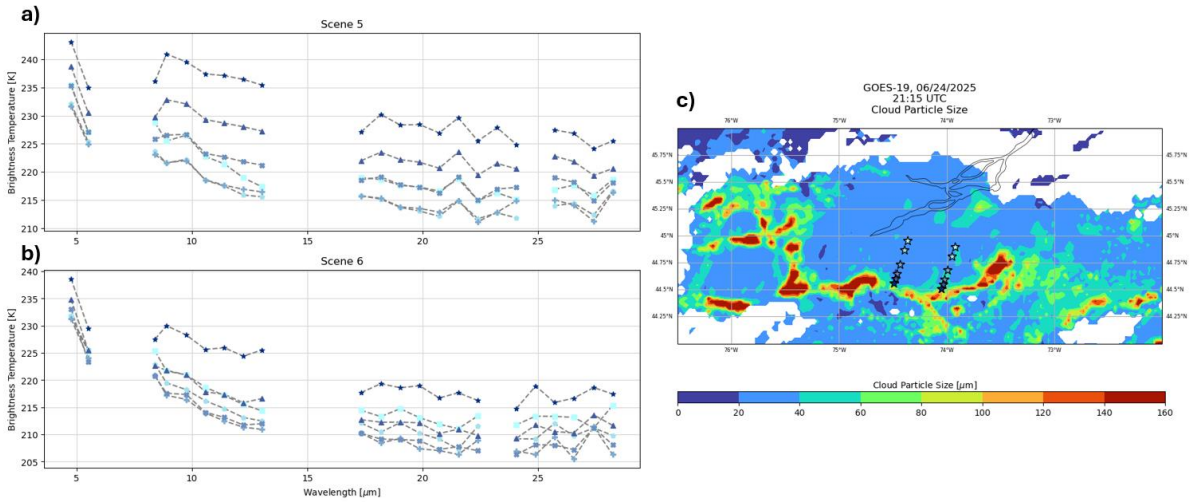

Figure 46: *Two possible smaller particle size spectral signatures: a) Observations from Scene 5, the easternmost scene b) Observations from Scene 6, the westernmost scene c) the GOES-19 Cloud Particle Size product, with the locations of the spectral measurements overlaid as blue stars.*

Figure 46(c) shows that the selected spectra from Scenes 5 and 6 are from regions with particle sizes between 20 and 40 μm, with a steep particle size gradient in the southern ends of the observations. The selected spectra are correspondingly jagged, with some perturbations that may represent spectral signatures of those smaller particles. This spectral signature also occurs in the case of deep African convection (Congo, Chapter 4.3) and mid-latitude convection (Chapter 4.1).

At, for example, 24.38 μm, the extinction efficiency for particles in this size range varies strongly with size while also exhibiting a strong dependence on incident wavelength. **Figure 43**, from Yang et al. 2013, shows a significant negative slope as wavelength (wavenumber) increases (decreases) in this range. It is possible that this negative slope, coupled with overall significant variability in extinction efficiency throughout the far-infrared, could create this jagged sawtooth pattern in the far-infrared when particles in some size ranges are present.

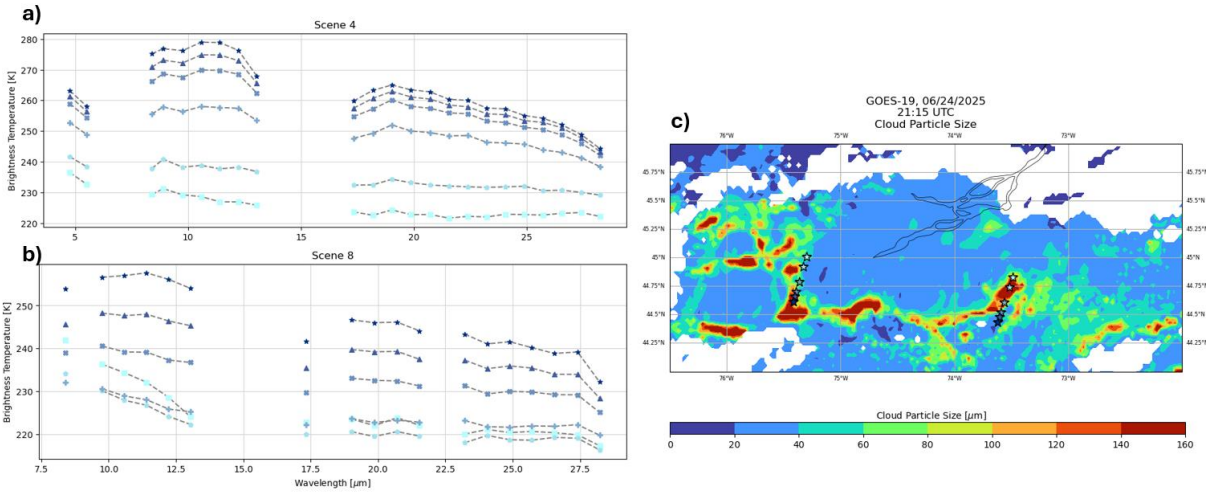

Figure 47: *Two possible larger particle size spectral signatures: a) Observations from Scene 4 the easternmost scene b) Observations from Scene 8, the westernmost scene c) the GOES-19 Cloud Particle Size product, with the locations of the spectral measurements overlaid as blue stars*

Figure 47 (c), on the other hand, shows that the selected spectra from Scenes 4 and 8 are taken from regions with larger particle sizes. The signatures from these regions (**Figure 47** (a) and (b)) are generally flat, with only one or two small kinks. Using similar logic as for the sawtooth pattern, we might expect that if this is a particle size signature, it would come from regions of low extinction efficiency variability with respect to wavelength and particle size. Both **Figure 43** and**Figure 44** present model findings from Yang et al (2013) that show that larger particle sizes demonstrate less variability in extinction efficiency in general, even at larger wavelengths – but that extinction efficiency does still retain some variability at these larger wavelengths (unlike at smaller (larger) wavelengths (wavenumbers), where extinction efficiency is relatively constant). This observation may hold with spectral signals that present as largely flat, with one or two slight variations – exactly what is shown in **Figure 46** (a) and (b).

This remains merely preliminary work. Further, more quantitative study is needed to more thoroughly explore these signatures and to rule out potential contamination from instrument noise. We present here only one possible explanation, with an eye towards in the future potentially leveraging it to develop a particle-size algorithm.

5.2. Towards quantitative far-infrared ice cloud property retrievals

We will now use this case of continental convection to investigate another potential application of far-infrared information. The far-infrared, as discussed previously, may have the capacity to compensate for current weaknesses in the mid-infrared split-window technique. While mid-infrared and shortwave windows complement each other well in the day-time, when the particle size and optical depth limitations of each method can be compensated for by the other method, a weakness arises in the night-time, when shortwave information is no longer available. It is likely that the far-infrared can contribute to the refinement of measurements in this realm: as noted, for optically thick clouds, brightness temperature differences in the far-infrared vary strongly enough to conclusively distinguish particle size (Yang et al. 2003). This variation, unlike in the mid-infrared window, holds true to larger particle sizes and is not confounded by optical depth. Brightness temperature differences between certain far-infrared channels also display sensitivity to the optical thickness of optically thin clouds, which are more opaque to the far-infrared than they are in the MIR. This allows for a stronger level of optical depth distinction than is currently possible with just mid-infrared window channel measurements (Yang et al. 2003; Saito et al. 2020)

The methodology proposed in Yang et al. (2003) can for the first time be applied to actual data to investigate the utility of the far infrared in the split-window use case. We will focus here on the optically thick particle-size case, where Yang posits that taking the brightness temperature difference between a strongly absorptive water vapor channel and a channel at the edge of the far-infrared dirty window can provide optical depth-insensitive information about particle size. The proposed relationship is shown in **Figure 48**, showing a relationship that depends on optical depth only for very small particles.

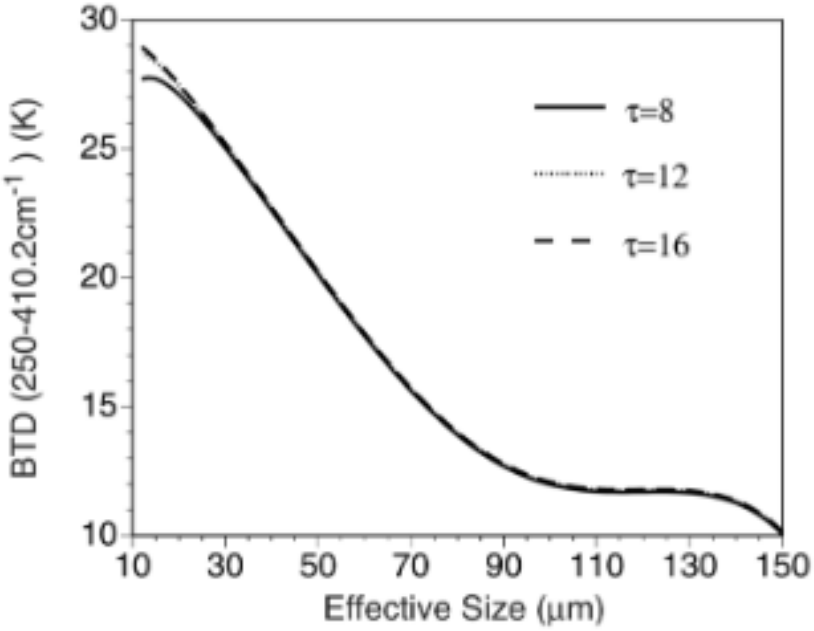

Figure 48, *from Yang et al. 2003: Brightness temperature difference between two channels v_1=250 cm^{-1}and v_2 = 559.5 cm^{-1}, for three ice cloud optical thicknesses.*

Before attempting to create an effective far-infrared split-window, we first sought to use a known case of convection to verify that PREFIRE data would effectively resolve mid-infrared split-window expectations. **Figure 49** repeats the geostationary satellite context shown in **Figure 45** and introduces additional information from the cloud phase, cloud optical depth, and cloud particle size products provided in GOES-19 Level 2 data. In order to compute the split-window using PREFIRE data, PREFIRE fields of view were filtered using the GOES-19 cloud phase product to include only cirrus-phase fields of view. They were then further filtered to include only points associated with the storm itself, as opposed to surrounding non-anvil cirrus. The final points used to calculate the split-window are shown overlaid on the cloud phase product imagery in **Figure 49**(b).

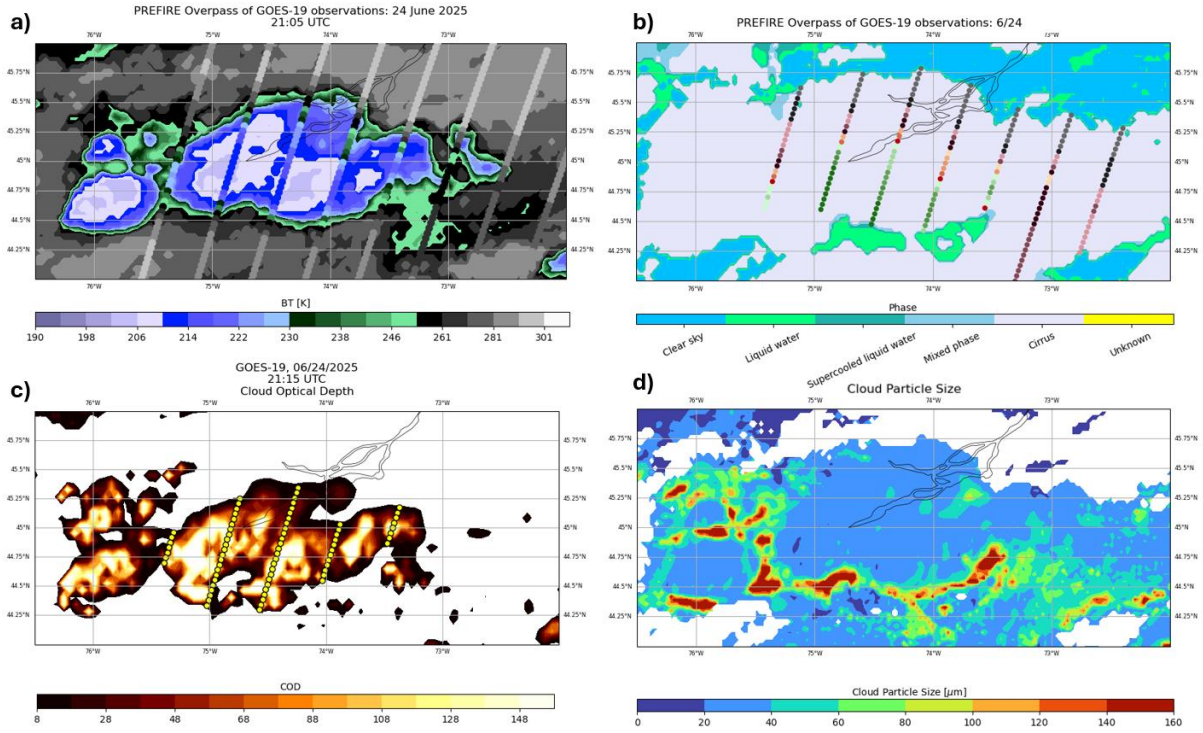

Figure 49: *GOES-19 products for this case: (a) window-channel brightness temperatures; (b) GOES-19 L2 Cloud Phase product with PREFIRE tracks overlaid showing filtering to be used for the mid-infrared split-window; (c) GOES-19 L2 Cloud Optical Depth product; (d) GOES-19 L2 Cloud Particle Size product*

This mid-infrared split-window is computed using the 11.41 and 12.23 μm channels on SAT1 and the brightness temperature used for the x-axis is the 11.41 μm channel. The computed split-window is shown in **Figure 50**. It displays the distinctive arcing pattern of the idealized split-window channel. The points in the computed window are colored on a spectrum from northernmost observation to southernmost observation, with marker shape determined by the scene the observation was taken in. This is to provide a sense of location to the split-window to see how well these observations line up with reality; it is found that most of the farthest north observations, taken at the northern edge of the storm, where optical depth is minimal, are clustered by the $\tau = 0$ and $\tau = 0.5$ regions of the arc. The southern observations, where optical depth is highest, are shown clustered by the larger optical depth isolines. Particle size is more difficult to identify location for, but the largest particles (those where the brightness temperature is smaller) appear to have been identified largely in the southern observations in Scenes 5 and 8, where GOES identifies the largest particle sizes. We can thus conclude that

PREFIRE is capable of successfully resolving a classical infrared split-window. This result is extremely exciting, as it shows that despite PREFIRE's coarse resolution, we are able to acquire real-world data that closely resembles theoretical models, which bodes well for the future potential of developing far-infrared retrievals based on PREFIRE data.

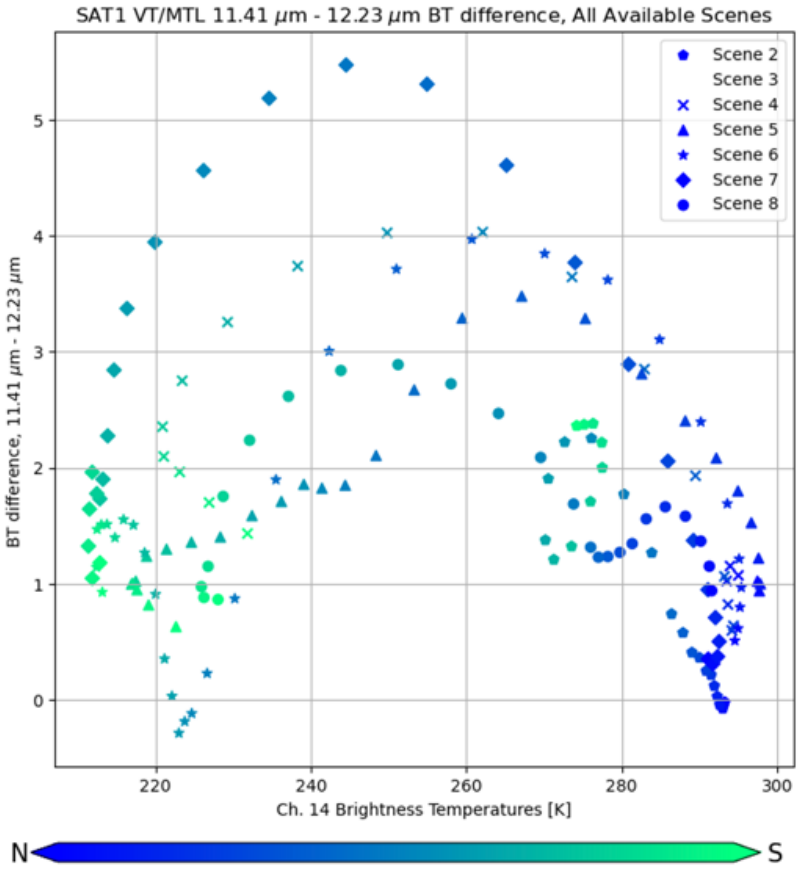

Figure 50: *Results of performing a mid-infrared split-window technique on PREFIRE data.*

Having verified that PREFIRE is capable of effectively resolving current split-window techniques, we will investigate a potential far-infrared split-window using two different splits: one that takes the difference between a channel in the far-infrared dirty window and a channel in the mid-infrared clean window, and one that performs the methodology proposed in Yang et al. (2003). The split-window using this methodology will use the GOES-19 Cloud Optical Depth product (**Figure 49**(c)) to filter the observations to ensure an optical depth of greater than 8, where the proposed methodology should be most effective. The other split-

window will use the filtering shown in **Figure 49**(b), to identify only cirrus clouds observations. Both theoretical split-windows are shown in **Figure 51**.

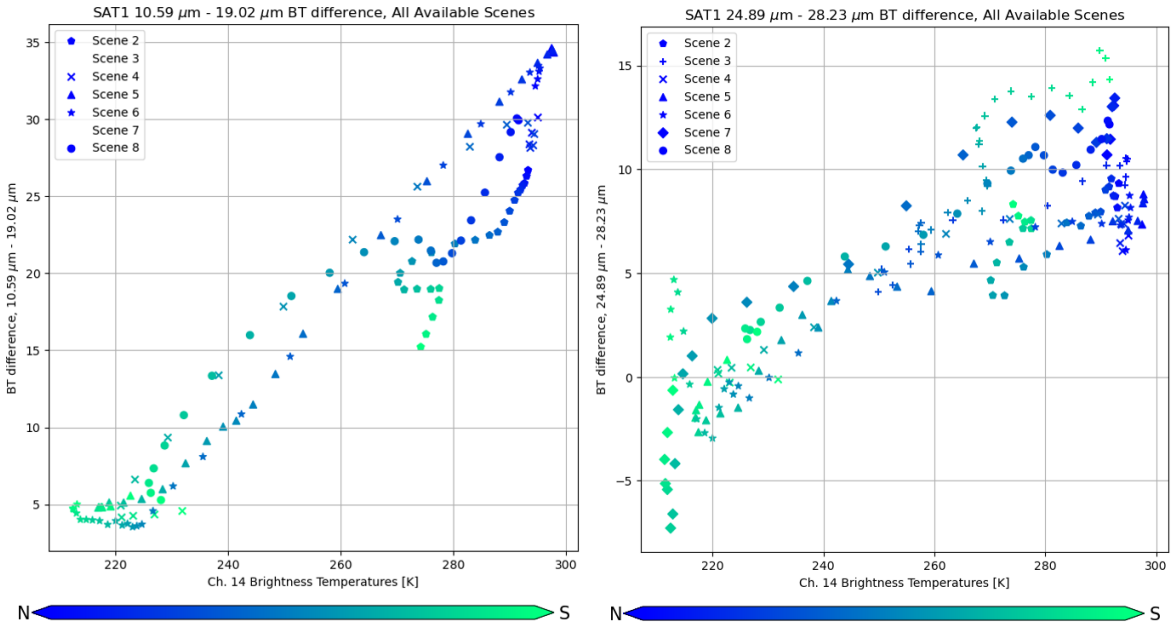

Figure 51: *Results of performing a far-infrared analysis on PREFIRE data. Left y-axis: 10.59 μm – 19.02 μm; Right y-axis: 24.89 μm – 28.23 μm. X-axis is 11.41 μm for both analyses.*

The dirty split-window shown in **Figure 51**(a) shows a very strong positive relationship (rvalue = 0.96, pvalue = 8 x 10^{-33}) between the window channel brightness temperature and the 10.59 μm -19.02 μm BTD. The chief excitement in this method lies in the enhanced range of BTDs, an order of magnitude greater than the range of the mid-infrared split-window. This increased range should allow for more detail and hopefully tease out more information about particle size and optical depth than the smaller range provided in the mid-infrared split-window, which (particularly at larger optical depths and larger particle sizes) may produce brightness temperature differences within the margin of error of a given instrument.

While the x-axis in the Yang et al. technique, shown in **Figure 51**(b), is not comparable to the x-axis in the theoretical model proposed in **Figure 48**, a distinct positive relationship between the 24.89 μm and 28.23 μm BT difference and the Ch 14 (11.41 μm) brightness temperature is shown. This relationship shows locational clustering – a distinct line of window channel 220 K observations from the southernmost points of Scene 2 and Scene 6 stays between -5

and 5 K BTD, while a notable cluster of large BTDs is present in the northernmost observations, where window channel brightness temperatures are warmest. While Ch 14 brightness temperatures are on their own independent of effective particle size (nominally, they are fully dependent on optical depth), in convective cloud systems they can still serve as an approximate locational indicator of where larger particle sizes would be expected – their value as a height indicator in this context means that they perform well at identifying updraft locations (and thus convective pedestals) and in a convective context those updraft locations often pinpoint expected larger particle sizes.

Comparing this to the GOES-19 Cloud Particle Size product by inlaying the calculated BTD and filtering to ensure the optical depth of the measured clouds is greater than 8 (filtering shown in **Figure 49**(c)) shows a loose relationship between BTDs between -5 and 5 and larger recorded cloud particle sizes (**Figure 52**).

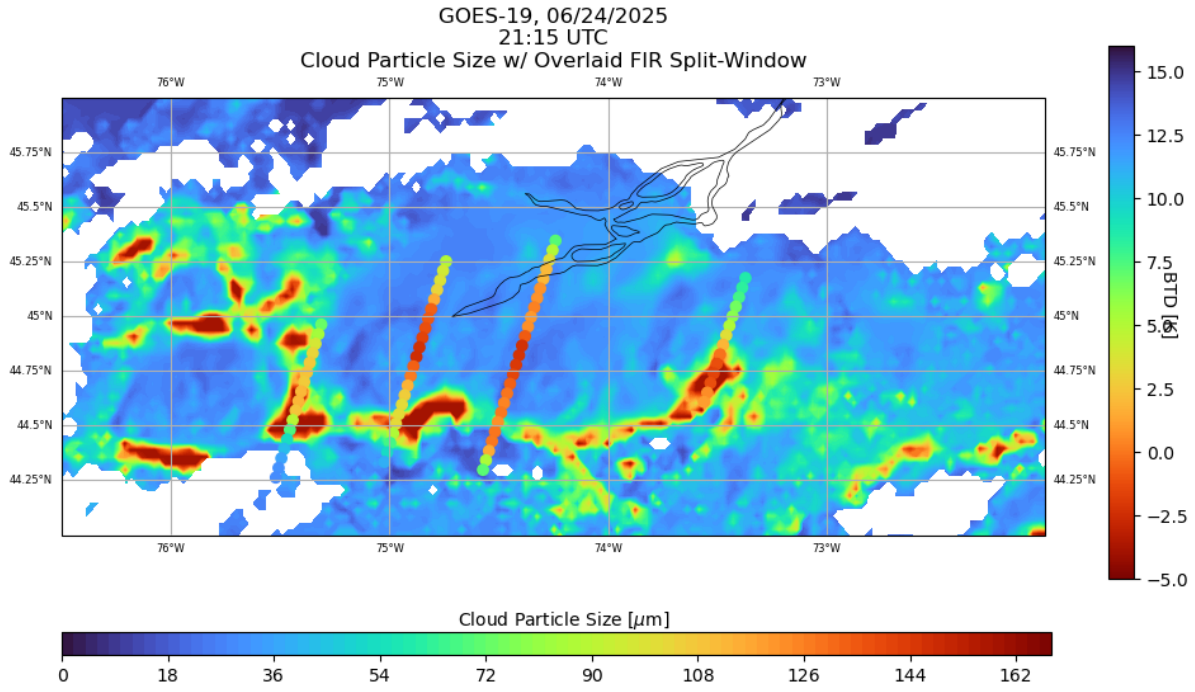

***Figure 52**: GOES-19 Cloud Particle Size product with PREFIRE tracks overlaid showing the results of a theoretical far-infrared split window. The colormap for the PREFIRE tracks is reversed from the colormap for the geostationary data to reflect that we expect smaller magnitude brightness temperature differences to occur where particle sizes are larger.*

While this is by no means a conclusive algorithm, the loose relationship here indicates that, with a future in-depth analysis of the water vapor signatures present in these BTDs, an algorithm in the far-infrared for cloud particle size can be teased out. Future progress in the PREFIRE products that will eventually make large swaths of the FIR-2 band available should also contribute to the efficacy of this algorithm; the further into the FIR-2 band, the more strongly absorbing the water vapor channel, leading to what is hopefully a clear discernment between particle sizes.

Chapter 6. Potential for refinement of initial convection-finding algorithm based on spectral analysis

Based on the findings of our qualitative spectral analysis, we propose a modification of the initial PREFIRE convection-finding algorithm, which had relied solely on a window-channel brightness temperature threshold. Considering initial spectral characteristics summarized in the schematic in Chapter 4.5 and folding these characteristics into the far-infrared split-window theory, we propose using a far-infrared brightness temperature difference in order to identify convective cloud-tops along the PREFIRE track.

We have observed in our case studies that the coldest regions of strongly convective storms display the smallest difference in brightness temperatures between the classic longwave IR window and the far-infrared dirty window. We have previously understood this to be an effect of high clouds reaching far enough into the upper troposphere/tropopause that the far-infrared dirty window serves as a “clean” dirty window. If we assume that these high clouds can be generally associated with cases of strong convection, we may be able to use this BTD to enhance the PREFIRE convection-finding algorithm and to present a less arbitrarily chosen threshold for convective storms.

As a first test, we will apply a preliminary version of this methodology to the case studies we have already examined. For each case, we took the full orbit the PREFIRE observation occurred in and calculated the brightness temperature difference between each of five selected far-infrared dirty window chanels and the traditional longwave IR window (SAT1 channel 14, or the 11.41 μm chanel); these channels are displayed in Table 1.

Table 1

Channel	**SAT1 Wavelength [μm]**	**Spectral significance**
20	16.51	Edge of dirty window band/carbon dioxide band
21	17.33	Rathke microwindow
22	18.18	Rathke microwindow
23	19.02	Rathke microwindow
24	19.86	Edge of far-infared dirty window band

These channels encompass the majority of SAT1's observations of the far-infrared window band. Future analysis will include SAT2 observations, which offer additional bands centered at slightly different wavelengths and will slightly increase overall spectral resolution, but current analysis is restricted to SAT1, as no SAT2 cases were used in this work. A preliminary analysis of this methodology is shown using the Ontario storm (**Figure 53**), the original mid-latitude (Iowa) storm (**Figure 55**), and the Congo storm (**Error! Reference source not found.**). For each storm, we display the results of filtering with BTD thresholds of 1, 2, and 3 K.

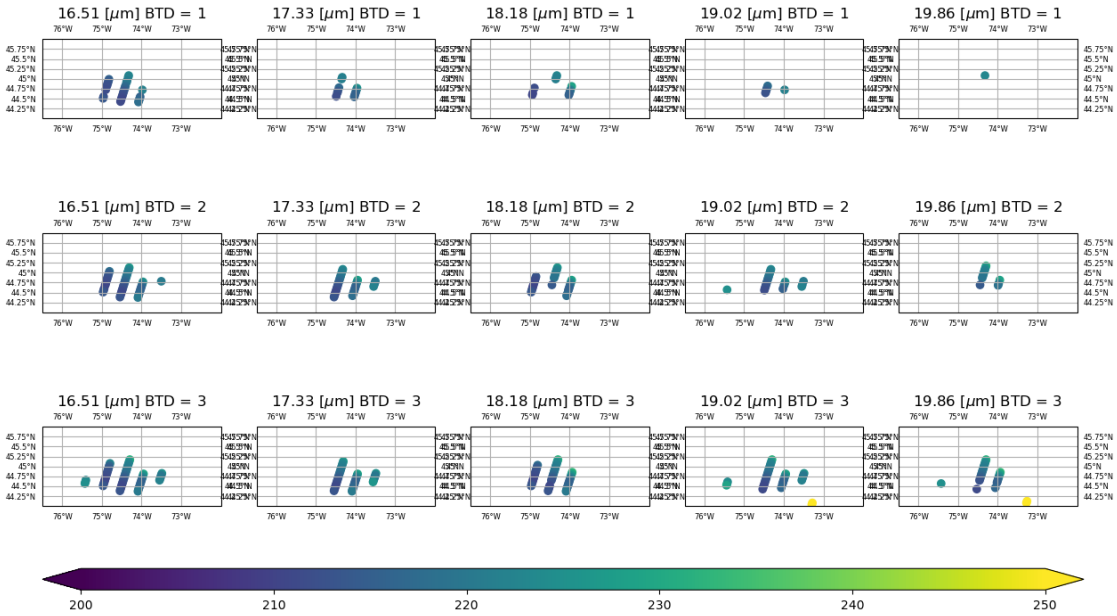

Figure 53: *Ontario case PREFIRE tracks for 16.51 μm, 17.33 μm, 18.18 μm , 19.02 μm, and 19.86 μm window-channel brightness temperature differences, filtered for BTD thresholds of 1, 2, and 3 K; colorbar in BT [K].*

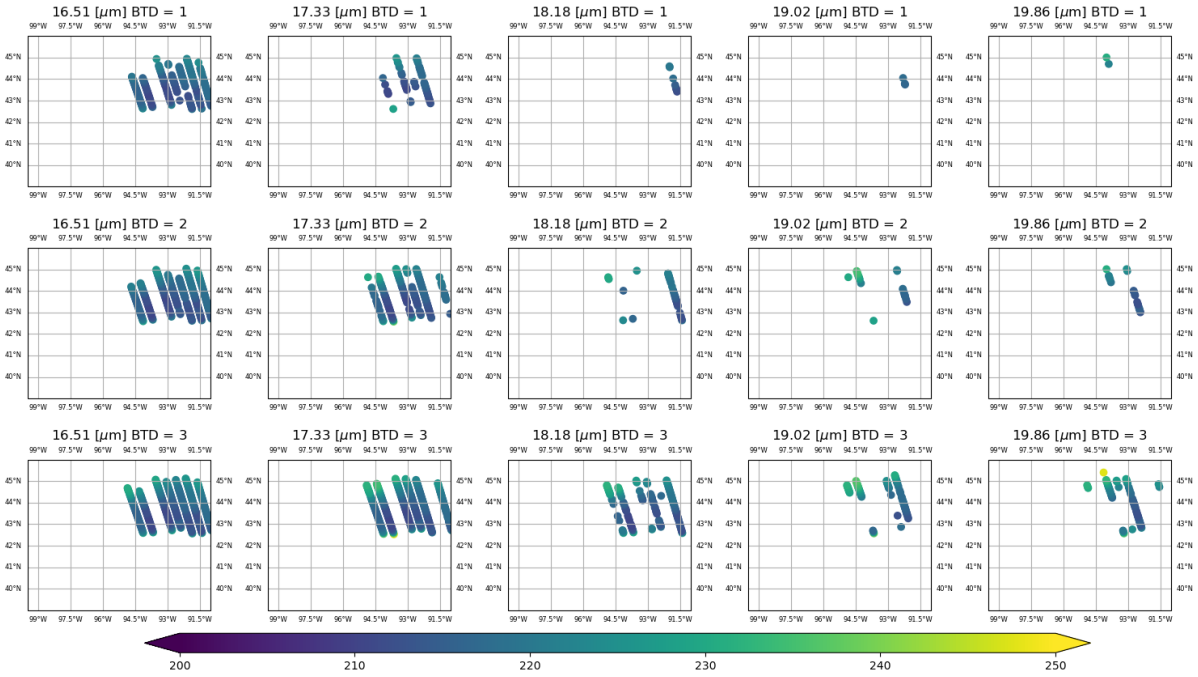

Figure 54: *As in* ***Figure 53****, for the mid-latitude storm.*

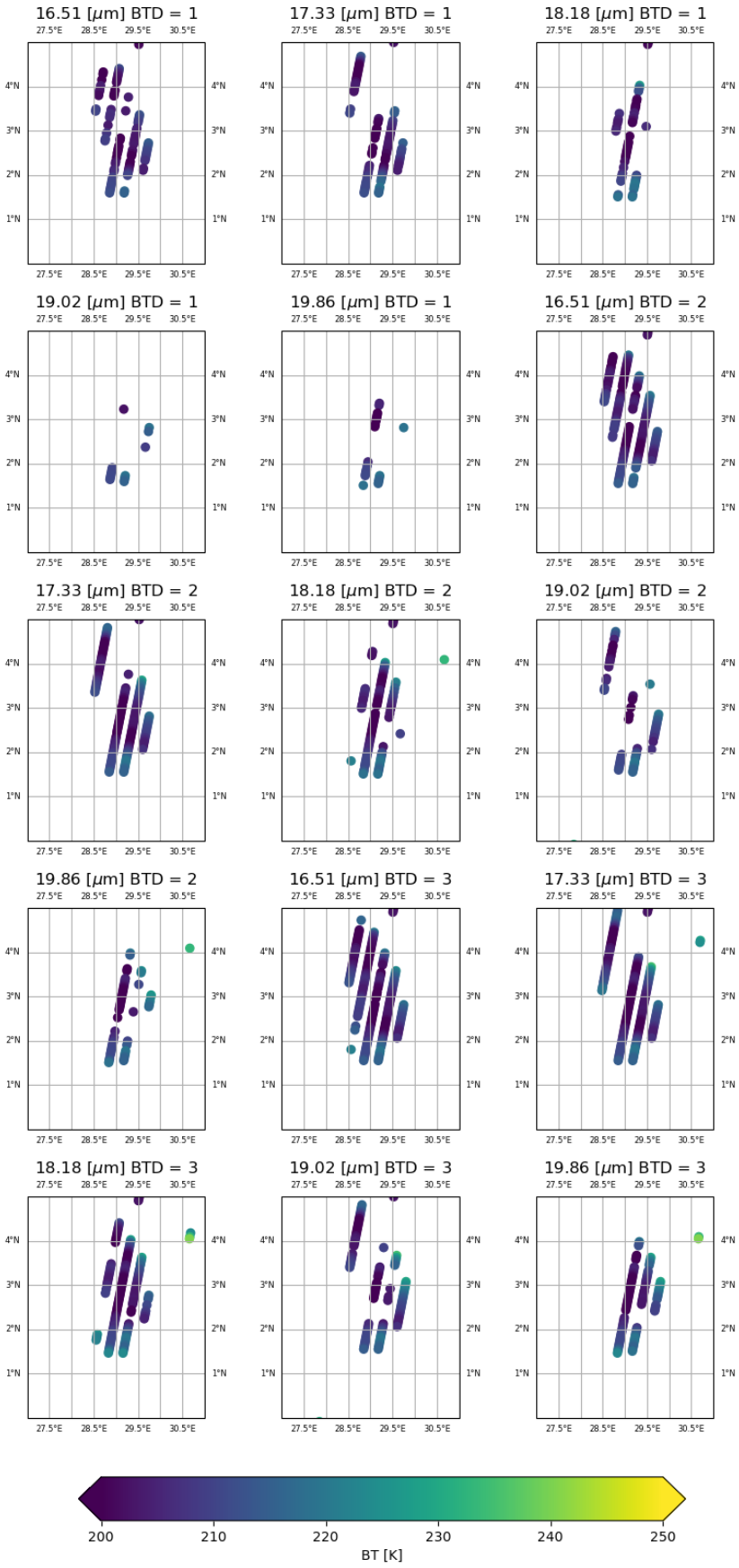

Figure 55: *As in* ***Figure 53****, for the Congo storm*

Comparison of these brightness temperature difference plots suggests that the 16.51 and 17.33 μm channel provide a diagnostic metric that identifies the majority of the coldest parts of these storms while largely filtering out the warmer sections; larger BTD thresholds in the longer wavelengths capture much of the same parts of these storms. Performing this same analysis with just a brightness temperature threshold of 215 K produces the results shown in **Figure 56**.

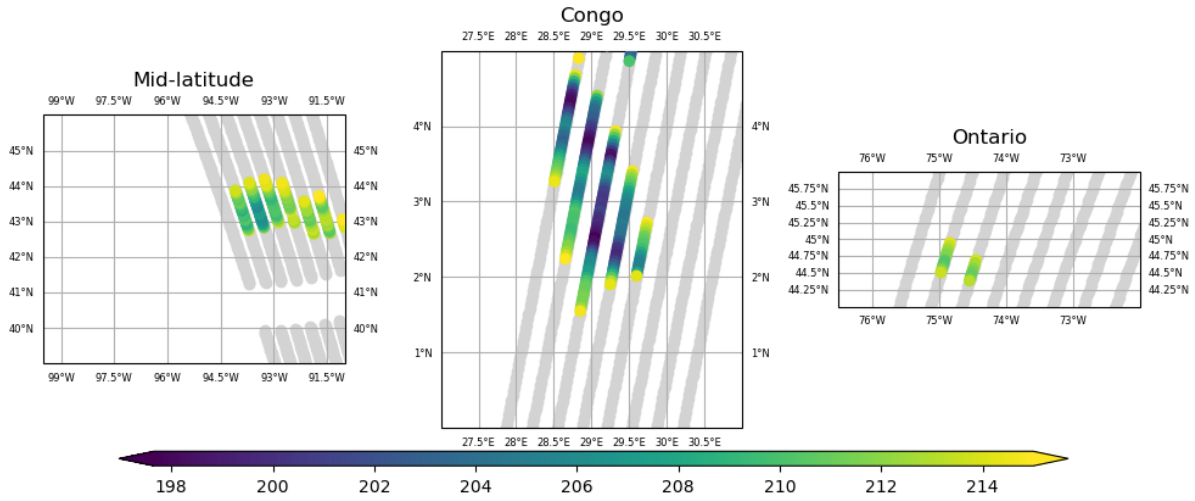

Figure 56: *Analysis performed with brightness threshold of 215 K; brightness temperatures shown with colorbar, with PREFIRE tracks shown in light grey*

Comparisons of the results from each of these algorithms indicate that, while both successfully identify the cases in question, using a brightness temperature difference is a more selective procedure and pinpoints more specifically the colder cores of the storms in question. It also requires less locational fine-tuning than the threshold method does. For example, in Ontario, while it is clearly a convective storm, applying the same brightness temperature threshold (215 K) to this case as we did to the Iowa and Congo cases identifies far less of the storm than in those cases.

More analysis is needed to determine if pixel count thresholds are necessary and to effectively analyze the relative efficacies of each method, but this brightness temperature dfffference method shows promise and would be an exciting new way to incorporate far-

infrared studies into the detection of convective storms while hopefully being more selective, precise, and consistent about the identification of truly intense storms.

Further progress will be assisted greatly by the implementation of Version 2 PREFIRE data, which should be available in the upcoming months; for this reason, we have not performed more in-depth analysis at this time.

Chapter 7. Lifecycle incorporation

With our analysis of oceanic convection in Chapter 4.4, we touched on the role of storm lifecycle stage in the radiative signal of a convective storm. Now, we will begin to lay the groundwork to investigate lifecycle stage in more rigorous detail. This is appealing as an area of study to attempt to identify not only variations in spectral observations, but to continue to build on an improved convection-seeking algorithm: can PREFIRE detect different lifecycle stages of a storm, and can this detection help with far-infrared characterization? As our discussion in Chapter 4.4 touched on, the evolution of microphysical and cloud extent characteristics throughout the lifecycle of a storm has significant impacts on the radiative properties of that storm. This evolution may show up in the far-infrared spectrum.

We will attempt first to develop a methodology for the diagnosis of lifecycle stage. In these first stages, we will rely heavily on geostationary spatial context. We will first identify storm lifecycle stage with the sole use of geostationary data and then follow it up with a PREFIRE-based spectral analysis. Future work will seek to identify couple these PREFIRE spectral characteristics with the observed storm lifecycle stage to allow for identification in a PREFIRE-contained workflow, possibly create PREFIRE satellite products for this application, and contribute further to a body of work in the far-infrared focused on storm lifecycle characterization. This broader goal will require significant quantitative and

statistical analysis that is currently beyond the scope of this work, so for now we will constrain ourselves to more case study-based analysis.

Our diagnostic methodology will derive heavily from a combination of Futyan and Del Genio (2007) (FDG) and Roca et al. (2017). We begin with a general characterization of the mesoscale system, following Houze (1989), which defines first the physical structure of the cloud shield of an MCS. They propose that this is composed of a convective core, a stratiform rain anvil region, and a non-precipitating stratiform anvil region. While the convective core is difficult for coarser-resolution satellites such as PREFIRE to resolve, the core + the surrounding regions of more intense precipitation can be considered the "pedestal" or "pillar" (as mentioned in Chapter 4.4) of the system and may be more easily resolved with a brightness temperature threshold method similar to that described previously.

In general, the radiative effects of the storm vary over its lifecycle because the composition of the storm – and thus its cloud-top properties – vary over its lifecycle. By some metrics, the non-precipitating portion of the anvil may contribute up to 31% of overall net cloud radiative forcing, in comparison to the 15% contributed by the precipitating portions of the storm (Feng et al. 2011). Diagnosing the lifecycle stage of a storm may help to understand its full radiative effect and to understand how the far-infrared can factor into understanding of these results.

FDG splits the lifecycle of a mesoscale convective system into three contiguous parts based on the evolution of this physical structure: initiation, maturity, and decay. During initiation, deep convection is triggered, a convective core begins to grow vertically, and condensate is brought aloft. As the system moves into maturity, deep convection is still present, but a stratiform anvil and mesoscale circulation build as the cloud material from previously active deep convective cells spreads from those cells and new convection is generated. This

stratiform anvil is the stratiform precipitating anvil; upper-level condensate is removed from the anvil in this manner. Precipitation does not necessarily occur throughout the entire stratiform anvil, but a large anvil cloud, precipitating or non-precipitating, is associated with the mature stage of a convective storm. Decay begins when deep convection stops, the anvil cloud begins to shrink, and precipitation eventually ceases.

With this structure from FDG in mind, we will attempt to identify these stages with satellite data. FDG proposes that these stages can be characterized with two pieces of information: the maximum size of the system and the minimum brightness temperature of the system. Before a system reaches its minimum brightness temperature, it is considered a developing system. After it reaches this minimum brightness temperature, it is considered a mature system. During this period of maturity, the system undergoes horizontal growth as the anvil cloud (both precipitating and non-precipitating) grows. Once the maximum radius is reached, the system begins to shrink and is considered dissipating. This definition allows lifecycle stage characterization to occur regardless of whether or not the full lifecycle is observed, as it relies on the tendencies of the system. The graphical representation of this concept is shown in **Figure 57** and a condensed version is shown in **Figure 58**.

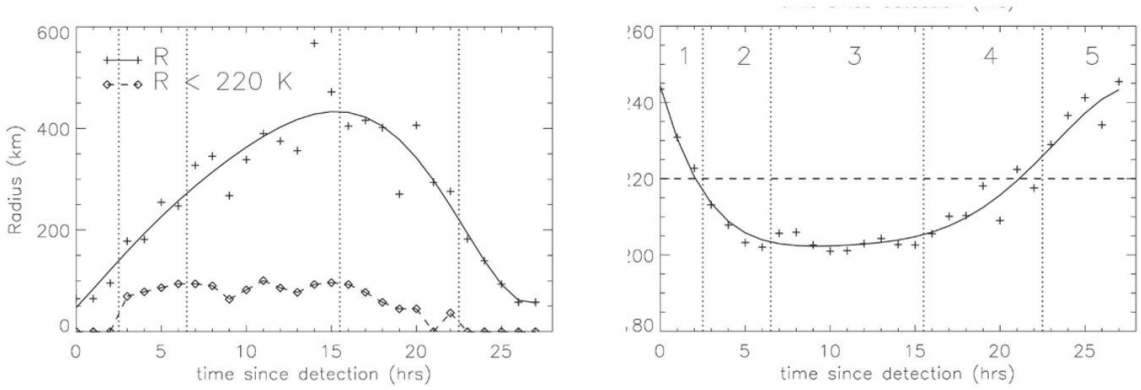

Figure 57*: from Futyan and Del Genio (2007), left: evolution of radius over lifecycle of system; right: evolution of brightness temperature over lifecycle of system. Numbers in right panel give the lifecycle stage: 1: warm developing, 2: cold developing, 3: mature, 4: cold dissipating, 5: warm dissipating.*

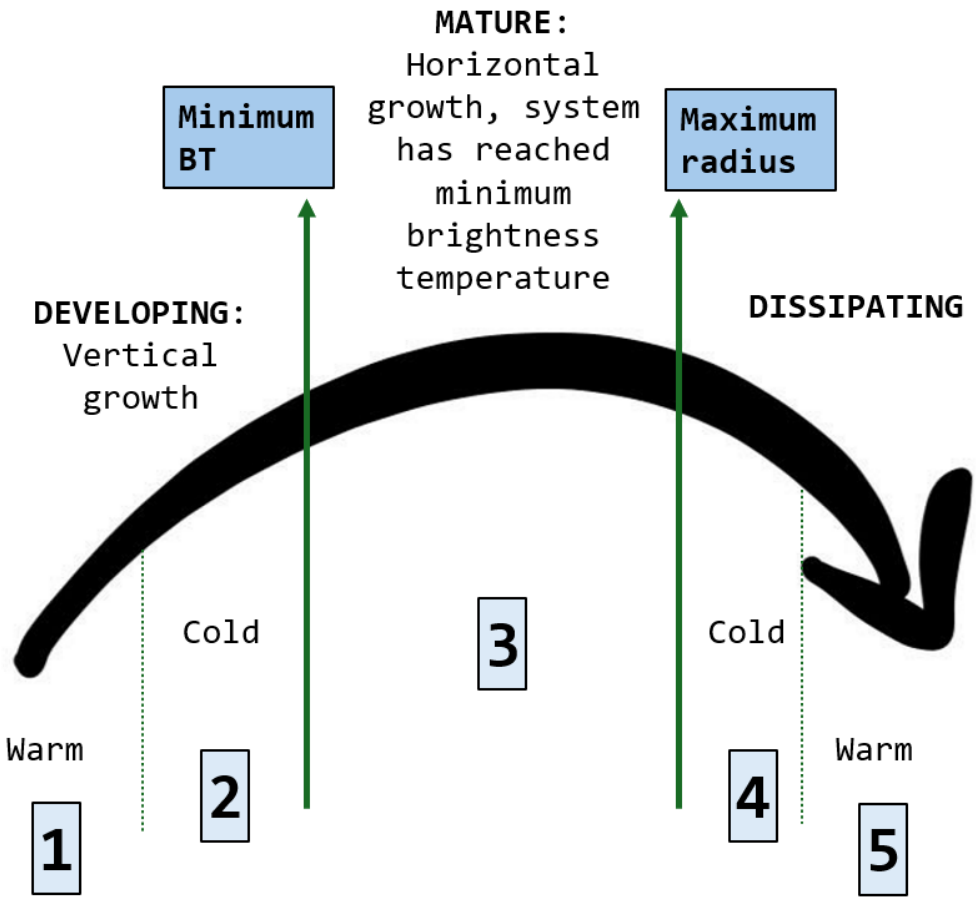

***Figure 58**: a condensed illustration of FDG's proposed lifecycle framework*

Using this concept, we develop a new method for diagnosing system lifecycle stage with geostationary data, to be applied as future algorithmic diagnostic criteria when evaluating PREFIRE convection overpasses. We use two separate methods:

1) Using brightness temperature over the course of the full convective lifecycle. This method is essentially just the preexisting FDG methodology (and in fact our analysis will be modelled off of the result shown in Figure 47(b))
2) Using relative brightness temperature areas over the convective lifecycle.

The second method is somewhat novel. For each geostationary timestep in an identified convective system, we compute the area below 210 K and the area between 210 K and 235 K. The area below 210 K is considered to be representative of the "core" or "pedestal" region – a very tall region with high clouds and likely large condensates. The area between 210 K and

235 K is considered to be representative of the anvil cloud region. The threshold of 235 K is taken from the typically accepted literature threshold for convective regions: much literature on the topic uses 235 K as a separation metric between anvil clouds with associated convective systems and middling or lower cirrus clouds, so we assume that, given a convective system is present already, the area between 210 K and 235 K is a reasonable way to separate out the anvil. By plotting the relationship between these two regions – between 210 K and 235 K, and below 210 K – we expect to be able to combine the two metrics identified in FDG to show one concise plot representing storm lifecycle. The expected result, shaped somewhat like an arrowhead, is shown in **Figure 59**.

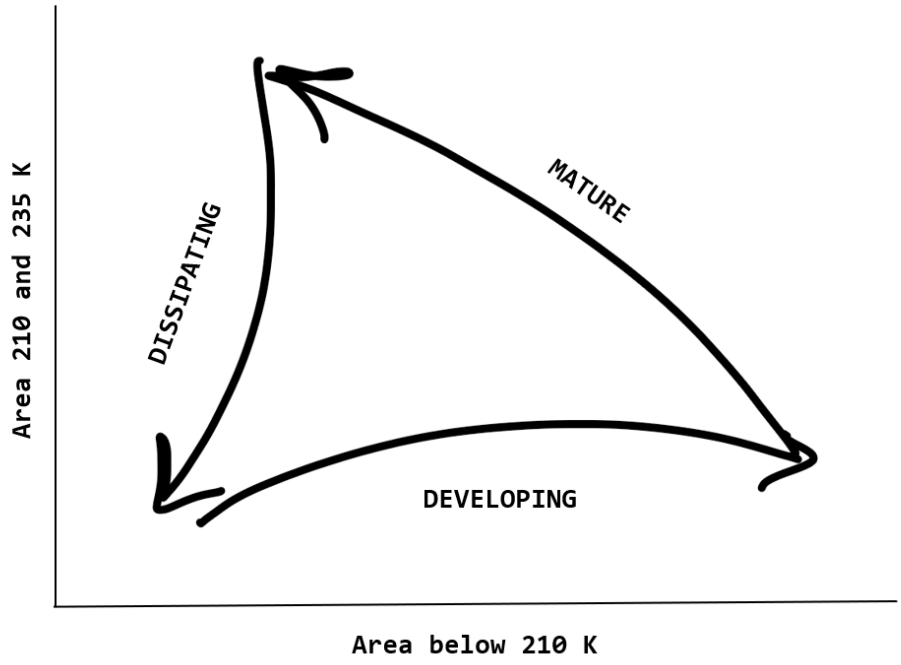

Figure 59: *Expected result of our lifecycle diagnostic methodology*

We anticipate that a developing system would lie on the bottom axis of the arrowhead, where the area below 210 K is growing steadily and the area between 210 K and 235 K is relatively stagnant. This should represent the vertical growth stage in the convective core, where the tall pedestal-like tower is growing but the anvil is not yet developing. Brightness temperatures should be decreasing in general and the area under 210 K should be increasing, but the

slightly warmer anvil regions – the area between 210 K and 235 K – will not be dominant until the storm is approaching maturity.

The inflection point between a developing and mature system would thus be at the point where the area below 210 K is at its maximum – where one might reasonably expect the system to have reached the minimum brightness temperature proposed in FDG – and the area between 210 and 235 K begins to increase. This mature system would then lie along the second arm of the arrowhead, where the area under 210 K is decreasing and the area between 210 and 235 K is increasing. This should correspond physically to the growth of the anvil – that area between 210 and 235 K – and the initial persistence and then steady dissipation of the area below 210 K. The final arm is the dissipating arm, which begins after the system has reached maximum size and the area below 210 K – the pedestal – is at its minimum or is completely gone. We expect that this maximum size would be roughly reflected in our "anvil" brightness temperature area reaching its peak. To test this framework, we will look at two individual cases that SAT1 observed in the spring and summer of 2025. The stage of lifecycle observed by SAT1 was assigned by taking advantage of collocated geostationary data to map the development of the storm, assess the rate of change in area at each individual geostationary timestep, and create the theoretical framework – the lifecycle triangle – described above.

The first of these cases is a storm that developed within the same system as the Iowa case that we have already looked at. This storm developed in the afternoon hours of April 17th, 2025 as a small, isolated part of a much larger storm complex that covered much of the midwestern United States. It develops throughout the afternoon, is observed by SAT1 at 22:35 UTC, and by 01:05 UTC on the 18th has reached full maturity. By 03:00 UTC, it has merged with the larger storm complex and is no longer an isolated storm. The full course of this storm's development is shown in Appendix A; the storm itself is shown in **Figure 60**.

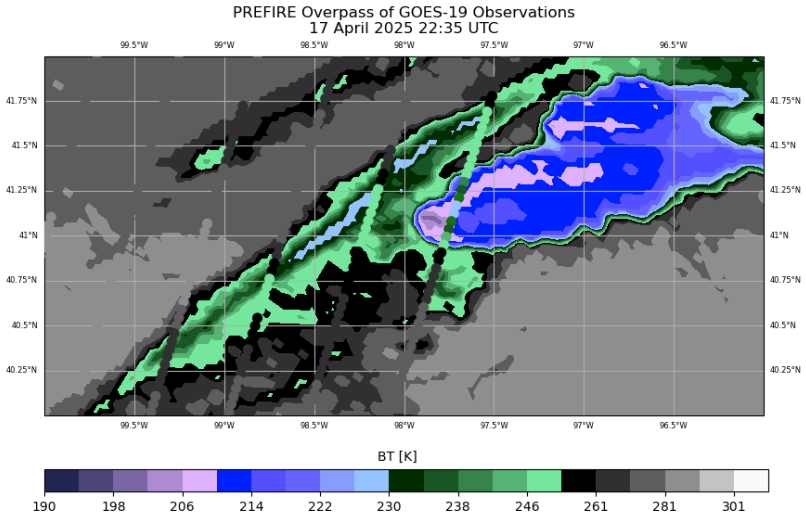

***Figure 60**: GOES-19 observations of our developing case, with the PREFIRE overpass overlaid*

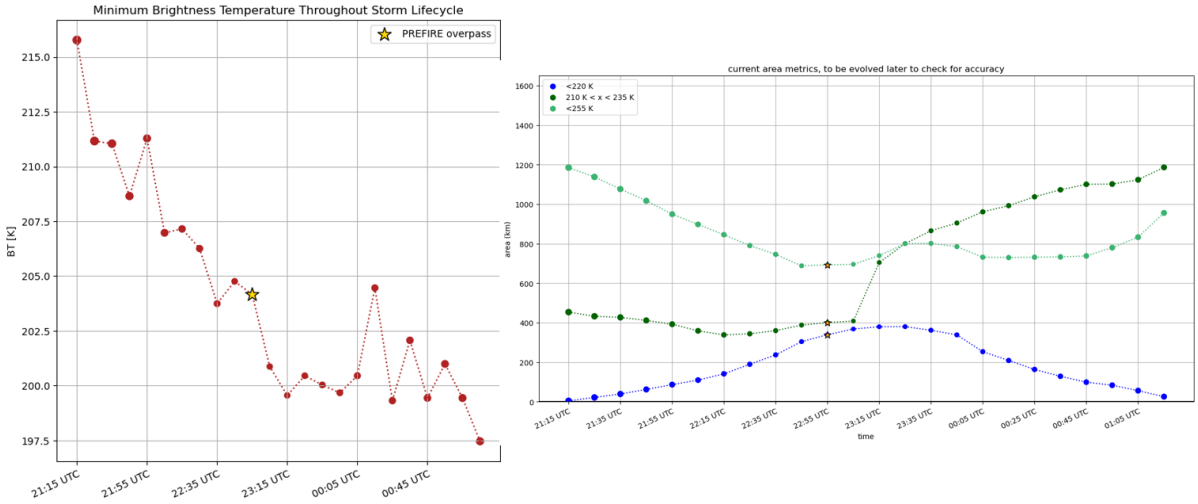

***Figure 61**: Following FDG, left, minimum brightness temperature throughout analyzed portion of storm lifecycle; Right, area of different regions of storm throughout analyzed portion of storm lifecycle*

To determine whether or not this was a developing storm, we analyze the storm first using the methodology proposed by FDG: overall area of storm and brightness temperature minimums. These are shown in **Figure 61**(a) and (b). The brightness temperature is yet to bottom out completely by the time this storm exits the observation region, but it is clear that the PREFIRE overpass occurs in a time period where the storm is steadily getting colder, characteristic of developing convective systems. We also see that the area under 220 K grows from zero, approaches a local maximum, and then decreases back down to nearly zero again. This is not necessarily an expected result, but further investigation of the development of the

storm as it joins the larger complex may explain this result. It is possible that this unusual developmental pattern is an indicator of slight storm dissipation before re-intensification occurs, driven by its merger with the larger storm complex. It is notable that the SAT1 overpass of this storm occurs prior to this local maximum, implying that even if we were to consider this to be a full storm lifecycle followed by a separate re-intensification, the SAT1 overpass can be considered to have occurred in the developing portion of the storm's lifecycle. The area of the storm specifically between 210 K and 235 K does show signs of steady growth without reaching a maximum, while the area below 255 K (which we may consider as an absolute limit of the storm's extent) experiences a local minimum around the same time as the local maximum of the area under 220 K before growing again.

While these are messier results than theoretical, for the purposes of the PREFIRE overpass we can draw two conclusions:

1) Where SAT1 observes the storm is in the developmental stage from an area analysis perspective, regardless of whether or not this analysis represents a full lifecycle.
2) An analysis of the minimum brightness temperatures as the storm progresses indicates that deep convection is still developing in the storm and the storm is not yet fully at maturity.

We can investigate this analysis further using our proposed theoretical framework. The expectation for this storm, under the assumption that the SAT1 overpass was in fact an overpass of a developing storm, would be that the data point representing this overpass is firmly in the developing branch of the lifecycle triangle. When performing this lifecycle analysis, we did not include data points beyond the storm's merger with its larger complex, treating it as the lifecycle was never completed. As a result, we expect to see that the branch we have tentatively labelled as "dissipating" would not be present in this representation, as

the storm as tracked in this study did not experience any weakening or anything that would be representative of dissipation prior to its merger with the larger storm complex.

The analysis using our theoretical framework is shown in **Figure 62**; it is immediately evident that the SAT1 overpass does in fact occur in the branch considered "developing". In this figure, we have provided the data points with a colormap representing the time of observation; the darkest points occurred earliest in the observational timeframe, while the lightest points occurred last. With the addition of this information, we can see that the earliest data points are in fact located in what we would call the "dissipating" branch, but that the latest data points cut off right before the expected inflection point, indicating that we are likely to have cut off our observations midway through the abbreviated lifecycle of this storm.

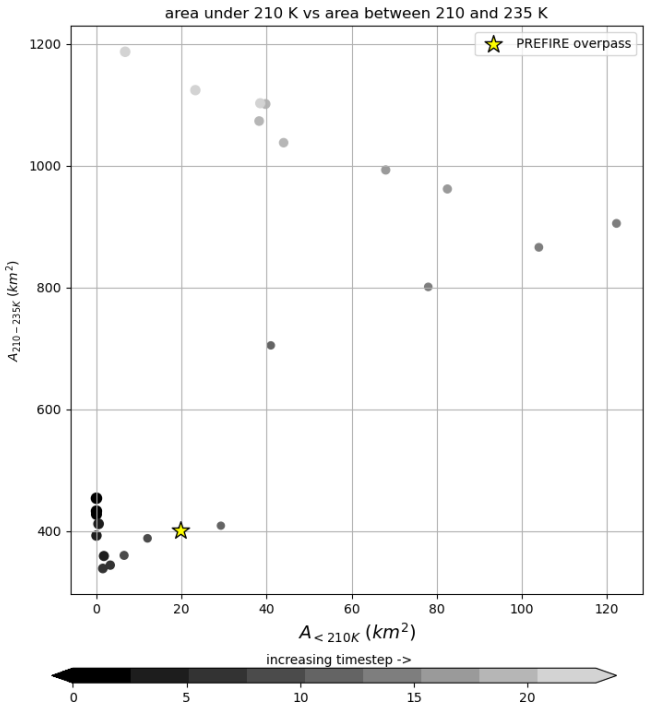

***Figure 62**: Proposed lifecycle diagnostic framework, applied to a case of developing convection over the midwestern United States.*

We can compare this lifecycle result to an example of a mature storm analyzed using this same theoretical framework. We have already analyzed this storm, shown in **Figure 45**, from

a spectral perspective: this is the case of continental convection that occurred over northern New York and southern Ontario. The evolution of this storm is shown in Appendix A, which shows the storm from pre-initiation in the early afternoon of June 24th until dissipation in the early hours of the night, with PREFIRE overpass highlighted in solid white.

A visual inspection of this storm indicates that this overpass coincides very neatly with peak of visual brightness temperature minimums; the convective cores shown in the visible imagery (**Figure 45**(b)) are well-developed and associated with a significant cirrus anvil. This overpass is also conveniently of a well-isolated storm, allowing us to observe the full lifecycle of the system without any merging, splitting, or absorption by a larger storm complex (as was the case for the developing storm in Iowa).

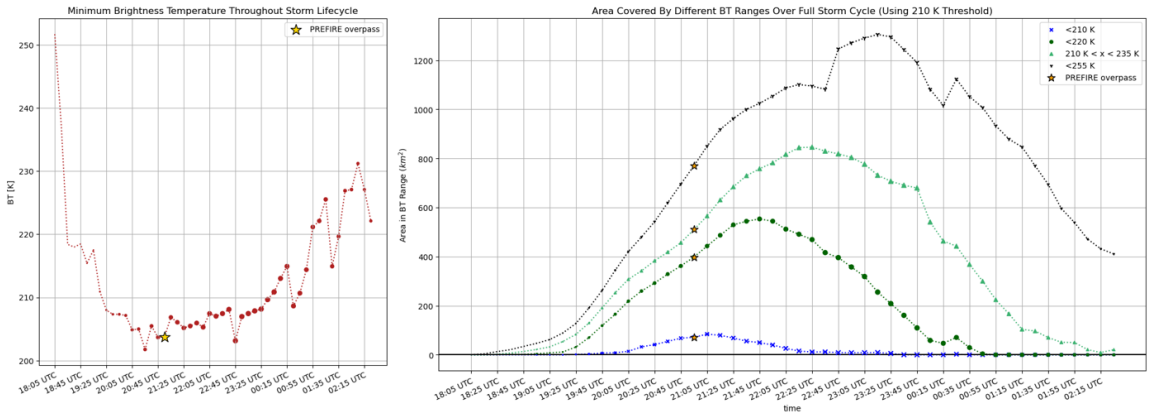

Figure 63: *As in* ***Figure 61****, for a mature case.*

Performing a similar initial analysis of the area and minimum brightness temperature evolution of this storm produces two notable results: one, that the minimum brightness temperature (**Figure 63**, left) behaves approximately as expected, reaching a minimum just around where our overpass occurs; two, that the overpass occurs nearly exactly at the local maximum of the area covered by brightness temperatures under 210 K (just under 100 km^2), and just before the local maximum of the area covered by brightness temperatures under 220 K (this observation is at 400 km^2; the maximum is just under 600 km^2).

A supplementary analysis of the rate of change in this area (**Figure 64**) finds that the overpass occurred just as this rate of change approached a maximum for all metrics that we are considering storm indicators (area under 210 K, area under 220 K, area between 210 and 235 K – the "convective pillar", and area under 255 K); after this maximum, the rate of change decreases before ultimately becoming very negative as the storm weakens and eventually dissipates. This maximum in rate of change is another metric of storm lifecycle stage – maturity centers approximately around this maximum, with the dissipation stage beginning as the rate of the convection slows and the storm begins to weaken.

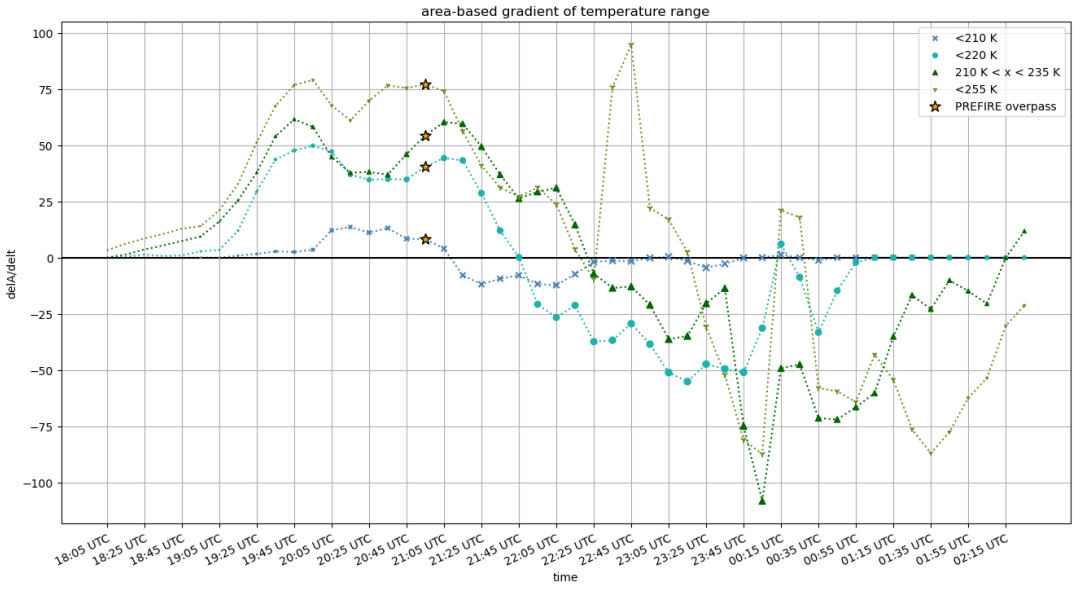

***Figure 64**: Analysis of the rate of change of the area of the storm less than 210 K, less than 220 K, between 210 K and 235 K, and less than 255 K.*

This analysis thus far would indicate that this storm is either firmly mature or just at the end of its development stage; we will now test our theoretical framework to see if this conclusion, drawn using metrics based on existing literature, holds up upon application of a new technique.

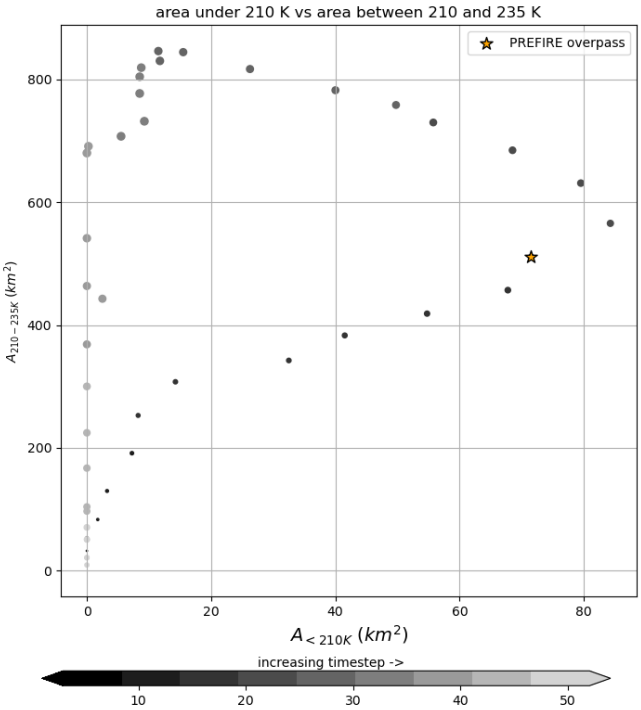

Figure 65*: As in* ***Figure 62****, for a mature case.*

This technique, shown in **Figure 65**, finds that the PREFIRE overpass took place in the upper right corner of the arrowhead figure, right at the end of what we have termed the "developing" branch, nearly exactly around where we begin to call a storm "mature". This holds with the findings of a more literature-based analysis. Further analysis of other storms indicates that this "transition" point is murky at best, as opposed to being a clear inflection point as the theory originally posited, and so this particular benchmark will require more investigation. Regardless, this result falls in line with what we would expect to see in this theoretical framework and is promising for the usage of this framework in a benchmark capacity, where it may help to improve lifecycle stage diagnostics without requiring analysis of the full lifecycle – particularly in cases where the full lifecycle may not be present for any given individual storm.

Having diagnosed the lifecycle stages of these storms, we will begin an area of analysis that future PREFIRE work will seek to build on: lifecycle spectral comparisons. At PREFIRE's lower spectral resolution and lacking the FIR-2 spectral region, it is unclear exactly how

distinct the differences between these two storms may be, but it is valuable to lay down the groundwork of comparison in order to build future work off of it. Introductory spectra, consisting of all spectra from scenes of interest in the PREFIRE overpasses, are shown in **Figure 66** for each of these storms, with imagery of the storms themselves repeated on the right for ease of comparison.

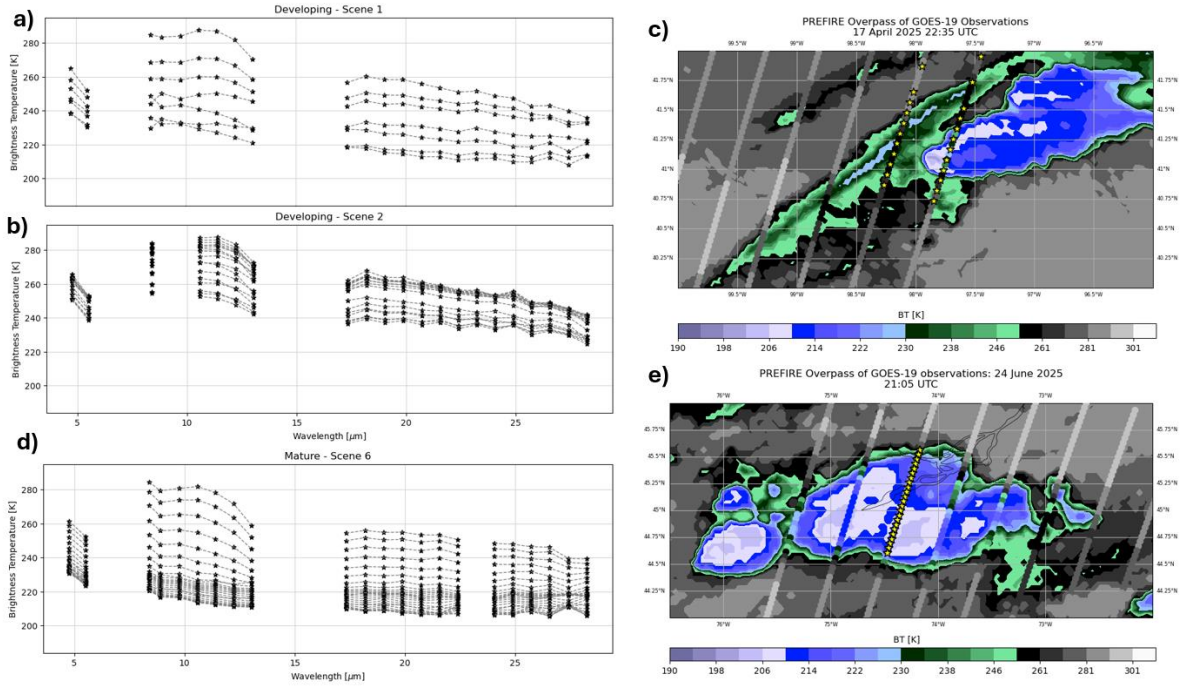

Figure 66: *Spectral analysis of a developing and a mature storm. A and B): observations from Scene 1 and Scene 2 as PREFIRE overpassed the developing storm (C). D) observations from Scene 6 as PREFIRE overpassed the mature storm. E): Mature storm geostationary imagery with stars indicating the locations spectral observations come from.*

The most obvious difference is that the developing storm (left top and middle, right top) has a far less developed convective region and displays far fewer cold brightness temperatures; the mature storm, on the other hand, has nearly peaked in terms of the extent of its convective pillar and these cold cloud-tops are refected in both geostationary imagery and PREFIRE spectra. In the mature case, the expected agreement/disagreement between the dirty and clean windows is present, with colder regions in agreement and warmer regions presenting as colder in the far-infrared than in the clean window band; in the developing case, this analysis

is less simple to make as the 15.96 μm band is not available even in quality flag-1 data, but the relationship seems to hold in this case as well. In both the developing and mature cases, there is what we have tentatively diagnosed as a smaller particle size signature present (the jagged, sawtooth patterns visible in the longer wavelength), albeit at much varied temperatures. There is no distinct difference in the behavior of the clean window channels. The overall pattern of the far-infrared in both cases seems approximately the same, with the slight U-shape to the colder brightness temperatures (**Figure 41**, 5th archetype) present in the mature case and ever so slightly in the developing case as well and the clear-sky/less-cloudy arch in the warmer brightness temperatures also present in both cases. The primary difference is mostly morphological and in the geostationary imagery.

While there is not a particularly clear lifecycle distinction in these two case studies, there is promise in the geostationary lifecycle diagnostic tool. If this diagnostic tool is successfully combined with an updated PREFIRE convection finding algorithm and applied to a wide range of cases, it may help to facilitate further investigation as to whether or not there truly is no strong far-infrared difference. The addition of FIR-2 data, likely with the release of Version 2 data in the coming months, will also help to facilitate this more robust, quantitative analysis.

Chapter 8. Conclusions and Next Steps

This study presents an initially survey of the opportunities that PREFIRE data may provide to advance low-latitude convective research. The work was guided by four primary questions:

1) Can we identify convective ice clouds with PREFIRE measurements?
2) How does the full emission spectrum vary across different storm types and regions?
3) How can far-infrared data enhance modern mid-infrared ice cloud property retrievals?
4) Can we begin to incorporate the lifecycle stage of the storm into our analysis?

We find that PREFIRE may successfully identify convective cases in multiple regions of the globe; our initial success came from the usage of pure brightness temperature thresholds, in keeping with geostationary satellite convective detection norms, but in the convective cases studied in this analysis, we found that where convection is strong, far-infrared dirty window brightness temperatures and the traditional mid-infrared dirty window brightness temperatures display strong agreement. Correspondingly, we propose in Chapter 6 that leveraging this agreement may prove more useful than a pure brightness temperature threshold; preliminary investigation indicates that regional variation using this relationship is more minimal than in the window channel, where the location of interest plays a prominent role in the choice of brightness temperature thresholds.

Having successfully identifed convective cases, we sought to answer the second question. We examined convective spectral characteristics in the far-infrared across a variety of regions and lifecycle stages. From this investigation, we produce an initial schematic (**Figure 41**) that represents six primary spectral regimes identified in PREFIRE convective cloud overpasses; this regimes vary somewhat regionally and provide interesting information about local atmospheric composition and the height of the observed convective cloud tops. A possible stratospheric/tropopause signal is identified in cases of convection in Brazil and the Congo, consistent with regional variation in tropopause characteristics (as suggested in Tegtmeier et al. 2020 and Xian and Fu 2015); this intriguing potential signal merits further study beyond the scope of this preliminary investigation. We find that there is significant science-level information in the far-infrared, including some intriguing spectral characteristics attributed to the coldest parts of the convective storms, a compelling potential relationship between convective cloud-top height and the temperature of the far-infrared window band, possible stratospheric water vapor signatures, and some regional variation. All of these characteristics

merit significant further investigation and enhanced quantification beyond this initial qualitative analysis.

We also investigated the third question: the potential, proposed in Yang et al. (2003), that the far-infrared may fill in observational gaps in the current mid-infrared split window. Initial results find that the brightness temperature difference between 10.59 μm and 19.02 μm (a modified split-window) provides an enhanced range in values that may be promising for making clearer distinctions between particle size and optical depth where these values are either extremely large or extremely small – an area where modern retrieval struggle. The brightness temperature difference between 24.89 μm and 28.23 μm, firmly in the far-infrared, provides intriguing clustering patterns that may be able to distinguish convective storm regions, as well as demonstrating some promise in the identification of larger particle size signatures – again, a retrieval that modern techniques struggle with. While much more work is needed to devise a truly functional algorithm capable of leveraging these results, initial results are extremely promising.

Finally, we took the first steps to answer the fourth question by developing a lifecycle analysis structure that aims to remove the necessity of observing the full storm cycle when performing a lifecycle analysis, in order to attempt to diagnose storm lifecycle stage at the time of a PREFIRE overpass without performing extensive manual identification. This novel lifecycle analysis framework shows some promise in the isolation of lifecycle stage without requiring the full context of a storm lifecycle, which may help to facilitate analysis for storms that do not undergo a traditional or complete lifecycle. Initial comparisons of one developing-stage storm and one mature-stage storm do not show significant far-infrared variation across lifecycle stage; we seek to refine the PREFIRE convection-seeking algorithm to attempt to locate more developing cases in order to facilitate further spectral comparisons. The

brightness temperature difference methodology, still in its infancy, may present some promise in this regard.

We find, overall, that the addition of PREFIRE data to low-latitude convective research shows significant promise and may contribute greatly to further scientific development, particularly in the enhanced characterization of clouds and further research into their radiative impacts.

8.1. Next steps

This preliminary, exploratory study opens several avenues for future work. In support of Chapter 3 showed that convection can be clearly identified in PREFIRE spectra. In the future, we will expand on this finding to develop an algorithm for identifying convection, analogous to currently-operational algorithms (e.g. TOOCAN (Fiolleau and Roca 2013) and tobac (Sokolowsky et al. 2024)) based on other observational platforms. This algorithm will incorporate methodology proposed in Chapters 5 and 6 and aim to support further PREFIRE-based investigation of the preliminary studies conducted in Chapters 4, 5, and 7. These studies require a large body of convective cases; identifying these cases with the assistance of a PREFIRE-tailored algorithm that does not require manual verification will enable us to perform quantitative, statistical analysis across a large swath of regions and storm types.

Building on the enhanced data access afforded by this algorithm development, we will then supplement our analysis with the σ-PREFIRE radiative transfer model, a radiative transfer model currently in development that is tailored to PREFIRE-style measurements, based on far-infrared enhancements made to the σ-IASI model (Masiello et al. 2024)). Using the flexibility afforded by the σ-PREFIRE model, we will more conclusively identify the source of the spectral characteristics highlighted in Chapter 4, identify the impact of changing cloud type, cloud height, atmospheric composition, and other environmental factors on the far-

infrared spectra observed by PREFIRE, and ensure that the brightness temperature difference thresholds identified for this proposed convection-finding algorithm are identifying the appropriate regions of convection and convective cloud signatures.

Chapter 5 demonstrated that there is significant promise in far-infrared brightness temperature difference-based particle size retrieval techniques. We will use the addition of the σ-PREFIRE model, as well as additional real-world cases identified by a more fleshed-out convection-finding algorithm, to build upon the promise of these methodologies and develop the first quantitative ice cloud effective radius retrieval from spaceborne far-infrared measurements. One of the main confounding factors in the framework proposed in Chapter 5 is the significant water vapor absorption present throughout the FIR-1 band; the experimentation allowed by the σ-PREFIRE model will allow us to understand the impact of water vapor absorption on the brightness temperature differences observed in our preliminary FIR split-window and to use this information to move towards the development of this particle size and optical depth retrieval framework.

Finally, Chapter 7 introduced a new method for characterizing storm lifecycle that warrants additional study. We will further develop this lifecycle framework to use in tandem with a fully-fleshed out convection-finding algorithm, as well as the σ-PREFIRE model, to conclusively identify lifecycle signatures (or a lack thereof) in PREFIRE data. This work will benefit from incorporating data from the Global Precipitation Mission's IMERG gridded precipitation product to clarify lifecycle stage in terms of storm rainfall production. IMERG will provide useful precipitation information that will again help to clarify lifecycle stage and storm structure, enhancing confidence in retrievals and helping to diagnose spectral quirks. Additional upcoming and currently available satellite projects will also contribute to this goal: the Earth Cloud, Aerosol, and Radiation Explorer (EarthCARE), launched in 2024, will provide a valuable vertical dimension to PREFIRE's current two-dimensional footprint. In

particular, the Cloud Profiling Radar (CPR) on EarthCARE will provide valuable environmental context and validation to interpretations of PREFIRE retrievals that will help to contextualize not only particle size and optical depth retrievals, but particle phase and vertical structure information that will help in efforts to clarify the lifecycle stage of convective storms.

There are also a number of potential avenues for future analysis to better understand links between convective intensity and radiative effects that were not directly addressed in this study. For example, the INvestigation of Convective UpdraftS mission (INCUS), set to launch in 2028 or 2029, will provide valuable information on vertical transport in convective storms, which adds additional critical snapshot-level detail about the lifecycle stages of these storms; cross-validation with PREFIRE data will provide an additional level of confidence for any data interpretation. In general, this work provides many exciting stepping stones to future research and future work will seek to expand on this groundwork.

Appendix A

Iowa case study lifecycle, 18 April 2025:

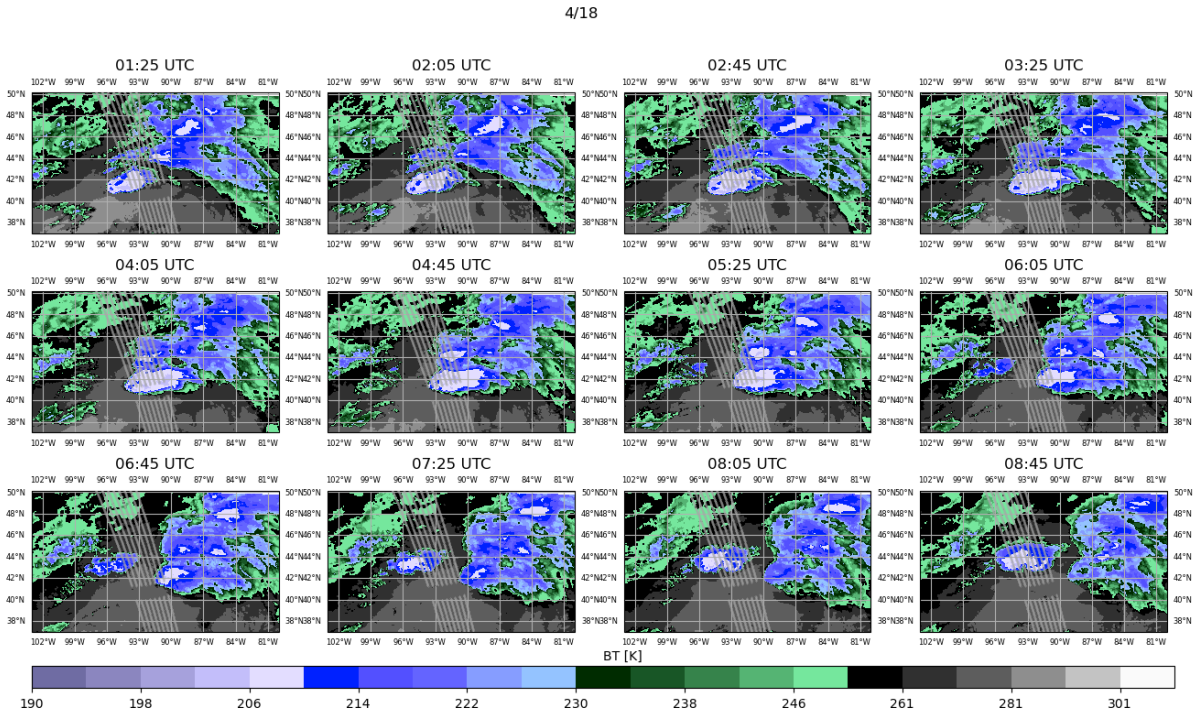

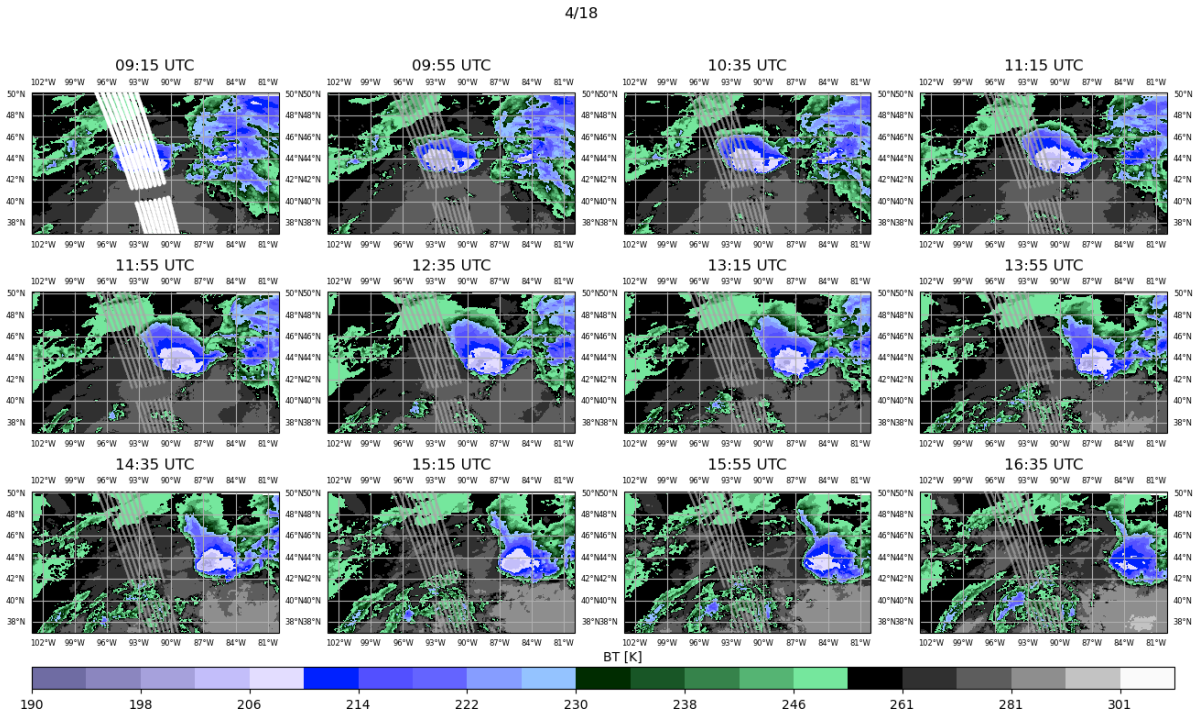

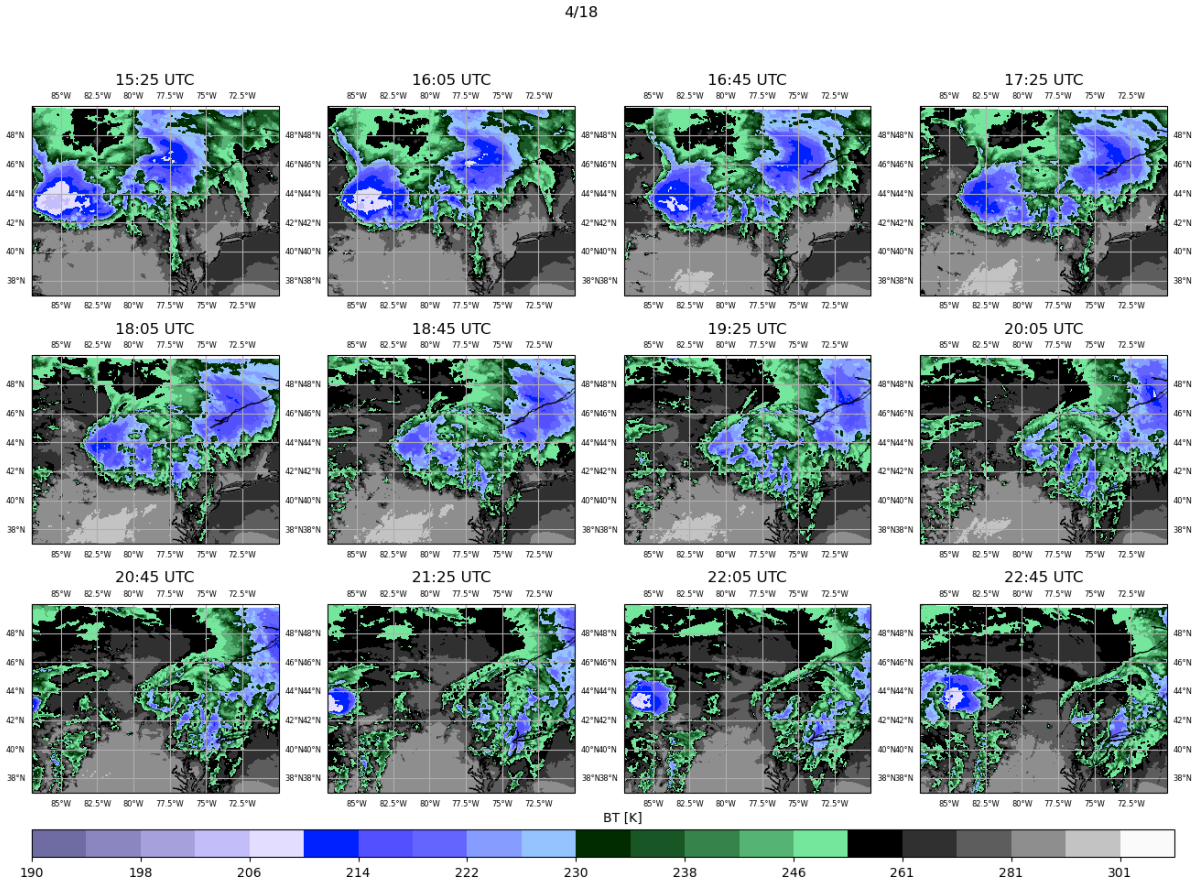

Iowa case study lifecycle, 17 April 2025:

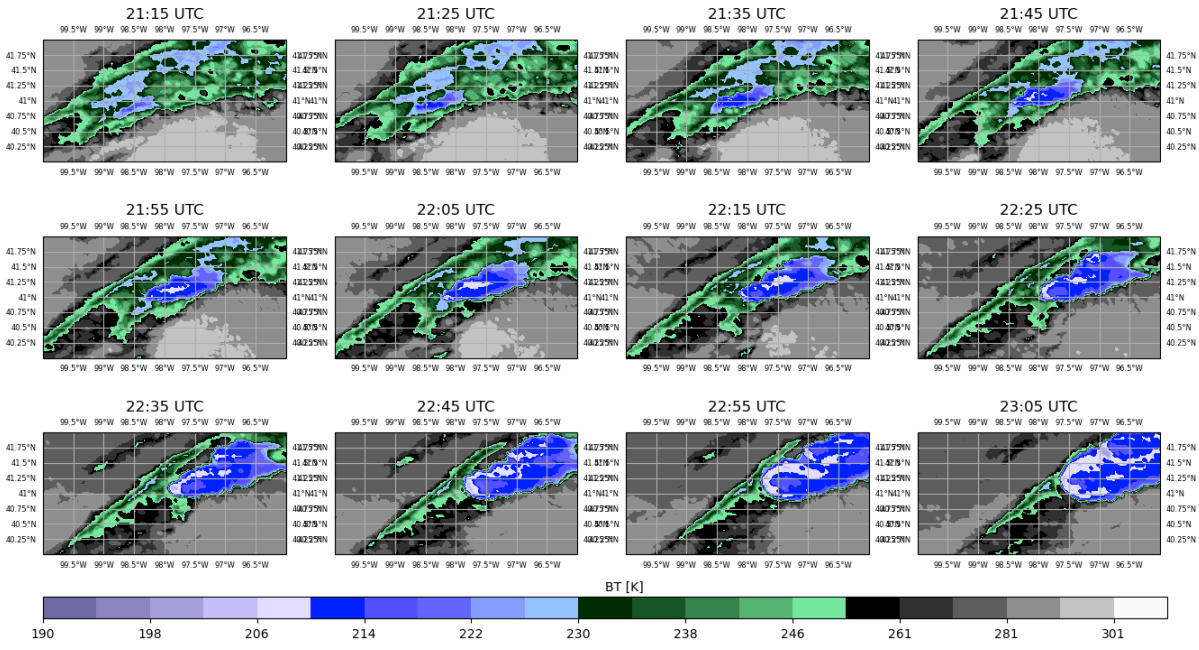

Brazil case study lifecycle, 12 March 2025:

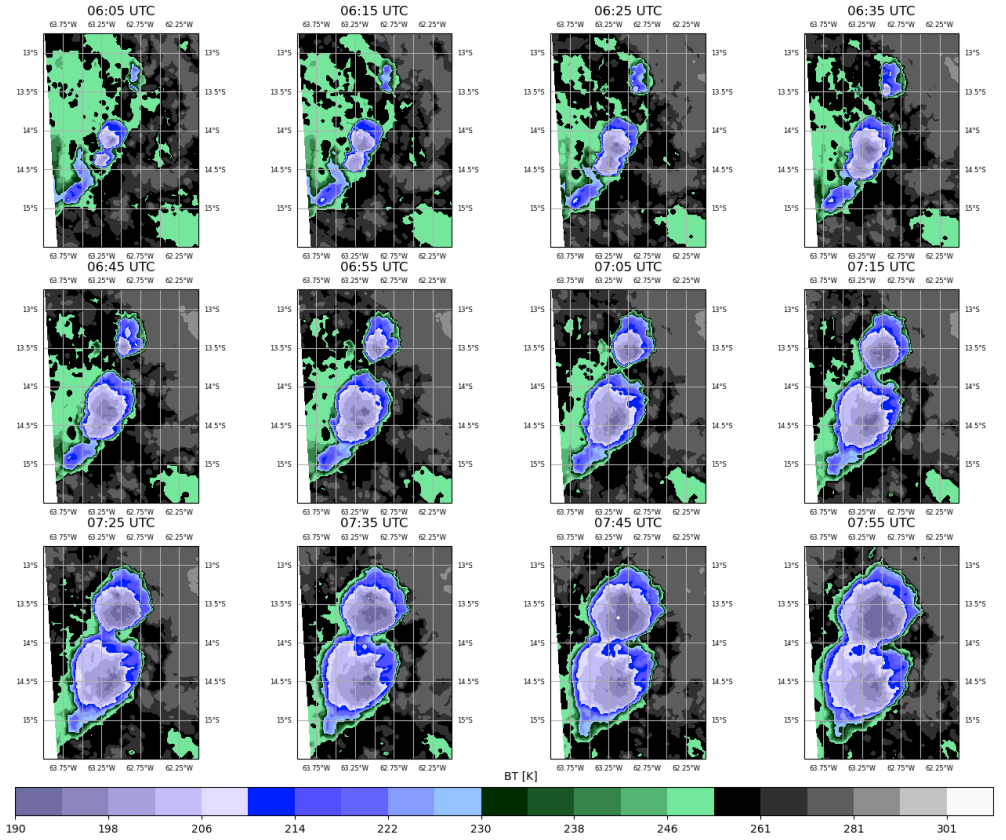

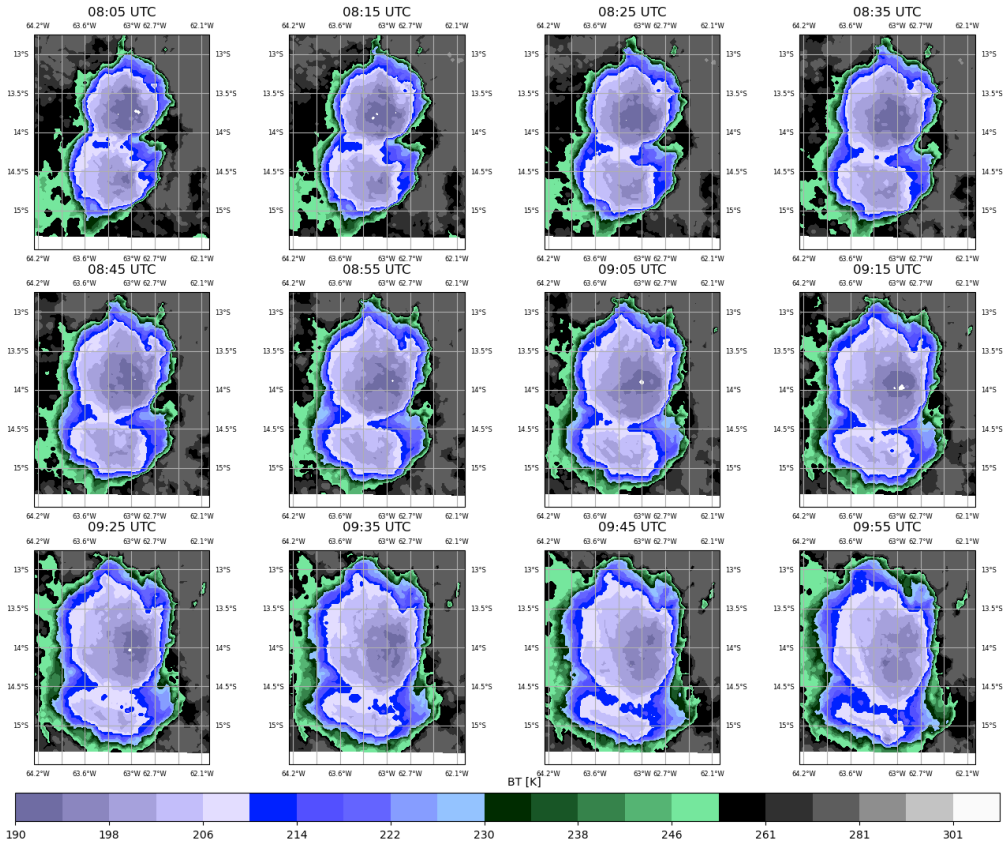

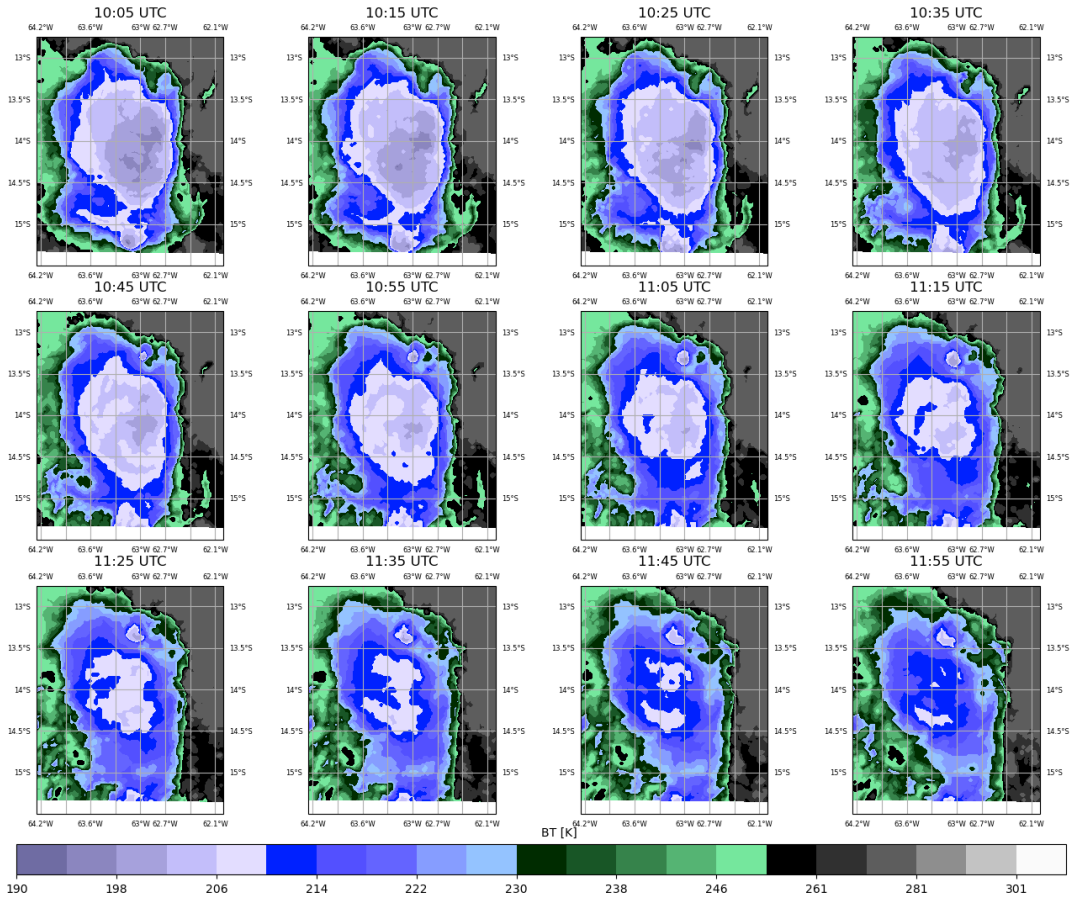

New York/Ontario/Quebec/Vermont case study lifecycle, 24 June 2025:

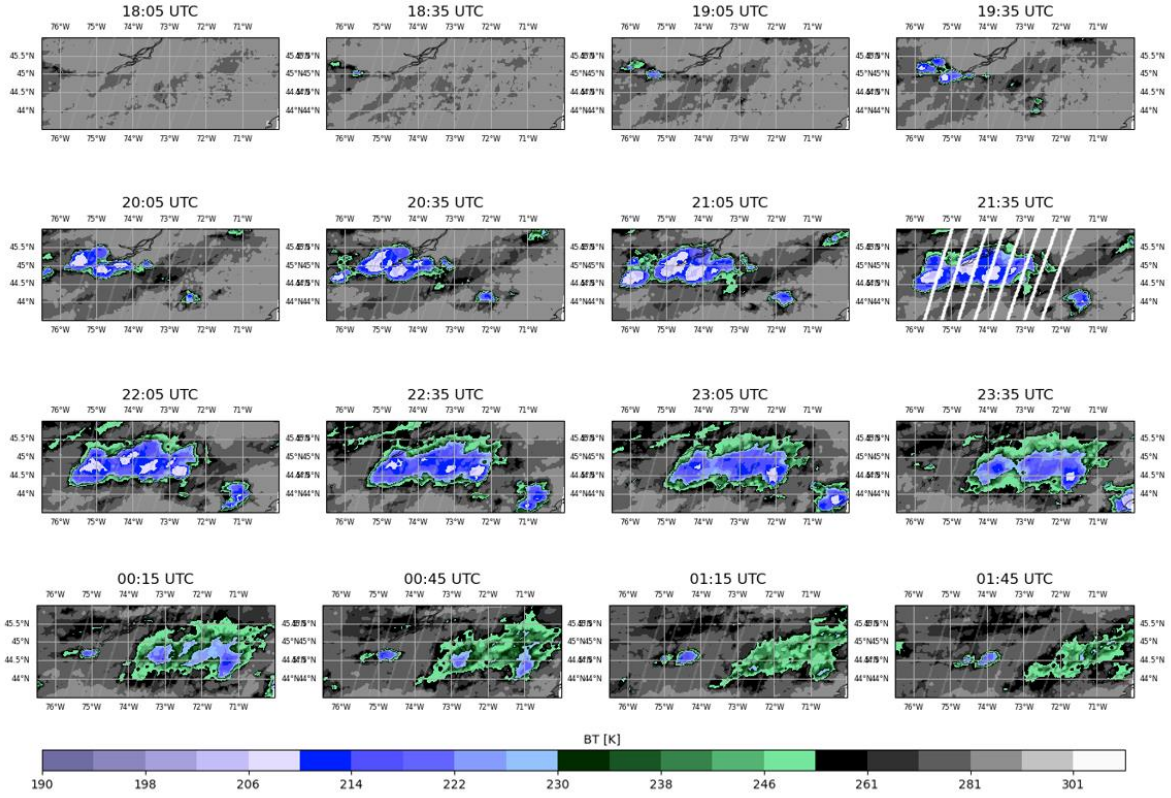

References

Ackerman, S.A., and Coauthors, 2019: Satellites see the world's atmosphere. *A Century of Progress in Atmospheric and Related Sciences: Celebrating the American Meteorological Society Centennial, Meteor. Monogr.,* No. 59, Amer. Meteor. Soc., https://doi.org/10.1175/AMSMONOGRAPHS-D-18-0009.1.

Andrews, D., 2000: *An Introduction to Atmospheric Physics*, Cambridge Univ. Press, Cambridge, U. K.

Bantges, R. J. and Coauthors, 2020: A test of the ability of current bulk optical models to represent the radiative properties of cirrus cloud across the mid- and far-infrared. *Atmos. Chem. Phys.*, **20**, 12889-12903, https://doi.org/10.5194/acp-20-12889-2020.

Baran, A. J., 2005: The dependence of cirrus infrared radiative properties on ice crystal geometry and shape of the size-distribution function, *Q. J. Roy. Meteor. Soc.,* **131,** 1129 – 1142, https://doi.org/10.1256/qj.04.91.

—, 2012: From the single-scattering properties of ice crystals to climate prediction: A way forward. *Atmos. Res.,* **112**, 45–69, https://doi.org/10.1016/j. atmosres.2012.04.010.

—, P. Hill, K. Furtado, P. Field, and J. Manners, 2014b: A coupled cloud physics–radiation parameterization of the bulk optical properties of cirrus and its impact on the met office unified model global atmosphere 5.0 configuration. *J. Climate*, **27**, 7725–7752, https://doi.org/10.1175/JCLI-D-13-00700.1.

Bedka, K., R. Dworak, J. Brunner, W. Feltz, 2012: Validation of Satellite-Based Objective Overshooting Cloud-Top Detection Methods Using CloudSat Cloud Profiling Radar Observations, *J. Appl. Meteor. Climate,* **51,** 1811-1822

Berry, E. and G. G. Mace, 2014: Cloud properties and radiative effects of the Asian summer monsoon derived from A-Train data, *J. Geophys. Res. Atmos.*, **119**, 9492-9508, https://doi.org/10.1002/2014JD021458.

Clerbaux, C. and Coauthors, 2009: Monitoring of atmospheric composition using the thermal infrared IASI/MetOp sounder, *Atmos. Chem. Phys.,* **9**, 6041-6054, https://doi.org/10.5194/acp-9-6041-2009.

Coursol, L. Q. Libois, P. Gauthier, and J.-P. Blanchet, 2020: Optimal Configuration of a Far-Infrared Radiometer to Study the Arctic Winter Atmosphere. *J. Geophy. Res. Atmos.,* **125,** e2019JD031773, https://doi.org/10.1029/2019JD031773.

Cox, C. V., J. E. Harries, J. P. Taylor, P. D. Green, A. J. Baran, J. C. Pickering, A. E. Last, and J. E. Murray: Measurement and simulation of mid- and far-infrared spectra in the presence of cirrus. *J. Roy. Meteor. Soc.,* **136**, 718-739, https://doi.org/10.1002/qj.596.

Feng, Z., X. Dong, B. Xi, C. Schumacher, P. Minnis, M. Khaiyer, 2011: Top-of-atmosphere radiation budget of convective core/stratiform rain and anvil clouds from deep convective systems, *J. Geophys. Res.,* **116,** D23202, https://doi.org/10.1029/2011JD0166451.

Fiolleau, T. and R. Roca, 2013: An Algorithm for the Detection and Tracking of Tropical Mesoscale Convective Systems Using Infrared Images From Geostationary Satellite, *IEEE Trans. Geosci. Remote Sensing*, **51**, 4302-4315, https://doi.org/10.1109/TGRS.2012.2227762

Fox, C., 2015: Far-infrared spectral radiance studies: Application to water vapour and cirrus. PhD thesis, Imperial College London, 182 p., https://doi. org/10.25560/25752.

Futyan, J. M. and A. D. Del Genio, 2007: Deep Convective System Evolution over Africa and the Tropical Atlantic, *J. Climate*, **20**, 5041-5060

Gasparini, B., P. J. Rasch, D. L. Hartmann, C. J. Wall, and M. Dütsch, 2021: A Lagrangian Perspective on Tropical Anvil Cloud Lifecycle in Present and Future Climate, *J. Geophys. Res. Atmos.,* **126**, e2020JD033487, https://doi.org/10.1029/2020JD033487.

Ge, J., X. Hu, Q. Mu, B. Liu, Z. Zhu, J. Du, J. Su, Q. Li, and C. Zhang, 2024: Contrasting characteristics of continental and oceanic deep convective systems at different life stages from CloudSat observations, *Atmos. Res.*, **298,** 107157, https://doi.org/10.1016/j.atmosres.2023.107157.

Goody, R. M., 1964: *Atmospheric Radiation*, Oxford Univ. Press, New York.

Hansen, J. E., and J. B. Pollack, 1970: Near-infrared light scattering by terrestrial clouds. *J. Atmos. Sci.,* **27**, 265–281, https://doi.org/10.1175/1520-0469(1970)027<0265:NILSBT>2.0.CO;2.

Harries, J., B. Carli, R. Rizzi, C. Serio, M. Mlynczak, L. Palchetti, T. Maestri, H. Brindley, and G. Masiello, 2008: The Far-infrared Earth. *Rev. Geophys.,* **46**, RG4004, https://doi.org/10.1029/2007RG000233.

Hartmann, D. L., B. Gasparini, S. E. Berry, and P. N. Blossey, 2018: The Life Cycle and Net Radiative Effect of Tropical Anvil Clouds, *J. Adv. Mod. Earth Sys.,* **10**, 3012-3029, https://doi.org/10.1029/2018MS001484.

Heidinger, A. and M. J. Pavolonis, 2009: Gazing at cirrus clouds for 25 years through a split window. Part I: Methodology. *J. Appl. Meteor. Climatol.,* **48**, 1100–1116, https://doi.org/10.1175/2008JAMC1882.1.

— and Coauthors, 2020: ABI cloud products from the GOES-R series. *The GOES-R Series: A New Generation of Geostationary Environmental Satellites*, Elsevier, 43–62, https://doi.org/10.1016/B978-0-12-814327-8. 00006-8.

— and Coauthors, 2026: A GEO-Ring of Spectral Radiances: Toward a Next Generation of the International Satellite Cloud Climatology Project (ISCCP-NG), *Bull. Amer. Meteor. Soc.*, **107,** E291-E308, https://doi.org/10.1175/BAMS-D-24-0161.1.

Heymsfield, A. J., and Coauthors, 2017: Cirrus Clouds. *Meteor. Monogr*., **58**, 2.1–2.26, https://doi.org/10.1175/AMSMONOGRAPHS-D-16-0010.1.

Highwood, E. J. and Hoskins, B. J., 1998: The tropical tropopause, *Q. J. Roy. Meteor. Soc.,* **124***,* 1579-1604, https://doi.org/10.1002/qj.49712454911.

Hokanson Wagner, E., 2025: *PREFIRE Auxiliary Meteorology Data for PREFIRE Satellite 1 version R01* [Data set]. NASA Langley Atmospheric Science Data Center Distributed Active Archive Center. https://doi.org/10.5067/PREFIRE-SAT1/PREFIRE/AUX-MET_L0.R01 Date Accessed: 2026-05-13

Houze, R. A. Jr., 1989: Observed structure of mesoscale convective systems and implications for large-scale heating, *Q. J. Roy. Meteor. Soc.,* **115**, 425-461, https://doi.org/10.1002/qj.49711548702.

—, K. L. Rasmussen, M. D. Zuluaga, and S. R. Brodzik, 2015: The variable nature of convection in the tropics and subtropics: A legacy of 16 years of the Tropical Rainfall Measuring Mission satellite, *Rev. Geophys*., **53**, 994-1021, https://doi.org10.1002/2015RG000488.

Huang, X., X. Chen, G. L. Potter, L. Oreopoulos, J. N. S. Cole, D. Lee, and N. G. Loeb, 2014: A Global Climatology of Outgoing Longwave Spectral Cloud Radiative Effect and Associated Effective Cloud Properties. *J. Climate,* **27**, 7475–7492, https://doi.org/10.1175/JCLI-D-13-00663.1.

Inoue, T., 1985: On the temperature and effective emissivity determination of semi-transparent cirrus clouds by bispectral measurements in the 10 micron window region. *J. Meteor. Soc. Japan,* **63,** 88–99, https://doi.org/10.2151/ jmsj1965.63.1_88.

Korolev, A. V., G.A. Isaac, P. Mazin, and H.W. Barker, 2001: Micophysical properties of continental clouds from *in situ* measurements, *Q. J. Roy. Meteor. Soc.,* **127,** 2117-2151, et al. 2001, https://doi.org/10.1002/qj.49712757614.

L'Ecuyer, T. S., and Coauthors, 2015: The observed state of global energy balance in the early 21st century. *J. Climate,* **28**, 8319–8346, https://doi.org/10.1175/ JCLI-D-14-00556.1.

—, A. Matus, and Z. Wang, 2019: Reassessing the Effect of Cloud Type on Earth's Energy Balance in the Age of Active Spaceborne Observations. Part I: Top of Atmosphere and Surface, *J. Climate,* **32**, 6197-6217, https://doi.org/10.1175/JCLI-D-18-0753.1.

— and Coauthors, 2021: The Polar Radiant Energy in the Far Infrared Experiment: A New Perspective on Polar Longwave Energy Exchanges, *Bull. Amer. Meteor. Soc.,* **102,** E1431-E1449, https://doi.org/10.1175/BAMS-D-20-0155.1.

Libois, Q., and J.-P. Blanchet, 2017: Added value of far-infrared radiometry for remote sensing of ice clouds, *J. Geophys. Res. Atmos.,* 122, 6541–6564, https:// doi.org/10.1002/2016JD026423.

Liu, C. and E. Zipser, 2013: Regional variation of morphology of organized convection in the tropics and subtropics, *J. Geophys. Res. Atmos.,* **118**, 453-466, https://doi.org/10.1029/2012JD018409.

Maestri, T., and Coauthors, 2014: Analysis of cirrus cloud spectral signatures in the far infrared. *J. Quant. Spectrosc. Radiat. Transfer*, **141**, 49–64, https://doi. org/10.1016/j.jqsrt.2014.02.030.

—, and R. Rizzi, 2003: A study of infrared diabatic forcing of ice clouds in the tropical atmosphere. *J. Geophys. Res.,* **108,** 4139, https://doi. org/10.1029/2002JD002146.

Masiello, G., C. Serio, T. Maestri, M. Martinazzo, F. Masin, G. Liuzzi, and S. Venafra, 2024: The new σ-IASI code for all sky radiative transfer calculations in the spectral range 10 to 2760 cm^{-1}: σ-IASI/F2N. *J. Quant. Spectrosc. Rad. Trans.,* **312**, 108814, https://doi.org/10.1016/j.jqsrt.2023.108814.

Merrelli, A., and D. D. Turner, 2012: Comparing information content of upwelling far-infrared and midinfrared radiance spectra for clear atmosphere profiling. *J. Atmos. Oceanic Technol*., **29,** 510–526, https://doi.org/10.1175/JTECHD-11-00113.1.

Palchetti, L. and Coauthors, 2020: FORUM: Unique Far-Infrared Satellite Observations to Better Understand How Earth Radiates Energy to Space, *Bull. Amer. Meteor. Soc.,* **101**, E2030–E2046, https://doi.org/10.1175/BAMS-D-19-0322.1.

Petty, G. W., 2006: *A First Course in Atmospheric Radiation (2nd ed)*. Sundog Publishing, 458 pp.

Pilewskie, J. A. and T. L'Ecuyer, 2022: The Global Nature of Early-Afternoon and Late-Night Convection Through the Eyes of the A-Train. *J. Geophys. Res. Atmos.,* **127**, e2022JD036438, https://doi.org/10.1029/2022JD036438.

—, G. Stephens, H. Takahashi, T. L'Ecuyer, 2024: A Multi-satellite Perspective on "Hot Tower" Characteristics in the Equatorial Trough Zone, *Surv. Geophys.*, **45**, 1933-1958, https://doi.org/10.1007/s10712-024-09868-2.

Rathke, C., J. Fischer, S. Neshyba, and M. Shupe, 2002: Improving IR cloud phase determination with 20 microns spectral observations, *Geophys. Res. Letters,* **29,** 50-1-50-4

Roca, R., T. Fiolleau, and D. Bouniol, 2017: A Simple Model of the Life Cycle of Mesoscale Convective Systems Cloud Shield in the Tropics. *J. Climate*, **30**, 4283–4298, https://doi.org/10.1175/JCLI-D-16-0556.1.

Saito, M., P. Yang, X. Huang, H. E. Brindley, M. G. Mlynczak, and B. H. Kahn, 2020: Spaceborne middle- and far-infrared observations improving nighttime ice cloud property retrievals. *Geophys. Res. Lett.,* **47,** e2020GL087491, https://doi .org/10.1029/2020GL087491.

Sassen, K., P. W. Arnott, D. Starr, G. Mace, Z. Wang, and M. R. Poellet, 2003: Midlatitude cirrus clouds derived from hurricane Nora: A case study with implications for ice crystal nucleation and shape. *J. Atmos. Sci.,* **60,** 873–891, https://doi.org/10.1175/1520-0469(2003)060<0873:MCCDFH>2.0.CO;2.

—, Z. Wang, D. Liu, 2008: Global distribution of cirrus clouds from CloudSat/Cloud-Aerosol Lidar and Infrared Pathfinder Satellite Observations (CALIPSO) measurements, *J. Geophys. Res. Atmos.,* **113**, 2008JD00A12

Slingo, J. M., and A. Slingo, 1988: The response of a general circulation model to cloud long-wave radiative forcing. I: Introduction and initial experiments, *Q. J. Roy. Meteorol. Soc.,* **114**, 1027 – 1062, https://doi.org/10.1002/qj.49711448209.

Sokolowsky, G. A. and Coauthors, 2024: *tobac* v1.5: introducing fast 3D tracking, splits and mergers, and other enhancements for identifying and analysing meteorological phenomena. *Geosci. Model Dev.,* **17**, 5309-5330, https://doi.org/10.5194/gmd-17-5309-2024.

Stackhouse, P.W., Jr. and Stephens, G.L., 1991: A theoretical and observational study of the radiative properties of cirrus clouds: results from FIRE 1986, *J. Atmos. Sci.,* **48,** 2044-2059, https://doi.org/10.1175/1520-0469(1991)048<2044:ATAOSO>2.0.CO;2.

Stephens, G. L., S.-C. Tsay, P. W. Stackhouse, and P. J. Flatau, 1990: The relevance of the microphysical and radiative properties of cirrus clouds to climate and climatic feedback, *J. Atmos. Sci.,* **47,** 1742 – 1753, https://doi.org/10.1175/1520-0469(1990)047<1742: TROTMA>2.0.CO;2.

Takahashi, H. and Z . J. Luo, 2014: Characterizing tropical overshooting deep convection from joint analysis of CloudSat and geostationary satellite observations, *J. Geophys. Res. Atmos.,* **119**, 112-121, https://doi.org/10.1002/2013JD020972.

—, M. Lebsock, Z. J. Luo, H. Masunaga, and C. Wang, 2021: Detection and Tracking of Tropical Convective Storms Based on Globally Gridded Precipitation Measurements: Algorithm and Survey over the Tropics, *J. Appl. Meteor. Climatol.,* **60,** 403-421, https://doi.org/10.1175/JAMC-D-20-0171.1.

Tegtmeier, S., and Coauthors, 2020: Temperature and tropopause characteristics from reanalyses data in the tropical tropopause layer, *Atmos. Chem. Phys.,* **20**, 753-770, https://doi.org/10.5194/acp-20-753-2020.

Turner, D. D., and E. J. Mlawer, 2010: Radiative Heating in Underexplored Bands Campaigns (RHUBC). *Bull. Amer. Meteor. Soc.,* **91,** 911–924, https://doi. org/10.1175/2010BAMS2904.1.

U.S. Committee on Extension to the Standard Atmosphere, 1976: U.S. Standard Atmosphere 1976, U.S. Govt. Print. Off., Washington, D. C. http://modelweb.gsfc.nasa.gov/atmos/us_standard.html.

Wendisch, M., P. Yang, and P. Pilewskie, 2007: Effects of ice crystal habit on the thermal infrared radiative properties and forcing of cirrus clouds. *J. Geophys. Res.,* **112**, D08201, https://doig.org/10.1029/2006JD007899.

Xian, T. and Y. Fu, 2015: Characteristics of tropopause-penetrating convection determined by TRMM and COSMIC GPS radio occultation measurements, *J. Geophys. Res.,* **120**, 7006-7024, https://doi.org/10.1002/2014JD022633.

Yang, P., and Coauthors, 2001: Sensitivity of cirrus bidirectional reflectance to vertical inhomogeneity of ice crystal habits and size distributions for two Moderate-Resolution Imaging Spectrometer (MODIS) bands. *J. Geophys. Res.,* **106**, 17267-17291, https://doi.org/10.1029/2000JD900618.

—, M. Mlynczak, H. Wei, D. Kratz, B. Baum, Y. X. Hu, W. Wiscombe, A. Heidinger, M. Mischchenko, 2003: Spectral signature of ice clouds in the far-infrared region: Single-scattering calculations and radiative sensitivity study. *J. Geophys. Res. Atmos.*, **108**, 2156-2202, https://doi.org/10.1029/2002JD003291.

—, L. Bi, B. Baum, K.-N. Liou, G. Kattawar, M. Mischchenko, B. Cole, 2013: Spectrally Consistent Scattering, Absorption, and Polarization Properties of Atmospheric Ice Crystals at Wavelengths from 0.2 to 100 μm, *J. Atmos. Sci.,* **70,** 339-347, https://doi.org/10.1175/JAS-D-12-039.1.

—., K.-N. Liou, L. Bi, C. Liu, B. Yi, and B. Baum, 2015: On the radiative properties of ice clouds: Light scattering, remote sensing, and radiation parameterization. *Adv. Atmos. Sci.,* **32,** 32-63, https://doi.org/10.1007/s00376-014-0011-z.

Yue, Q. and K. N. Liou, 2009: Cirrus cloud optical and microphysical properties determined from AIRS infrared spectra, *Geophys. Res. Letters*, **36**, 2008GL036502, https://doi.org/10.1029/2008GL036502.